2012-07-06

Analytical Thermal Model of Friction Stir Welding with Spatially Distributed Heat Source

Gordon Scott Reese
Brigham Young University - Provo

Analytical Thermal Model of Friction Stir Welding with Spatially Distributed Heat Source

Gordon Reese

A thesis submitted to the faculty of
Brigham Young University
in partial fulfillment of the requirements for the degree of

Master of Science

Matthew R. Jones, Chair
Tracy W. Nelson
Carl D. Sorensen

Department of Mechanical Engineering

Brigham Young University

August 2012

ABSTRACT

Analytical Thermal Model of Friction Stir Welding with
Spatially Distributed Heat Source

Gordon Reese
Department of Mechanical Engineering
Master of Science

Friction stir welding (FSW) has been studied extensively for the past two decades. Thermal modeling has been of particular interest, as the quality of the weld is dependent upon the temperature history of the work piece during the process. Since direct temperature measurements of the welded zone are not possible, an analytical model was developed to predict the temperature in this area. This model requires parameters that cannot be easily experimentally determined, so a best fit for these parameters was acquired via regression analysis by comparing the model to experimental data acquired outside of the weld zone. The model was then validated by comparing it to additional temperature data, not including the data used for regression analysis.

Keywords: friction stir welding, analytical thermal model

ACKNOWLEDGMENTS

I would like to thank first my adviser, Matthew Jones for his support and assistance. I also want to thank the other members of my committee, Carl Sorensen, Vladimir Solovjov, and Tracy Nelson for their expertise. I graciously acknowledge the financial support for this project, which was provided by the Brigham Young University Friction Stir Research Laboratory. The foundation of the modeling portion of this work was laid in large part by Chris Dillon, to whom I am indebted. Of course, I have my friends, family, and my supportive fiancée Alison to thank for their encouragement and support all throughout this project.

TABLE OF CONTENTS

LIST OF TABLES

LIST OF FIGURES

NOMENCLATURE

L	length of workpiece, m
W	half width of workpiece, m
S	depth of workpiece, m
v	velocity of FSW tool, m/s
T	temperature, K
$\dot{q}$	volumetric heat generation, W/m^3
k	thermal conductivity, W/m-K
α_t	thermal diffusivity, m^2/s
t	time, s
$D_{shoulder}$	diameter of tool shoulder, m
α	shoulder cone angle
H_{probe}	height of probe, m
D_{probe}	diameter of probe, m
r_s	outer length of heat source model, m
r_p	inner length of heat source model, m
r_s	outer width of heat source model, m
r_p	inner width of heat source model, m
h_s	inner depth of heat source model, m
h_p	outer depth of heat source model, m
Q_s	heat generated by shoulder, W
Q_p	heat generated by probe, W
f_s	heat fraction $\frac{Q_s}{Q_{tot}}$
f_o	heat fraction $\frac{Q_o}{Q_{tot}}$
Q_{tot}	total heat generated, W
Q_o	heat transferred through the backing plate, W
H	Heaviside step function
δ	Dirac delta function

h	convection coefficient, W/m^2-K
U	overall heat transfer coefficient through backing plate, W/m^2-K
T_∞	ambient temperature, K
ξ	nondimensional length $\frac{x}{L}$
η	nondimensional width $\frac{y}{W}$
ζ	nondimensional depth $\frac{z}{S}$
τ	nondimensional time $\frac{\alpha_t t}{L^2}$
ξ_o	nondimensional velocity $\frac{vt}{L}$
θ	nondimensional temperature $\frac{WSk}{Q_{tot}L}(T - T_\infty)$
Bi	Biot number $\frac{hL}{k}$
μ	ratio of surface heat transfer $\frac{U}{h}$
ξ_s	nondimensional length $\frac{r_s}{L}$
ξ_p	nondimensional length $\frac{r_p}{L}$
η_s	nondimensional width $\frac{r_s}{W}$
η_p	nondimensional width $\frac{r_p}{W}$
ζ_s	nondimensional depth $\frac{r_s \tan(\alpha)}{S}$
ζ_p	nondimensional depth $\frac{h_p}{S}$
A	length ratio $\frac{W}{L}$
B	length ratio $\frac{S}{L}$
f_p	heat fraction $\frac{Q_p}{Q_{tot}}$
ω	angular speed of tool, rad/s
P_{mech}	mechanical power of FSW tool, W
f_{therm}	fraction of FSW tool power converted to heat $\frac{Q_{tot}}{P_{mech}}$

1 INTRODUCTION

1.1 Background

Friction stir welding (FSW) is a solid-state joining process developed by researchers at The Welding Institute in 1991 (Thomas 1991). A rotating tool plunges into a joint interface (see Figure 1-1), generating frictional heat and stirring material together to create a welded joint (see Figure 1-2). The solid-state nature of this process results in welds with superior properties when compared to conventional welding processes, as the temperature of the material remains below its melting point.

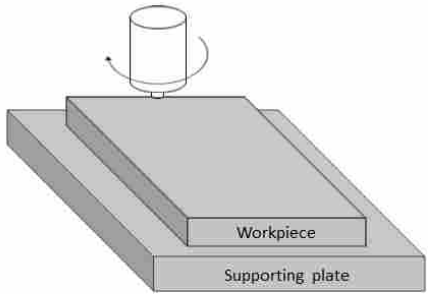

Figure 1-1: Diagram of FSW tool and process

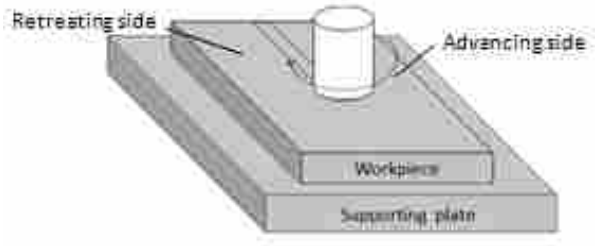

Figure 1-2: Different regions of the FSW process

Primarily, FSW is applied in the joining of aluminum parts where post-weld heat treatment is difficult or impossible. Aerospace, automotive, railway, and shipbuilding industries have successively applied this technology, including the manufacturers of the Delta series rockets (Uday 2010). Applications with different metals are now being investigated, as the solid-state nature of the joining process of FSW results in very desirable weld properties, without the porosity or cracking due to solidification found in conventional welding techniques (Gould 1998).

Phenomena associated with FSW involve complex thermomechanical interactions between the tool and the workpiece material. The rapidly rotating tool induces three-dimensional mixing of the material while containg the material flow with downward force. Additionally, the process is asymmetric about the weld line. The side of the weld line where the FSW tool is rotating towards the direction of the tool path is referred to as the advancing side, while the other side is referred to as the retreating side (Cho 2005).

The mechanical properties of material undergoing a FSW process are dependent upon its temperature history, so it is of interest to manufacturers to either directly measure the workpiece's temperature or predict it using a model. Direct measurement in the stirred weld zone itself is impossible, as instruments placed there would be destroyed by the stirring process. Additionally, direct measurement requires extensive preparation and drilled holes for thermocouple placement, making this method of evaluating temperature of welds prohibitively time-consuming and expensive. Therefore, an accurate analytical thermal model remains the lowest cost and most desirable method of predicting the temperature history inside the stirred

weld zone. An accurate model can be parameterized and used to optimize for cooling rates and peak temperatures to achieve desired temperature histories in manufacturing applications.

1.2 **Discussion of Previous Work**

Thermal modeling of FSW is complicated by the coupling of the work done by the FSW tool to deform the welded material and the frictional heat generated (Nandan 2008). Many numerical models have been employed, using the finite element method to account for such complexities such as variable contact resistance between the workpiece and the backing plate (Soundararajan 2005), torque-based heat input (Khandkar 2003), and the mechanical deformation of the workpiece material (Hamilton 2008). Results from these models agree well with experimental data, although they require significant computational resources and set up (Schmidt 2008).

Significant work has also been performed on analytical models for FSW, which are less computationally expensive than numerical models. Most of these analytical models are based on Rosenthal's foundational study on moving punctual heat sources (Rosenthal 1941). Much of the work on these analytical models focuses on the proper treatment of the heat generation in FSW. One of the earlier studies in this area, conducted by McClure et al (McClure 1998) described the heat generated by the FSW tool in terms of rotational speed and pressure against the workpiece. Schmidt et al (Schmidt 2004) developed a more detailed model that allows the heat generation of the FSW tool to be expressed as a function of the stirred material's yield stress, the geometry of the FSW tool, the tool's rotational speed, and the frictional condition at the tool-workpiece interface. Ferro and Bonollo (Ferro 2009) built upon this model of heat generation and used an iterative approach to determine the temperature field of a workpiece undergoing FSW. Vilaca et

al (Vilaca 2005) developed a similar analytical model, also accounting for the asymmetry in temperature distribution due to the rotating motion of the tool.

These analytical thermal models of FSW are fairly sophisticated and have been demonstrated to agree reasonably well with experimental data under specific circumstances (Nandan 2008). Generally, these models either rely on input data from previous experiments for best accuracy, or only show accurate results when compared to a limited set of data in the midplane of the workpiece. Additionally, since these thermal models are based on Rosenthal's mathematical treatment (Rosenthal 1941) in which the source is modeled using a singular Dirac delta function, the predicted temperatures near the heat source are significantly overestimated. Since it is of great interest to determine the thermal history of the entire workpiece—especially in the stirred zone, near the heat source—an alternative analytical model for the heat source that will accurately predict temperatures is herein proposed. This analytical model may be applied to different welds and compare favorably with data obtained at various depths and distances from the welding tool.

1.3 **Objective**

The purpose of this study is to develop an analytical model of friction stir welding that predicts the thermal history at any location within the workpiece during a FSW process. The frictional heat generated at the FSW tool-workpiece interface is modeled with a spatially distributed heat source, rather than the point source used in other current analytical models (Ferro 2009). This distributed heat source allows for finite temperature predictions near the FSW tool, unlike the unrealistically high temperatures predicted near the tool with point source models.

This model will be hereafter referred to as the analytical distributed source (ADS) model. In the ADS model, the total heat input used in this model is calculated with Schmidt's model (Schmidt 2004) and the heat source is distributed over a volume, rather than modeled as a point source. The ADS model predicts finite temperatures in the stirred zone and throughout the workpiece. Schmidt's model (Schmidt 2004) requires parameters that describe the heat generation and the thermal boundary conditions, which are determined by inverse modeling of far-field temperature measurements. A small subset of data collected by Huang (Huang 2008) and Furse (Furse 2010) is used to obtain estimates for these key model parameters, such as the conductance through the backing plate and the fraction of tool power converted to heat by the shoulder and pin. The ADS model's predicted temperatures are compared with the remaining data collected by Huang (Huang 2008) and Furse (Furse 2010).

1.4 **Overview**

The development of the ADS model is detailed in the following chapter. The resulting governing equation and boundary conditions applied are presented with a discussion of the key parameters and assumptions made in the development of the model. The experiments used to assess the model are also outlined at the end of Chapter 2. The results from this validation are shown in Chapter 3, along with observations about the model's behavior. Temperature contours calculated by the model are given in the end of Chapter 3. Chapter 4 draws conclusions from the results depicted in Chapter 3.

2 MODEL DESCRIPTION AND VALIDATION

2.1 Solution of Heat Diffusion Equation

2.1.1 Governing Equation

The three-dimensional, transient heat diffusion equation describes the transfer of heat within the workpiece based on Langrangian perspective, which is illustrated in Figure 2-1. The thermophysical properties of the workpiece are assumed to be uniform and independent of temperature.

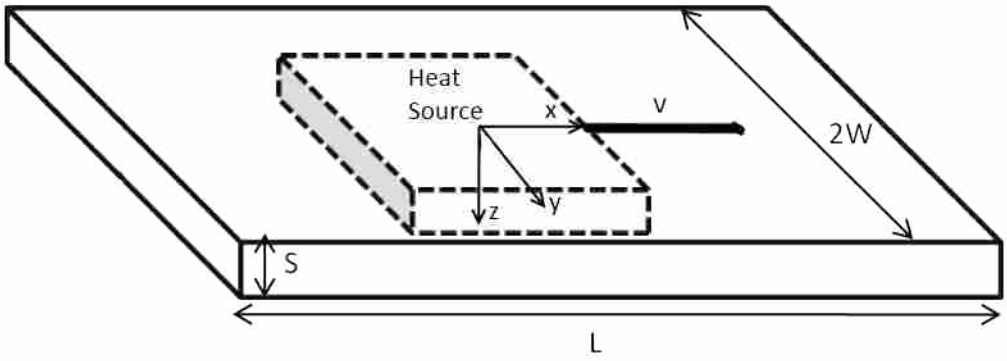

Figure 2-1: Diagram of the workpiece and the moving heat source

Under these conditions, the governing differential equation is as follows.

$$\frac{\partial^2 T}{\partial x^2}+\frac{\partial^2 T}{\partial y^2}+\frac{\partial^2 T}{\partial z^2}+\frac{\dot{q}}{k}=\frac{1}{\alpha_t}\frac{\partial T}{\partial t} \qquad \text{2-1}$$

2.1.2 Overall Energy Balance

The mechanical energy of the FSW tool is converted into thermal energy as heat and into the kinetic energy associated with the bulk motion of workpiece material and the vibration of the supporting structures. The fraction of the total power, Q_{tot}, converted to heat and transferred into the workpiece is defined by the factor f_{therm}, which is discussed further in Section 2.2.2. Consider a section of the workpiece to be the system as illustrated in Fig. 2-2. In the ADS model, heat is assumed to be generated due to friction within the *t*-shaped region shown below. This heat is stored within the system, or it is transferred out of the system. Heat is transferred out of the system by convection from the exposed surface or is conducted further into the workpiece and into the supporting plate below.

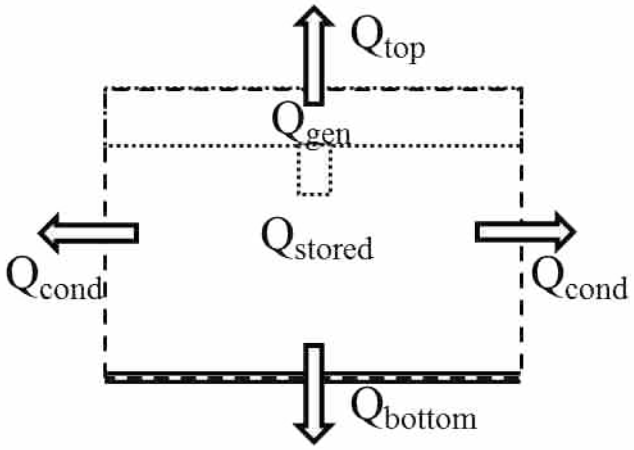

Figure 2-2: Diagram of control volume for energy balance

2.1.3 FSW Tool Description

The FSW tool itself is a cylindrical piece consisting of a "probe" and a "shoulder," as depicted in Figure 2-3, which rotates at speed ω. The probe plunges into the workpiece while the shoulder moves across the surface. Frictional heating at the rotating surfaces softens the workpiece material such that material begins to plastically deform about the FSW tool. This

heating can be modeled as the product of the friction stress at the interface and the relative tool velocity. Commonly, this friction stress is modeled as Coulomb friction, using the downward pressure of the tool and the proportionality coefficient μ (Maalekian 2008).

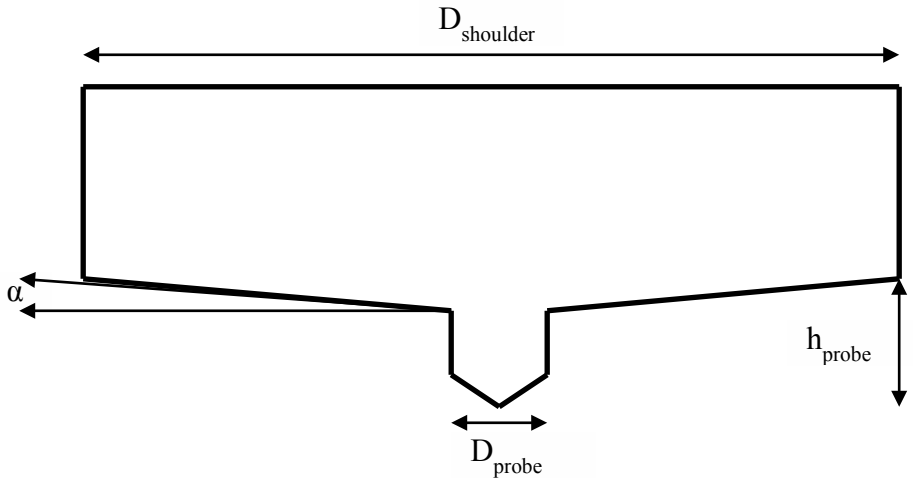

Figure 2-3: Detailed view of the FSW tool

Frictional heating in FSW is complicated by the plastic deformation of the workpiece material. This deformation results in significant variation in the stress at the tool-workpiece interface, as the material shears with the rotating tool surfaces, rather than rubbing against them. This condition is sometimes referred to as "sticking," and the extent to which this occurs is highly dependent upon the temperature and mechanical properties of the material (Schmidt 2005). Additionally, the flow of the workpiece material induces viscous dissipation, serving to increase the local temperature (Moraitis 2010).

2.1.4 FSW Tool Model Description

Given the complex nature of the FSW process, finite element methods are usually employed, such as the model used by Moraitis et al (Moraitis 2010) or Hamilton et al (Hamilton

2008). As discussed earlier, these models require significant set up and computational resources to evaluate. In order to develop a mathematically tractable analytical solution, approximations are required.

The heat source created by the FSW tool is modeled as shown below in Figure 2-4. The subdivisions within the heat source approximate the spatial variation in heat input. The dimensions in the *x*- and *y*- directions are constrained to the outer and inner radii of the FSW tool. The outer and inner divisions approximate the heat generation contribution by the tool shoulder and the probe, respectively. The depth of the shoulder portion is the radius of the shoulder multiplied by the tangent of the shoulder cone angle α. The depth of the probe portion of the heat source is set to h_{probe}.

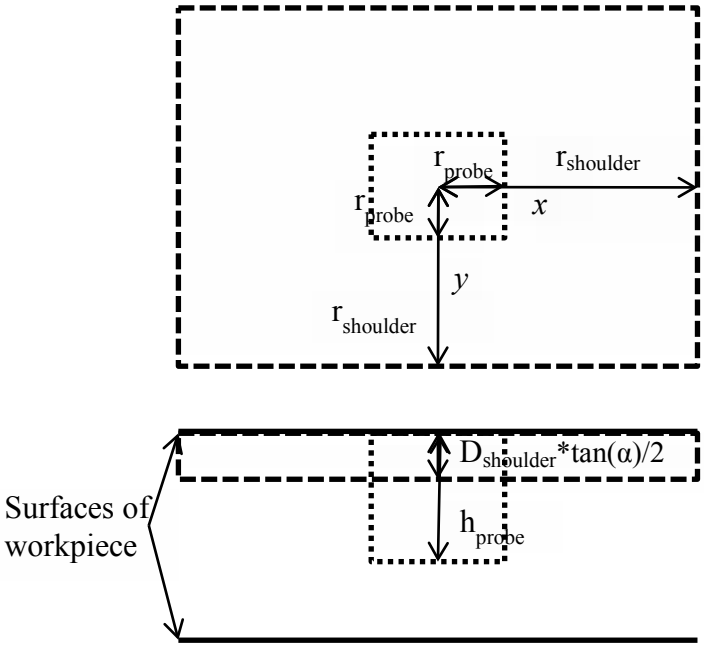

Figure 2-4: Details of the partitions of the moving heat source used in the thermal model

Equation 2-2 describes the heat generation as shown in Equation 2-1, where Q_s and Q_p represent the heat generated in the shoulder and probe zones, respectively. These values sum to Q_{tot}, the total heat input. The values used for these parameters are calculated by models proposed

by Schmidt (Schmidt 2004). A thermal sink is introduced using the parameter Q_o. This sink term is included because the localized pressure exerted by the FSW tool significantly reduces the thermal contact resistance immediately beneath the tool, resulting in a higher rate of heat transfer into the supporting plate beneath the tool. The inverse modeling technique used to obtain the value of Q_o is described in Section 2.2.6.

$$\dot{q} = \frac{Q_s}{r_s\tan(\alpha)(4r_s^2-4r_p^2)}\{[H(x-vt+r_s)-H(x-vt-r_s)][1- H(y-r_s)][1-H(z-r_s\tan(\alpha))]-[H(x-vt+r_p)- H(x-vt-r_p)][1-H(y-r_p)][1-H(z-r_s\tan(\alpha))]\}+ \frac{Q_p}{4h_p r_p^2}\{[H(x-vt+r_p)-H(x-vt-r_p)][1-H(y-r_p)][1- H(z-h_p)]\}-\frac{Q_o}{4r_s^2}\{[H(x-vt+r_s)-H(x-vt-r_s)][1- H(y-r_s)]\delta(z-S)\} \quad \textbf{2-2}$$

2.1.5 Boundary Conditions

The boundary conditions and initial condition applied to Equation 2-1 are shown below. Convective conditions were applied on all surfaces except for the workpiece-backing plate interface. This interface was modeled with an overall heat transfer coefficient U. A symmetrical boundary condition was implemented across the y-axis, which ignores the effects of the enhanced heat generation on the advancing side of the tool. This approximation was made in order to achieve a mathematically tractable solution to the governing differential equations.

$$k\frac{\partial T}{\partial x}|_{x=0} = h(T-T_\infty) \quad \textbf{2-3}$$

$$-k\frac{\partial T}{\partial x}|_{x=L} = h(T-T_\infty) \quad \textbf{2-4}$$

$$\frac{\partial T}{\partial y}|_{y=0} = 0 \quad \textbf{2-5}$$

$$-k\frac{\partial T}{\partial y}|_{y=W} = h(T - T_\infty) \quad \textbf{2-6}$$

$$k\frac{\partial T}{\partial z}|_{z=0} = h(T - T_\infty) \quad \textbf{2-7}$$

$$-k\frac{\partial T}{\partial z}|_{z=S} = U(T - T_\infty) \quad \textbf{2-8}$$

$$T(x, y, z, 0) = T_\infty \quad \textbf{2-9}$$

2.1.6 Solution of Governing Equation

Equation 2-1 was solved using an eigenfunction expansion. The nondimensional temperature distribution was assumed to be described by the summation in Equation 2-10. The heat source described by Equation 2-2 is also expressed as a summation in 0.

$$T(x, y, z, t) = \sum_{p=1}^{\infty}\sum_{q=1}^{\infty}\sum_{r=1}^{\infty} c_{pqr}(t)X_p(x)Y_q(y)Z_r(z) \quad \textbf{2-10}$$

The eigenfunctions and eigenvalues used in Equation 2-10 are a result of solving the corresponding Sturm-Liouville problems in each direction. The details of this solution are shown in Appendix A. The resulting eigenfunctions are shown in the following equations.

$$X_p = \sin\left(\lambda_p\frac{x}{L}\right) + \frac{\lambda_p}{Bi}\cos\left(\lambda_p\frac{x}{L}\right) \text{ where } \tan(\lambda_p) = \frac{2\lambda_p Bi}{\lambda_p^2 - Bi^2} \quad \textbf{2-11}$$

$$Y_q = \cos\left(\frac{W}{L}\beta_q\frac{y}{W}\right) \text{ where } \tan\left(\frac{W}{L}\beta_q\right) = \frac{Bi}{\beta_q} \quad \textbf{2-12}$$

$$Z_r = \sin\left(\frac{S}{L}\gamma_r\frac{z}{S}\right) + \frac{\gamma_r}{Bi}\cos\left(\frac{S}{L}\gamma_r\frac{z}{S}\right) \text{ where } \tan\left(\frac{S}{L}\gamma_r\right) = \frac{Bi\gamma_r(1+\mu)}{\gamma_r^2 - Bi^2\mu} \quad \textbf{2-13}$$

The expansion coefficients are given in the following equation.

$$c_{pqr} = \frac{\left[Bi\left(\lambda_p^2+\beta_q^2+\gamma_r^2\right)+\frac{\lambda_p^2 vL}{\alpha_t}\right]\sin\left(\lambda_p\frac{vt}{L}\right)+\left[\lambda_p\left(\lambda_p^2+\beta_q^2+\gamma_r^2\right)-\frac{Bi\lambda_p vL}{\alpha_t}\right]\cos\left(\lambda_p\frac{vt}{L}\right)}{2N_pN_qN_r\frac{W}{L}\lambda_p\beta_q Bi\left[\left(\lambda_p^2+\beta_q^2+\gamma_r^2\right)^2+\frac{\lambda_p^2v^2L^2}{\alpha_t^2}\right]} \quad \textbf{2-14}$$

$$\left\{\left[\frac{\frac{Q_S}{Q_{tot}}}{\left(\frac{r_S}{L}\left(\frac{r_S r_S}{L\,W}-\frac{r_p r_p}{L\,W}\right)\right)\frac{S}{L}\gamma_r}\left(\left(sin\left(\beta_q\frac{W}{L}\frac{r_p}{W}\right)sin\left(\lambda_p\frac{r_p}{L}\right)-\right.\right.\right.$$

$$sin\left(\beta_q \frac{W}{L}\frac{r_s}{W}\right) sin\left(\lambda_p \frac{r_s}{L}\right)\right)\left(cos\left(\gamma_r \frac{S}{L}\frac{r_s \tan(\alpha)}{S}\right) - 1 - \frac{\gamma_r}{Bi} sin\left(\gamma_r \frac{S}{L}\frac{r_s \tan(\alpha)}{S}\right)\right)\Bigg] -$$

$$\frac{\frac{Q_p}{Q_{tot}}}{\left(\frac{r_p r_p}{L\ W}\frac{h_p}{S}\right)\frac{S}{L}\gamma_r}\left[sin\left(\beta_q \frac{W}{L}\frac{r_p}{W}\right) sin\left(\lambda_p \frac{r_p}{L}\right)\left(cos\left(\gamma_r \frac{S}{L}\frac{h_p}{S}\right) - 1 - \frac{\gamma_r}{Bi} sin\left(\gamma_r \frac{S}{L}\frac{h_p}{S}\right)\right)\right] -$$

$$\frac{\frac{Q_o}{Q_{tot}}}{\left(\frac{r_s r_s}{L\ W}\right)}\left[sin\left(\beta_q \frac{W}{L}\frac{r_s}{W}\right) sin\left(\lambda_p \frac{r_s}{L}\right)\left(sin\left(\gamma_r \frac{S}{L}\right) + \frac{\gamma_r}{Bi} cos\left(\gamma_r \frac{S}{L}\right)\right)\right]\Bigg\}$$

Equation 2-10 shows that the temperature is dependent upon time, position, input heat, fractions of input heat contributed by the shoulder and the probe, convection coefficient, workpiece-supporting plate conductance, dimensions of the workpiece, dimensions of the FSW tool, the velocity of the tool, and the thermophysical properties of the workpiece material. In order to evaluate for temperatures within the workpiece, it is required to find suitable values for all unknown parameters. Input heat, convection, and conductance between the workpiece and the supporting plate are obtained in the manner described in the following section.

2.2 **Determination of Unobservable Parameters**

2.2.1 Heat Generation

There are several parameters that need to be assigned values before Equation 2-10 can be evaluated. The most important parameter is the heat input. Schmidt et al (Schmidt 2004) proposed an analytical model for the mechanical power, P_{mech}, in FSW which is dependent upon the contact condition between the FSW tool and the workpiece. Schmidt considers this mechanical power to be approximately equal to the total heat generation.

Two FSW tool-workpiece contact conditions are suggested by Schmidt: the "sticking" and the "sliding" conditions. The "sticking" condition assumes that workpiece material in contact with the rotating tool shears off from the underlying workpiece material, leading to contact stress being the shear stress of the material, τ_{yield}. Assuming a constant stress, the heat

generation due to sticking can be modeled as the product of the rotational speed of the tool, the surface area of the tool, and the shear stress. The three terms in the following equation represent the contributions from the shoulder, the probe tip, and the probe sides.

$$P_{mech,sticking} = \frac{2}{3}\pi\tau_{yield}\omega\left(\left(R_{shoulder}^3 - R_{probe}^3\right)(1+\tan(\alpha)) + R_{probe}^3 + 3R_{probe}^2 H_{probe}\right) \quad \textbf{2-15}$$

With the above equation, P_{mech} can be estimated for the sticking condition. The sliding condition describes contact where the tool slides along the surface of the workpiece without moving material. Schmidt develops the model further to account for a hybrid between the sticking and sliding conditions (Schmidt 2004), introducing additional unknown parameters. For the ADS model, the sticking condition is assumed to predict the mechanical power used in the FSW process. Because the sticking condition necessarily requires that mechanical power be consumed in bulk motion of workpiece material, an estimate for the fraction of the total mechanical power converted to thermal energy must be made.

2.2.2 Fraction of Heat Transferred to Workpiece

The fraction f_{therm}, approximates the portion of P_{mech} converted to thermal energy and transferred to the workpiece, rather than conducted up the FSW tool. Q_{tot} then becomes the product of P_{mech} and f_{therm}. Nandan et al (Nandan 2007) modeled this fraction with Equation 2-16 as a function of the tool and workpiece thermal properties.

$$f_{therm} = \frac{\sqrt{(k\rho c_p)_{workpiece}}}{\sqrt{(k\rho c_p)_{tool}}} \quad \textbf{2-16}$$

This equation results from the analysis of two semi-infinite dissimilar materials in contact with a point heat source at the interface (Carslaw 1959). The FSW tool, relative to the workpiece, is quite large, so considering the two materials as semi-infinite is an approximation. No contact resistance is assumed between the two solids, and the two solids are assumed to start at thermal equilibrium. Lienert et al (Lienert T.J. 2003) found this expression to provide good estimates for this fraction in FSW on AISI 1018 mild steel. This expression gives an estimate for f_{therm}, but it does nothing for approximating the amount of mechanical energy converted to thermal energy. Inverse modeling is employed to find the best fit value, which is described in Section 2.2.6.

2.2.3 Thermal Contact Resistance Between Workpiece and Supporting Plate

The overall backside heat transfer coefficient *U*, which models the heat loss through the supporting plate underneath the workpiece, is a critical parameter that greatly influences thermal cycles in FSW. Researchers have suggested different values for an overall heat transfer coefficient, from 500 W/m^2-K (Chao 1998) to as great as 10000 W/m^2-K (Khandkar 2003). Given the complex nature of thermal contact resistance, the value of *U* was determined by optimization techniques.

In addition to the complexity of the thermal interaction between the workpiece and the supporting plate, there is a significant reduction in thermal contact resistance due to the downward force exerted by the FSW tool. The tool effectively increases the heat transfer to the supporting plate directly beneath it. To mathematically represent this moving region of reduced

thermal contact resistance, the parameter f_o, which is the result of the localized heat loss (Q_o) divided by the total heat input (Q_{tot}), is employed. Like U, the best value for f_o was determined with optimization techniques.

2.2.4 Convection Coefficient

To obtain an estimate of the convection coefficient for the surfaces of the workpiece, the McAdams horizontal flat plate correlation in Equation 2-17 was used, which is available in literature (Incropera 2007).

$$Nu = 0.15 Ra_L^{\frac{1}{3}} \qquad \textbf{2-17}$$

The natural convection from the surfaces of the workpiece was assumed to be turbulent, with an ambient temperature of 300 K and an average surface temperature of 400 K. This correlation results in a convection coefficient h of approximately 10 W/m^2-K.

The following figures show the relatively small effect of the precise value of h for free convection ranges (5 to 50 W/m^2-K). The temperature profiles were calculated for a thermocouple location (x = 73.08 cm, y = 10.08 mm, z = 1.27 mm) in the Furse weld (Furse 2010) using f_{therm} (referred to in the figure as ftherm) = 0.7, U = 200 W/m^2-K, f_o (referred to as qo) = 0.7, and varying h. Note that all temperature profiles in this section are calculated at the same x location.

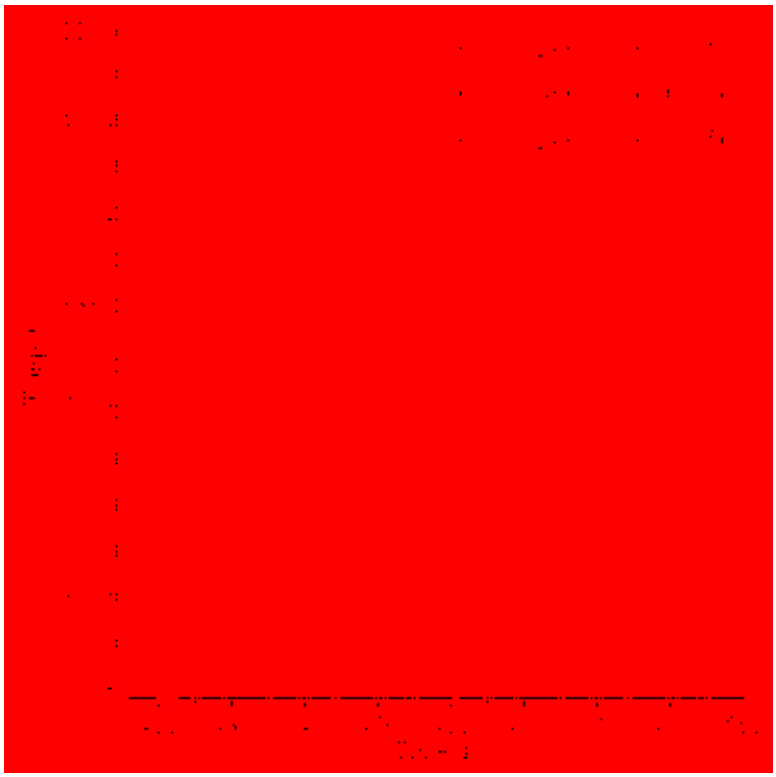

Figure 2-5: Effect of variation of *h* on the thermal history at y=10.08mm and z=1.27mm

Note that the value of *h* has a small effect on the temperature profile at any point in the workpiece. At locations farther from the center of the weld line, *h* has a slightly larger impact on the thermal history within the workpiece. It can be seen that while the overall cooling rate is enhanced with increasing convection, it is not the dominating factor in the cooling rate.

Since the value of the convection coefficient *h* does not significantly impact the ADS model's temperature predictions, the value of 10 W/m^2-K will be used in all subsequent calculations.

It should also be noted that there is "ringing" in the temperature curve of Figure 2-7, near the boundaries of the solution space (surfaces and edges of the workpiece).

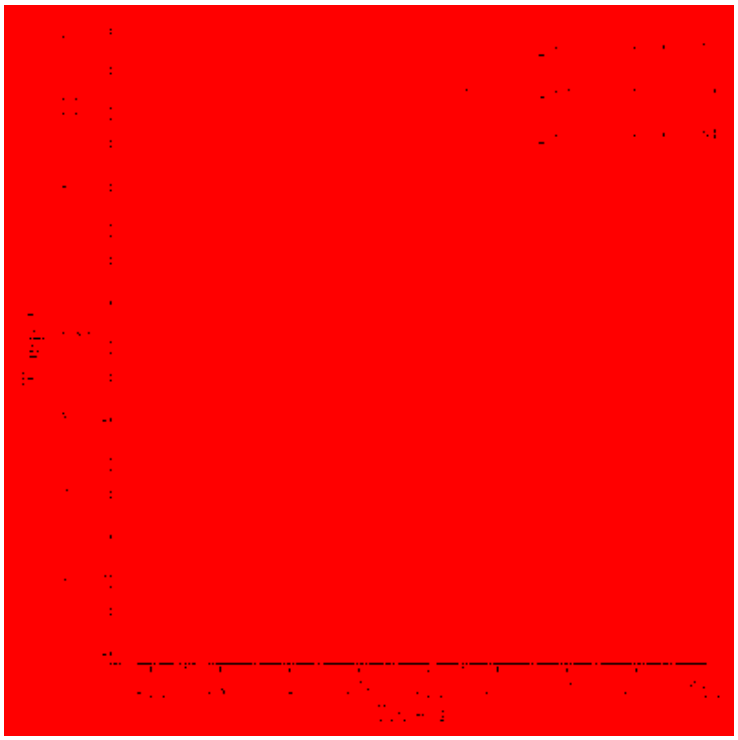

Figure 2-6: Effect of variation of *h* on the thermal history at y=5mm and z=5mm

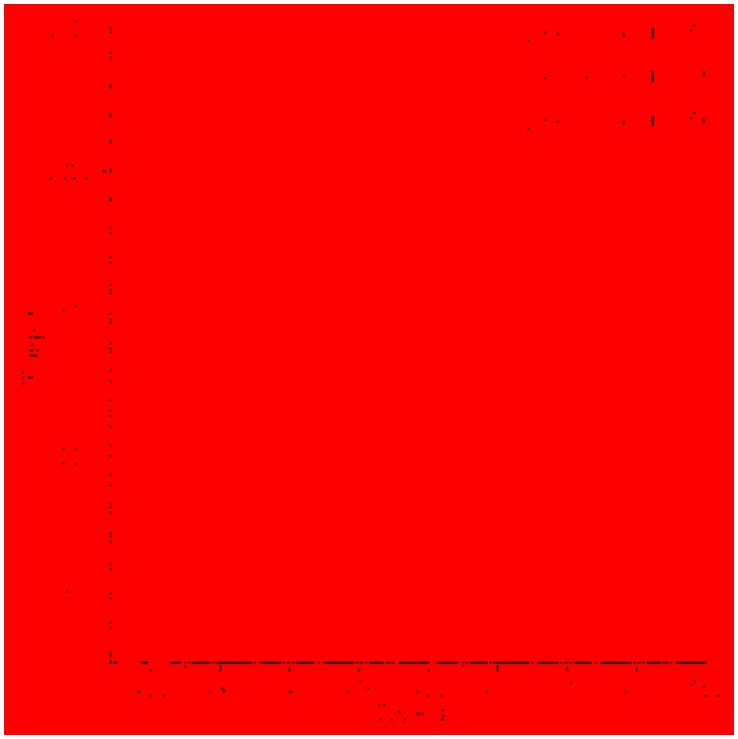

Figure 2-7: Effect of variation of *h* on the thermal history at y=1mm and z=0.5mm

2.2.5 Fractions of Q_{tot} Assigned to Shoulder and Pin Zones

The total heat input, Q_{tot}, is divided across two zones, as referenced in Figure 2-4. The fractions of the total heat assigned to the shoulder and the probe zones, f_s and f_p can be modeled with Equations 2-18 and 2-19, as derived by Schmidt (Schmidt 2004). These fractions summed together yield 1.

$$f_s = \frac{Q_s}{Q_{tot}} = \frac{\left(R_{shoulder}^3 - R_{probe}^3\right)(1+\tan(\alpha))}{\left(\left(R_{shoulder}^3 - R_{probe}^3\right)(1+\tan(\alpha)) + R_{probe}^3 + 3R_{probe}^2 H_{probe}\right)} \quad \textbf{2-18}$$

$$f_p = \frac{Q_p}{Q_{tot}} = \frac{R_{probe}^3 + 3R_{probe}^2 H_{probe}}{\left(\left(R_{shoulder}^3 - R_{probe}^3\right)(1+\tan(\alpha)) + R_{probe}^3 + 3R_{probe}^2 H_{probe}\right)} \quad \textbf{2-19}$$

Eliminating the convection coefficient as a significant parameter and solving for f_s and f_p with the previous equations, the remaining input parameters to solve the governing differential equations must be found by inverse analysis of available data. This inverse analysis allows the model to be better "trained" to provide the most accurate results for the weld under investigation. Details of this method to obtain values for f_{therm}, U, and f_o are discussed in the following section.

2.2.6 Optimization Techniques Used in Determining Unobservable Parameters

To obtain the best values for f_{therm}, U, and f_o, Equation 2-10 and its accompanying equations that determine the solution's eigenvalues (see 0) were written into a Maple procedure, such that the procedure uses these unknown parameters as inputs to output the modeled temperature profile. Then, experimental temperature data from a variety of depths and horizontal distances from the center of the weld were selected to compare with the modeled temperature

profile. Evaluating the model at the corresponding spatial location for each experimental dataset, the model temperature value at each time step in the data was subtracted from the experimental value to determine the residual. Each residual was squared, and the residuals were summed together. Implementing the sum of the squared residuals with a set of experimental data into the original procedure, an input of the unknown parameters outputs the error see. In Figure 2-8, a temperature profile at location subscript 1 is plotted versus time. At each point, the residuals between the predicted temperature and the data were summed to produce $Error_1$, the squared sum of residuals for location subscript 1.

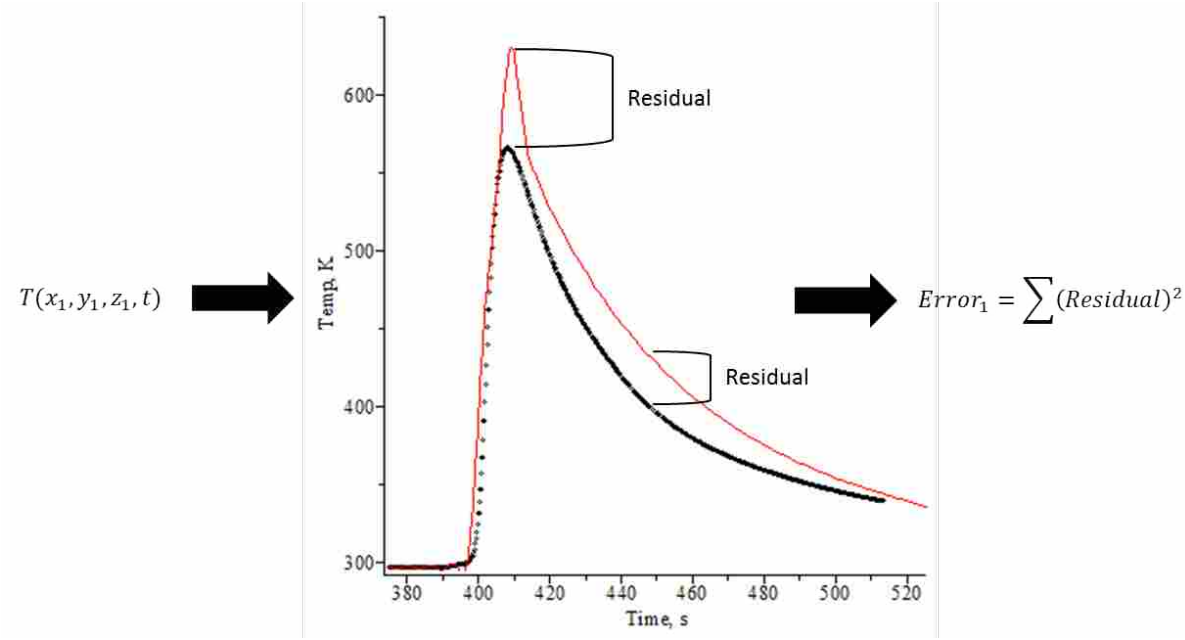

Figure 2-8: Description of how error is calculated for a set of thermocouple data

With the sum of the squared residuals as the objective function, bounds were placed on the allowable values of the unknown parameters such that they remain nonnegative and that f_{therm} and f_o do not exceed unity. The sum of the squared residuals was then minimized using sequential quadratic programming (Bonnans 2006), resulting in the best unobservable parameter

values for a given location within the workpiece. Using the optimized results from multiple locations, these parameter values were averaged to obtain best fit values for the entire workpiece.

After this inverse modeling, all the required parameters now are defined, allowing for the evaluation of Equation 2-10. In order to demonstrate how the optimized parameters can affect the predicted temperature profiles from the ADS model, various values of f_{therm}, U, and f_o will be compared at different depths and distances from the center of the weld line. This will also demonstrate what the optimization procedure does to find a best fit for these parameters to the training data.

2.3 Effect of Unobservable Parameters

2.3.1 Effect of Variation in f_{therm}

Variation in the fraction f_{therm} describes variation in the amount of energy transferred into the workpiece as heat compared to the heat transferred to the tool and the energy used in plastic deformation of workpiece material. This parameter has the largest effect on the modeled peak temperature, as it effectively varies the amount of heat input in the ADS model. The model is quite sensitive to modest changes in this value. As expected, the time to cool to ambient temperature is extended for higher values of f_{therm}, due to the higher peak temperature.

The effect of varying f_{therm} is demonstrated by displaying temperature profiles at x = 73.08 cm in the following figures. The parameters used are displayed in each figure, and the y and z locations are described in the captions.

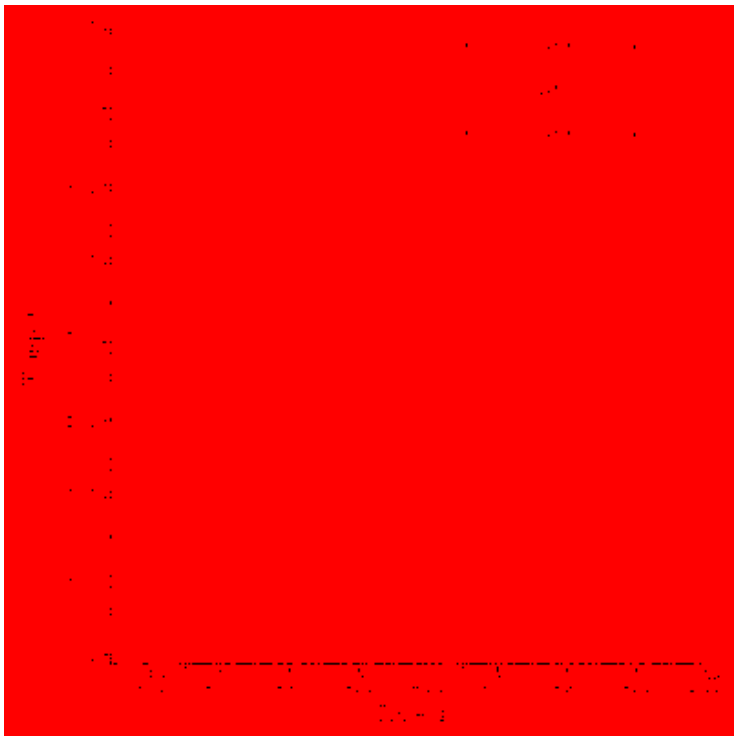

Figure 2-9: Effect of variation of f_{therm} on the thermal history at y=10.08mm and z=1.27mm

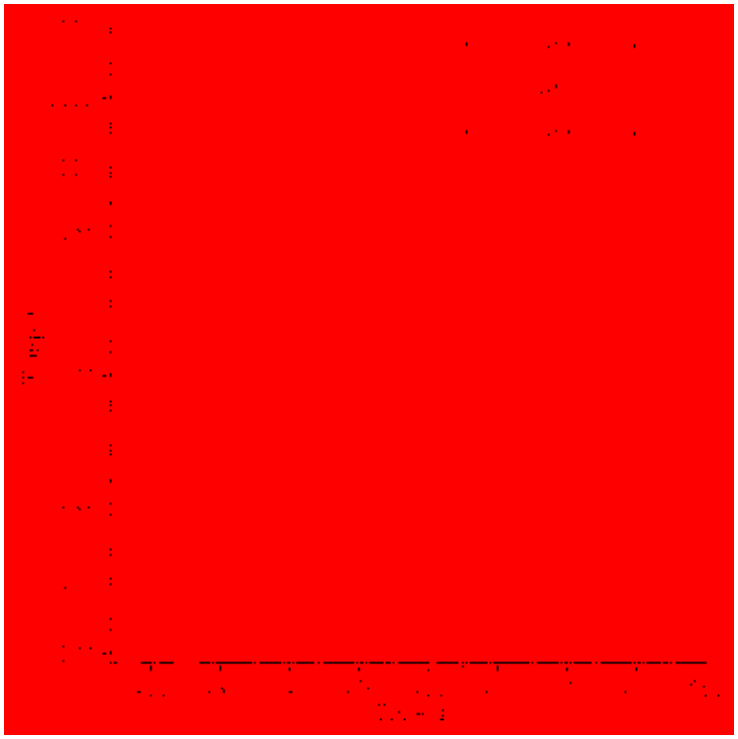

Figure 2-10: Effect of variation of f_{therm} on the thermal history at y=5mm and z=5mm

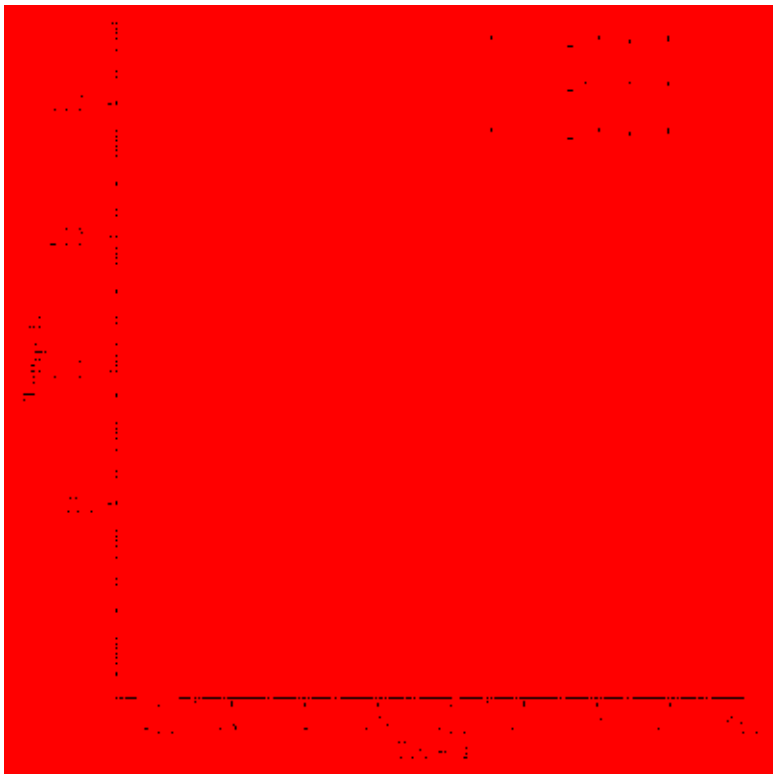

Figure 2-11: Effect of variation of f_{therm} on the thermal history at y=1mm and z=0.5mm

The impact of f_{therm} is rather significant, and it becomes increasingly meaningful at locations closer to the surface, where the same change in f_{therm} produces larger changes in peak temperature than at locations deeper within the workpiece.

2.3.2 Effect of Variation in *U*

Variation in the overall heat transfer coefficient *U* describes the degree to which heat flows from the workpiece to the supporting plate beneath it, which is dependent upon the amount of thermal contact resistance between the two plates. This parameter is demonstrated to have very little impact on the peak temperature. However, the cooling rate is highly dependent on the value of this parameter—larger values result in rapid cooling, and smaller values lengthen the time required for the workpiece to return to room temperature.

The effect of varying *U* is demonstrated by displaying temperature profiles at x = 73.08 cm in the following figures. The parameters used are displayed in each figure, and the *y* and *z* locations are described in the captions.

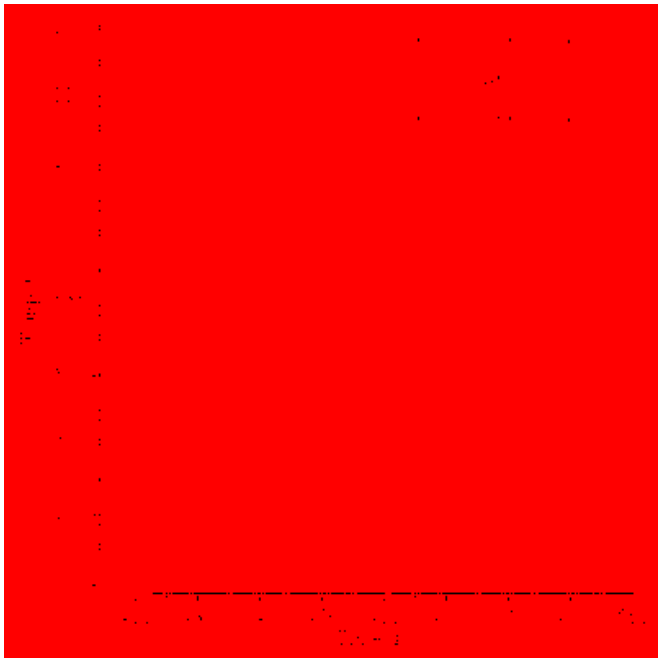

Figure 2-12: Effect of variation of *U* on the thermal history at y=10.08mm and z=1.27mm

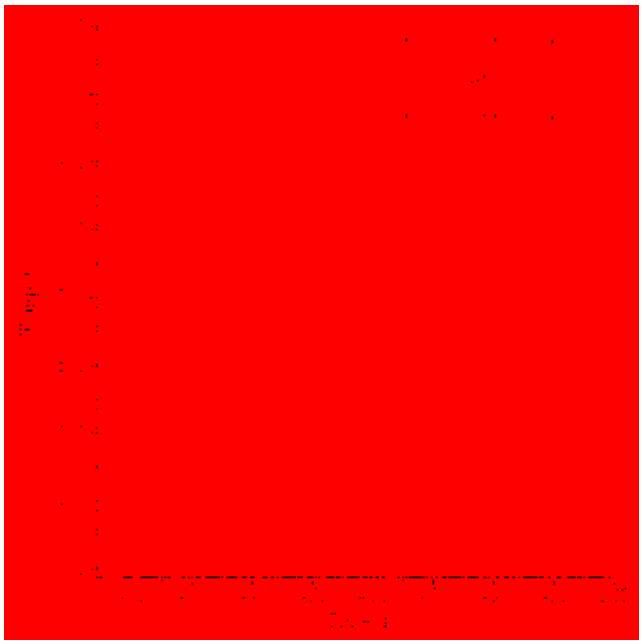

Figure 2-13: Effect of variation of *U* on the thermal history at y=5mm and z=5mm

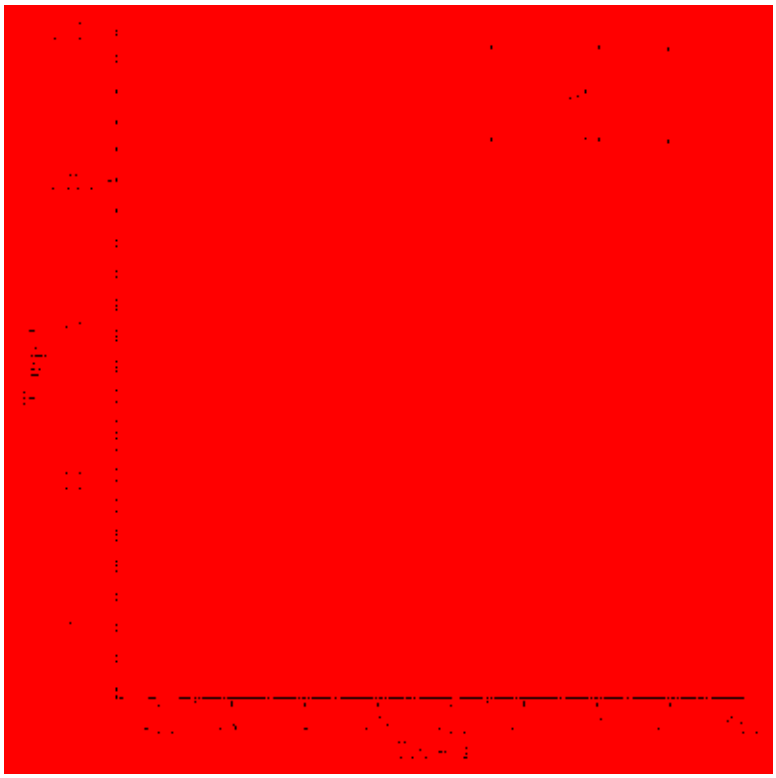

Figure 2-14: Effect of variation of *U* on the thermal history at y=1mm and z=0.5mm

Changing values of U has similar impact at all locations within the workpiece, as demonstrated by the preceding figures. At locations near the bottom surface (see Figure 2-13), U has a somewhat more significant influence over the cooling rate than at other locations.

2.3.3 Effect of Variation in f_o

Variation in the fraction f_o describes the extent to which the local contact resistance between the workpiece and the supporting plate is decreased due to the downward pressure of the FSW tool. It is defined as the ratio of Q_o to Q_{tot}. This parameter affects both the peak temperature and the cooling rate at any given location within the workpiece. Lower values serve to simultaneously reduce the peak temperature and decrease the cooling rate, and higher values do the opposite. The cooling rate is not affected to as great an extent by f_o as it is by U.

The effect of varying f_o is demonstrated by displaying temperature profiles at x = 73.08 cm in the following figures. The parameters used are displayed in each figure, and the y and z locations are described in the captions.

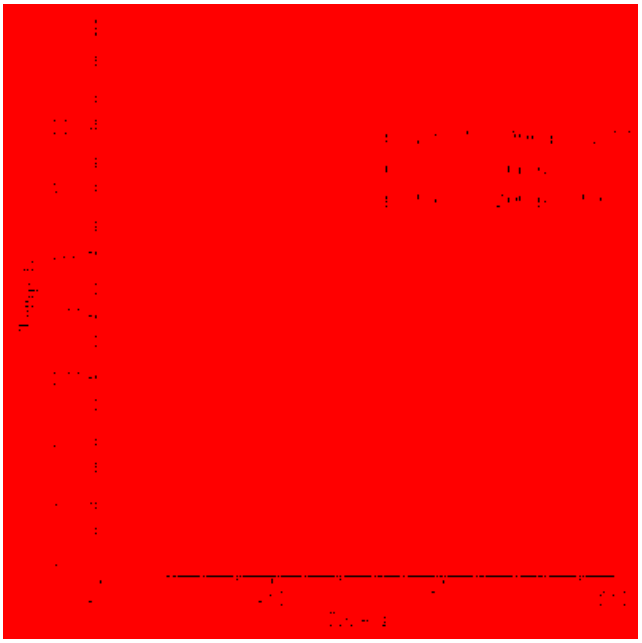

Figure 2-15: Effect of variation of f_o on the thermal history at y=10.08mm and z=1.27mm

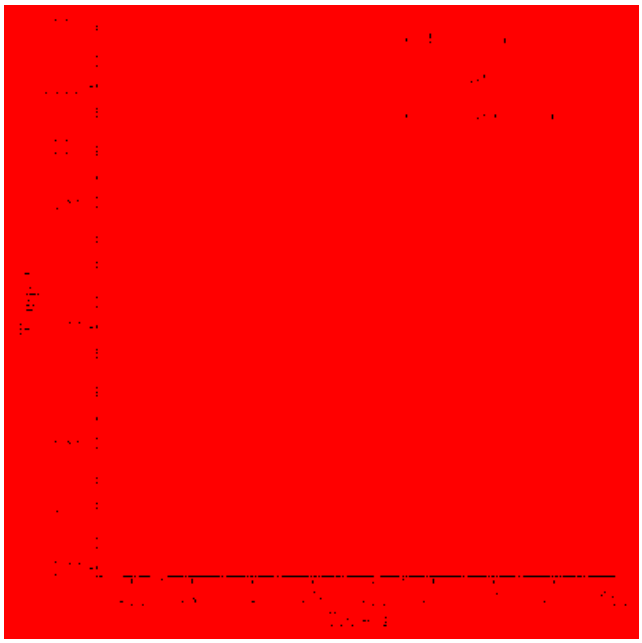

Figure 2-16: Effect of variation of f_o on the thermal history at y=5mm and z=5mm

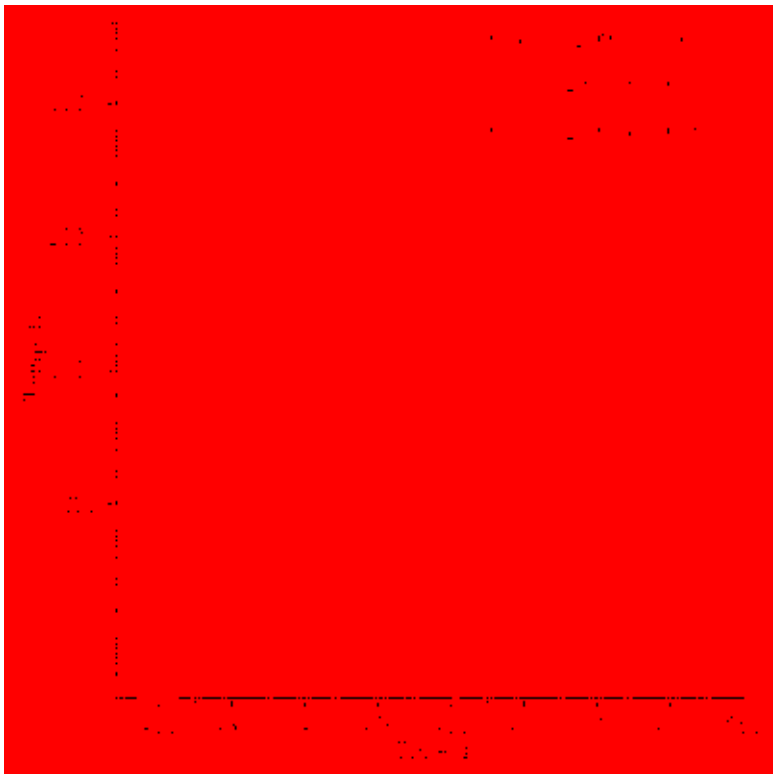

Figure 2-17: Effect of variation of f_o on the thermal history at y=1mm and z=0.5mm

The most apparent increase in significance of f_o is for locations closer to the stirred zone, which is the area most affected by the decrease in workpiece-supporting plate thermal contact resistance. The influence of f_o is reduced at locations farther away from the stirred zone (see Figure 2-15).

2.4 Validation of Model

The analytical model developed was validated with data collected from two different friction stir welding experiments.

2.4.1 Huang Experiment

The first experiment, conducted by Huang (Huang 2008), was performed on a 1.22 m x 0.203 m x .635 cm Inconel 718 plate using a PCBN tool of shoulder diameter 2.54 cm, probe diameter 0.6096 cm, and probe height 0.384 cm. The FSW tool traveled at 2.53 mm/s, rotating at 200 RPM, with a 39.6 kN axial force. 56 thermocouples were placed at various depths and locations within the workpiece to measure the temperature.

2.4.2 Furse Experiment

The second experiment, conducted by Furse (Furse 2010), was performed on a 1.22 m x .203 m x 0.635 cm 304L stainless steel plate using a PCBN tool of shoulder diameter 2.36 cm, probe diameter 0.721 cm, and probe height 0.483 cm. The FSW tool traveled at 1.69 mm/s, rotating at 400 RPM, with a 33.3 kN axial force. Like Huang's experiment, 56 thermocouples were embedded in the workpiece to record the temperature distribution.

2.4.3 Effect of Thermocouple Response

In comparing the thermal model to experimental data, the response of the 0.032 inch grounded K-type thermocouples was taken into consideration. Assuming a first-order response, the temperature of the thermocouple can be described with Equation 2-20, where T_{tc} represents the thermocouple temperature, T_m represents the model temperature of the plate (as calculated from Equation 2-10), and τ represents the time constant of the thermocouple. Lumped into the time constant is the thermal contact resistance between the thermocouple bead and the material of the plate, as well as the thermal capacitance of the thermocouple itself.

$$\frac{dT_{tc}}{dt} = \frac{1}{\tau}(T_m - T_{tc}) \qquad \textbf{2-20}$$

$$T_{tc}(t=0) = T_\infty \quad \text{2-21}$$

Solving Equation 2-20 for T_{tc} with the initial condition, Equation 2-21, yields the following equation.

$$T_{tc} = e^{-\frac{t}{\tau}}\left(\int \frac{T_m}{\tau} e^{\frac{t}{\tau}} dt + T_\infty\right) \quad \text{2-22}$$

The thermocouples used in both experiments were analyzed by Owen (Owen 2006). By measuring the time taken for a thermocouple to reach thermal equilibrium with a large mass of known temperature, it was determined that the time constant value is best approximated as 0.385 s. This resulted in the thermocouple temperature being about 5 K offset from the plate temperature. As can be seen from Figure 2-18, the difference between the temperature response of the thermocouple and the predicted plate temperature is negligible. Figure 2-19 more clearly shows the shift in phase and amplitude of the thermocouple from the plate's predicted temperature. The ADS model was evaluated with the parameters for the Furse weld (Furse 2010) at x = 93.24 cm, y = 10.08 mm, and z = 2.5 mm.

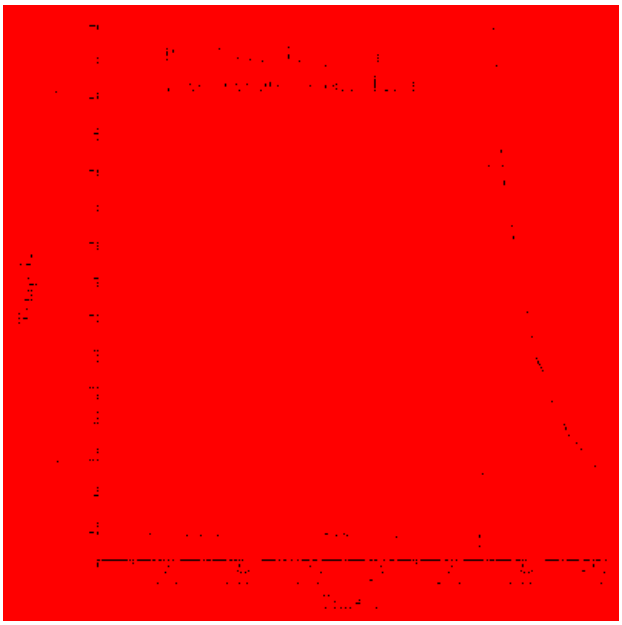

Figure 2-18: Comparison of predicted temperature profiles with a thermocouple time constant of 0.385s

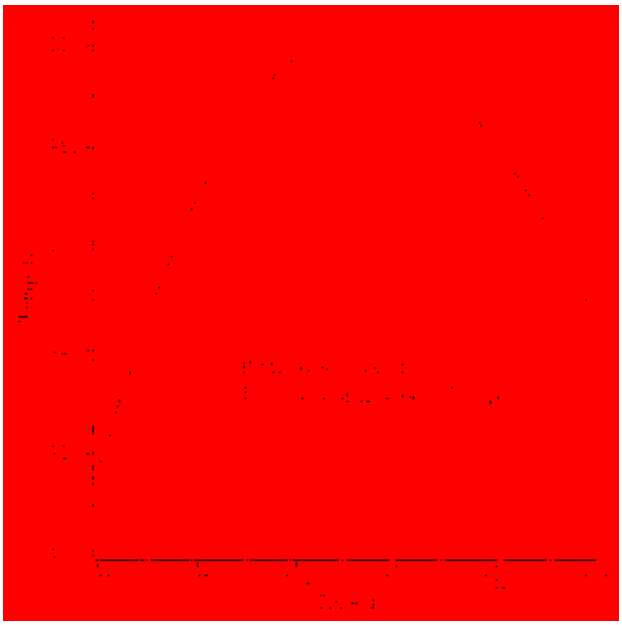

Figure 2-19: Detailed view of the predicted effect of thermocouple response time on temperature profile

2.4.4 Difference in Advancing and Retreating Sides

The temperature field observed in FSW is asymmetrical due to the effect of rotating tool. Temperatures on the advancing side, where the tool is rotating into the direction of the traveling tool, are generally higher compared to the retreating side (Nandan 2006). This effect can be seen in the experimental data shown in the figures below. It is observed that the Huang data is more symmetric across the weld line than the Furse data. In an effort to incorporate the differences in peak temperature across the weld, the model was also optimized to fit the advancing and retreating sides, resulting in different sets of values for the unobservable parameters. In Sections 3.1.3 (for the Huang data) and 3.2.3 (for the Furse data) the thermal history obtained using advancing side parameters will be compared to the advancing side data, and similarly the thermal history obtained using retreating side parameters will be compared to the retreating side data.

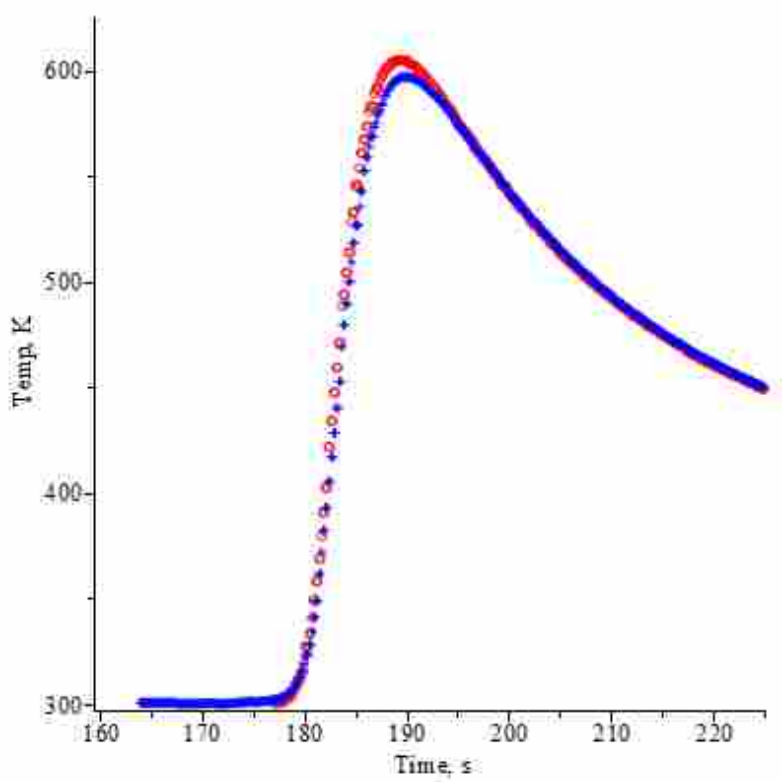

Figure 2-20: Advancing side data (circles) compared to retreating side data (crosses) for Huang data

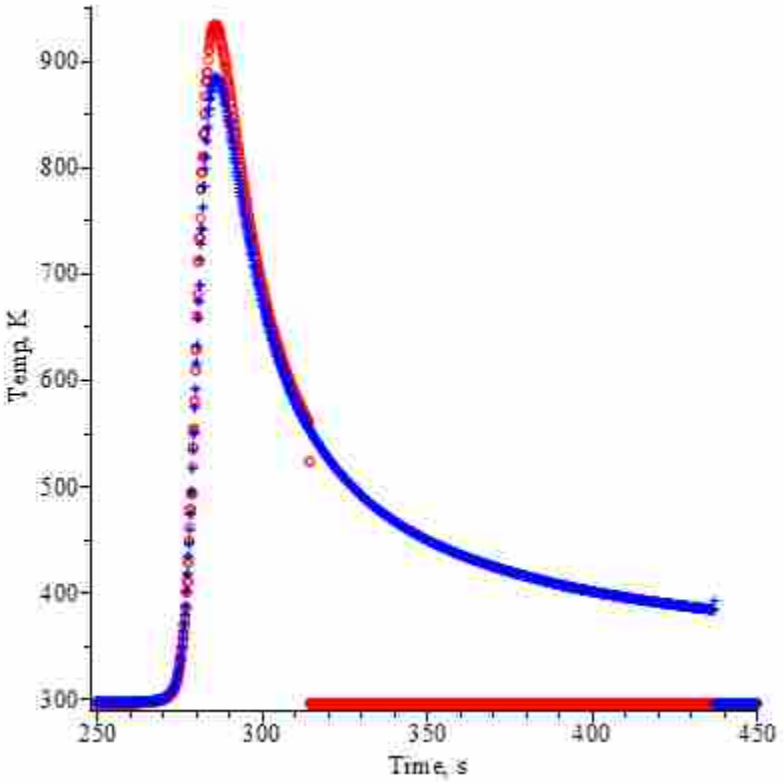

Figure 2-21: Advancing side data (circles) compared to retreating side data (crosses) for Furse data

3 RESULTS

3.1 Comparison to Huang Data

Huang performed FSW on a 1.22 m X 0.203 m X 6.35 mm plate of Inconel 718. 56 holes of varying depths and locations were drilled into the workpiece, into which thermocouples were placed. The polycrystalline cubic boron nitride tool proceeded at 2.53 mm/s, rotating at 200 RPM, and pressing downwards with an approximate 39.6 kN force (Huang 2008). The thermocouple placements are described in Appendix B.

The number of thermocouples used exceeded the number of available data acquisition channels. To obtain pertinent data, thermocouples were disconnected after the FSW tool passed over their location and exchanged with thermocouples located ahead of the tool. Because of this, limited cooling data was obtained, with the exception of the thermocouples located towards the end of the workpiece.

In determining the unobservable parameters, four different thermocouple measurements (different distances from the weld and different depths, namely Holes 4, 15, 19, 41 as shown in Appendix B) were used in the optimization analysis. From this step, f_{therm} was averaged at 0.286, U at 211 W/m^2-K, and f_o at 0.501. The data used for the optimization was not used in the following plots.

3.1.1 Model Comparisons at same Depth

The first series of plots compare the thermal model with data collected at the same depth into the workpiece and at locations progressively closer to the center of the weld line. The model is depicted as a solid red line, and the experimental data as black points. Locations for the thermocouples correspond with the hole numbers listed in Appendix B. Note that the displayed plots are all at locations on the advancing side of the workpiece.

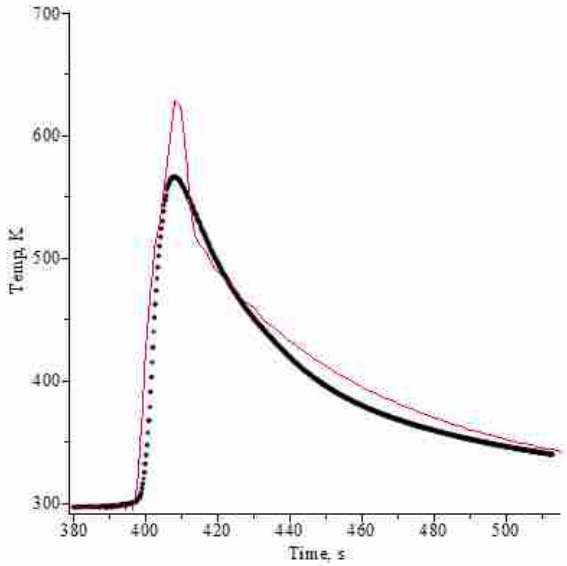

Figure 3-1: Hole 23, 0.1mm beneath top surface

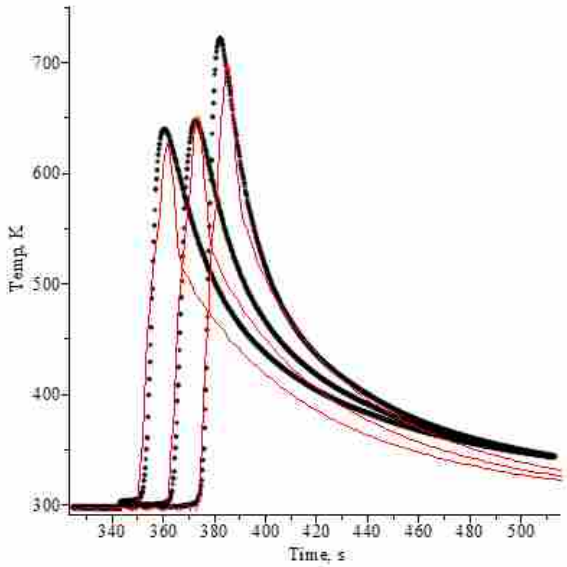

Figure 3-2: Holes 8, 11, and 15, 0.6mm beneath top surface

The effect of the distributed heat source is markedly more pronounced closer to the surface, as Figure 3-1 shows. Also, the predicted peak is overestimated by about 70 K. The predicted peak temperature is more accurate at a depth 0.6 mm (Figure 3-2). However, the predicted cooling rate is more rapid than what was measured.

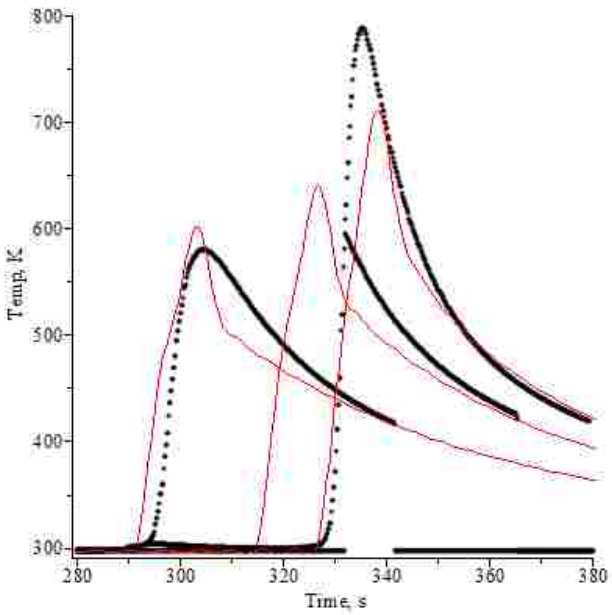

Figure 3-3: Holes 18, 22, and 26, 1.2mm beneath top surface

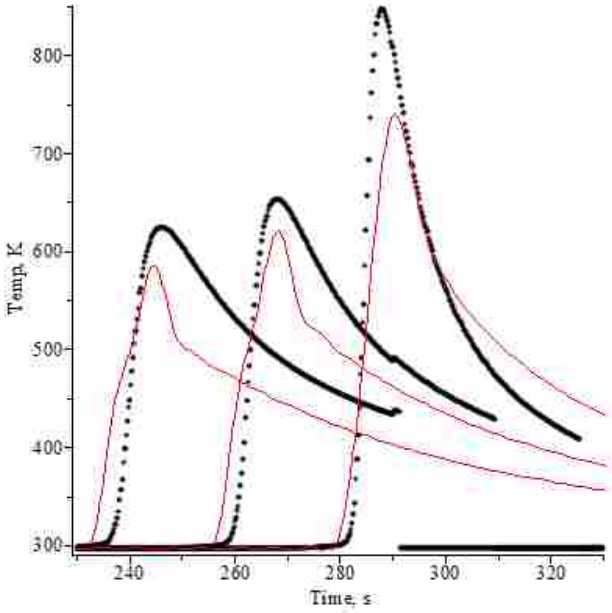

Figure 3-4: Holes 3, 7, and 14, 1.8mm beneath top surface

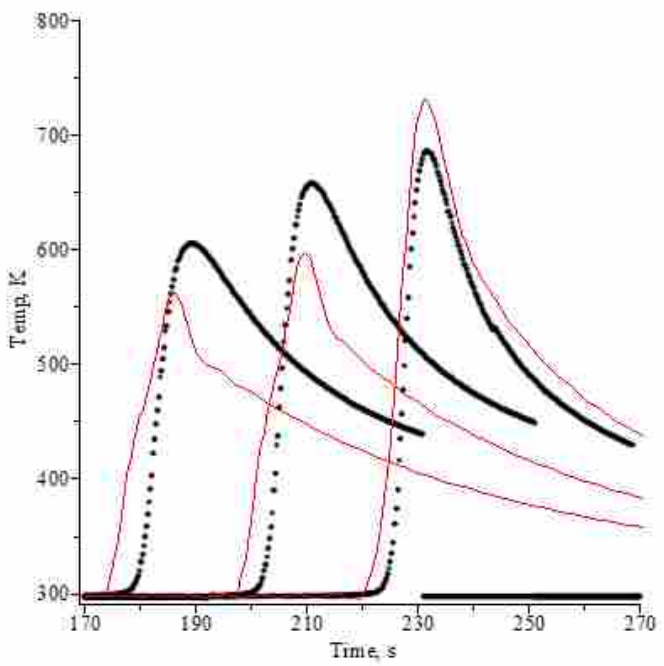

Figure 3-5: Holes 13, 17, and 25, 2.4mm beneath top surface

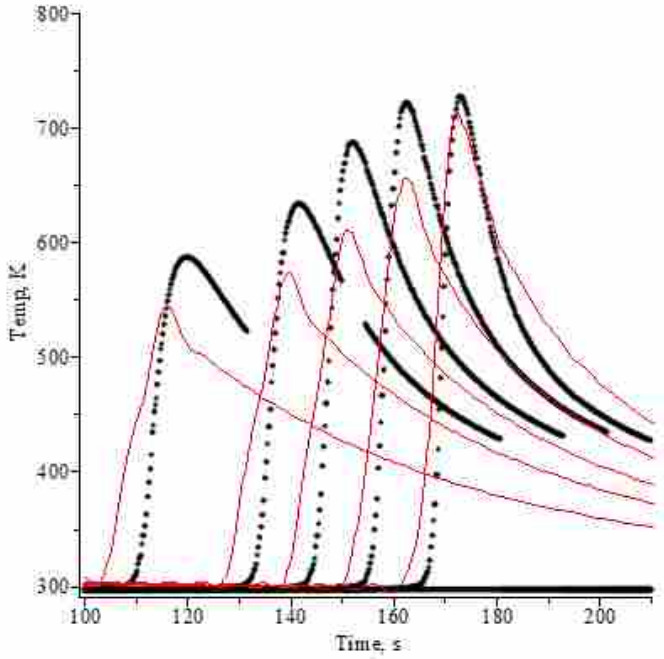

Figure 3-6: Holes 20, 24, 2, 6, and 10, 2.9mm beneath top surface

These plots show more accurate model predictions for the cooling rate, especially at the 2.9 mm depth. Note that peak temperature is underestimated at locations closer to the center of

the weld line. Additionally, locations closer to the center of the weld line have longer predicted cooling periods than measurements show.

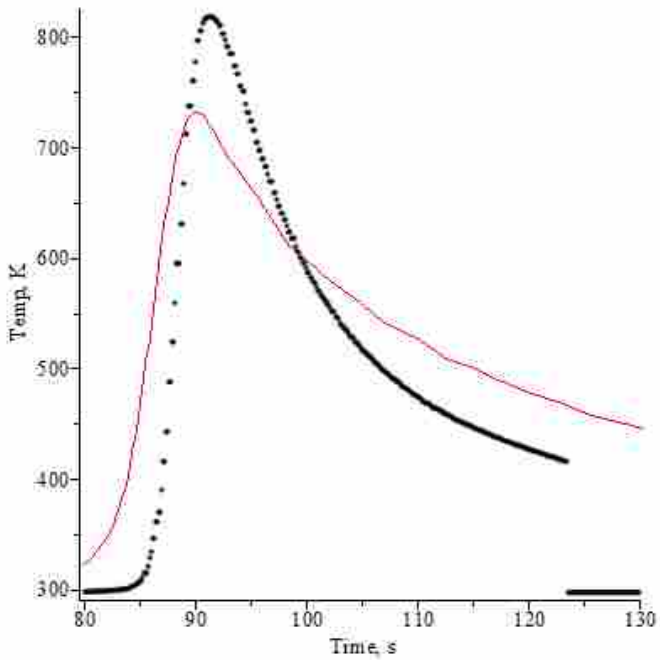

Figure 3-7: Hole 16, 2.95mm beneath top surface

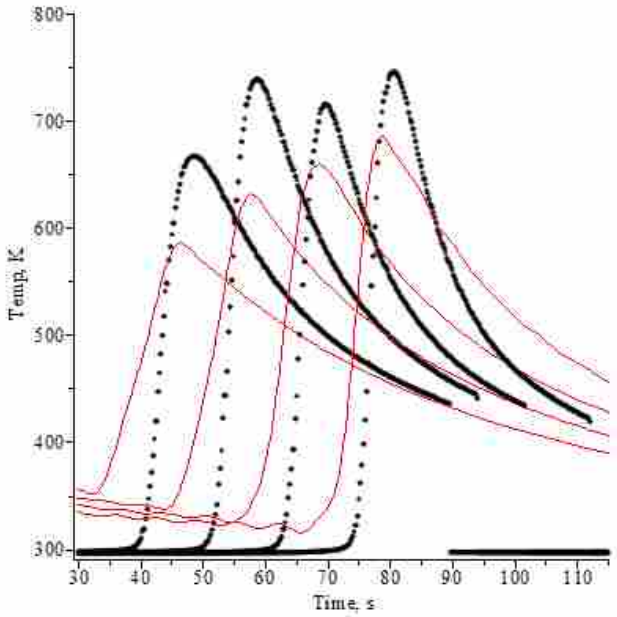

Figure 3-8: Holes 1, 5, 9, and 12, 3.4mm beneath top surface

There are a few general observations that can be made from these plots. First, the predicted peak temperature is at average 40 K below the measured peak. Much larger deviations

are observed closer to the center of the weld line (as time increases the locations of the observed locations on the graphs move towards the center, see Figure 3-1, Figure 3-3, Figure 3-4, and Figure 3-5). Also, the nature of the mathematical techniques used to develop the model results in erroneous temperature values at early times (up to around the first 70 seconds), as seen in Figure 3-8—the solution "rings" more near the system boundaries. While increasing the number of terms used to plot the model can mitigate this ringing to some extent, it cannot eliminate it. Lastly, as the model is evaluated at deeper locations, the cooling trend becomes shallower than observed. Note that at locations above 2.9 mm, the model predicts faster cooling than measured, whereas below this point, the model predicts slower cooling than detected.

3.1.2 Model Comparisons at same Distance from Center Line

The second series of plots compare the model with data at locations progressively closer to the surface of the workpiece. In both series, the model is depicted as a solid red line, while the thermocouple data are depicted as black dots. The hole numbers correspond to the locations of the thermocouples shown in Appendix B. Only advancing side data were used in the following plots.

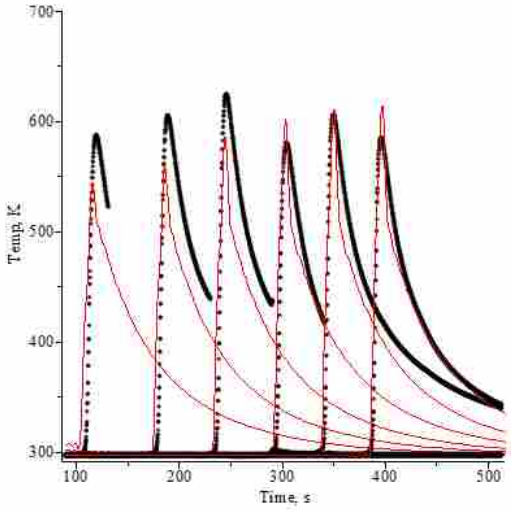

Figure 3-9: Holes 20, 13, 3, 18, 4, and 19, 10.25mm from center of weld line

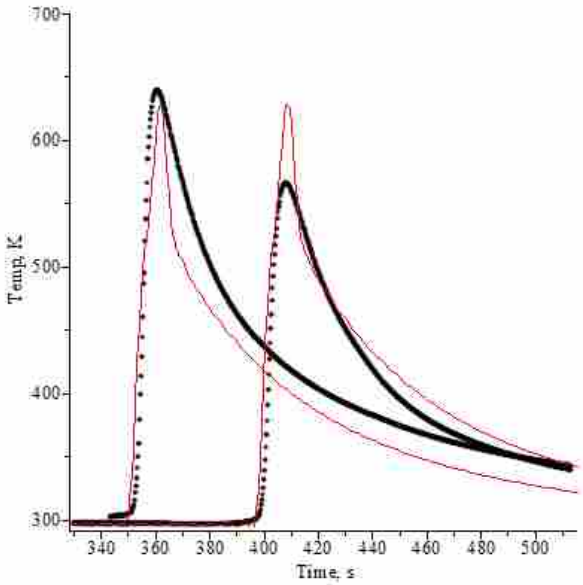

Figure 3-10: Holes 8 and 23, 9.65mm from center of weld line

The model fairly accurately predicts peak temperature at these locations farther from the center of the weld line, within about 30 K. Again, Hole 23, as seen in Figure 3-10, exhibits the effect of the distributed heat source, being close to the surface of the workpiece, with the high peak temperature rapidly diminishing once the tool passes by. With the exception of this location, the cooling rate predicted by the model is more rapid than that measured experimentally.

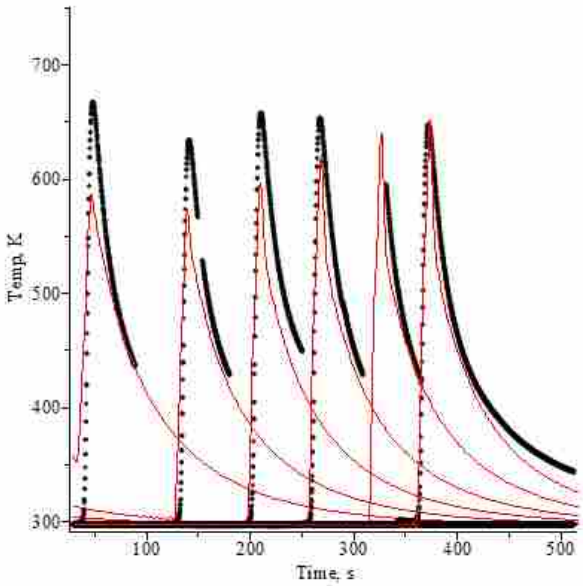

Figure 3-11: Holes 1, 24, 17, 7, 22, and 11, 8.75mm from center of weld line

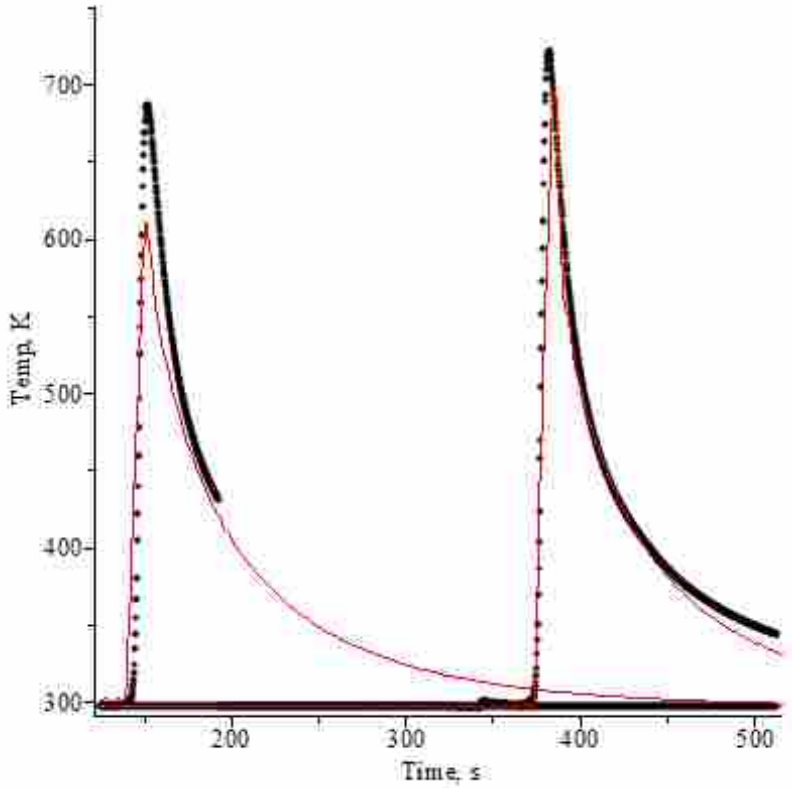

Figure 3-12: Holes 2 and 15, 6.85mm from center of weld line

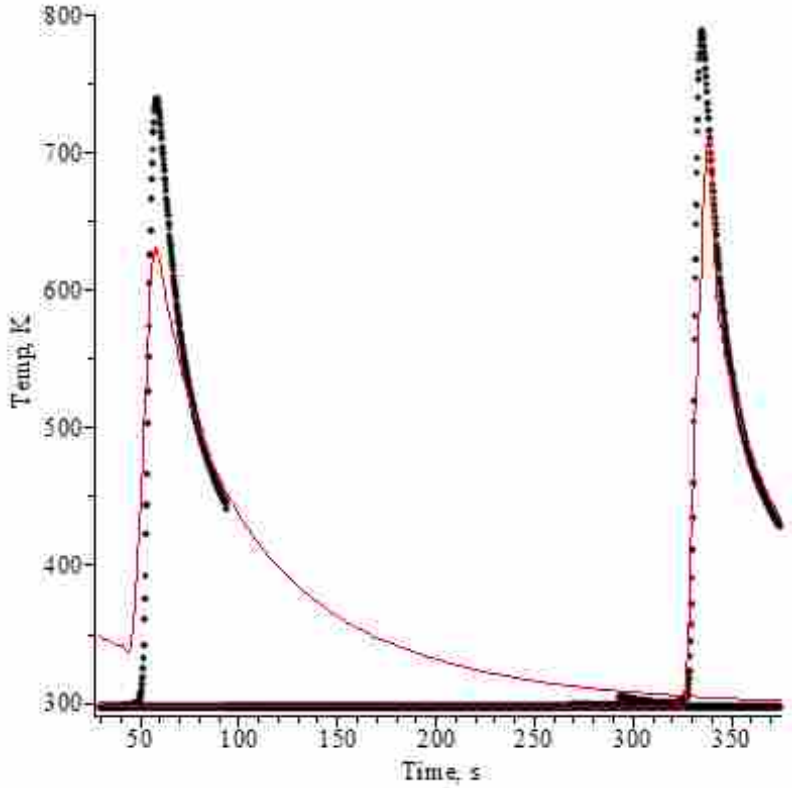

Figure 3-13: Holes 5 and 26, 5.8mm from center of weld line

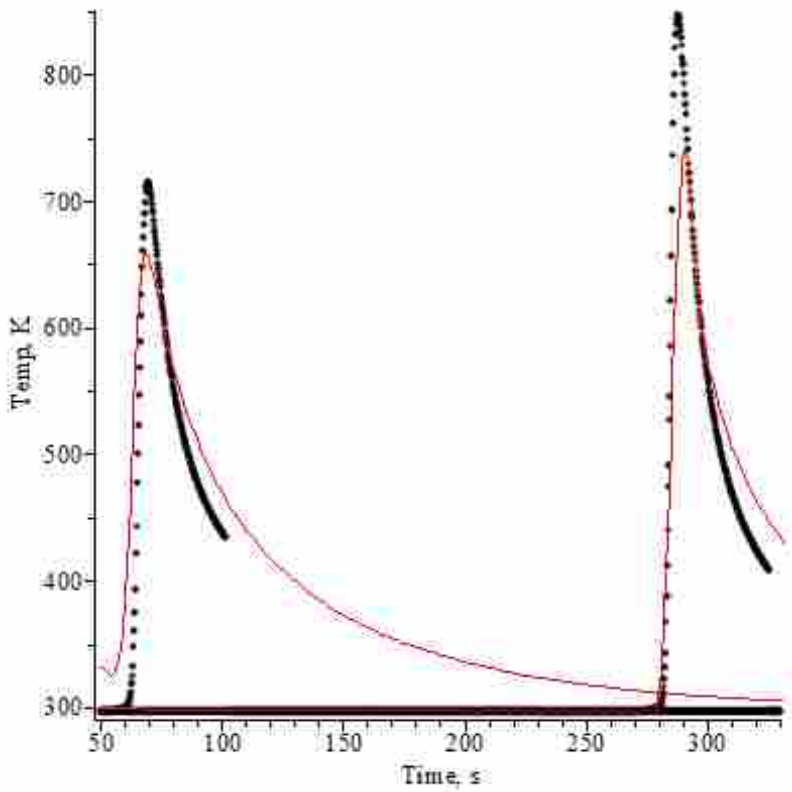

Figure 3-14: Holes 9 and 14, 3.35mm from center of weld line

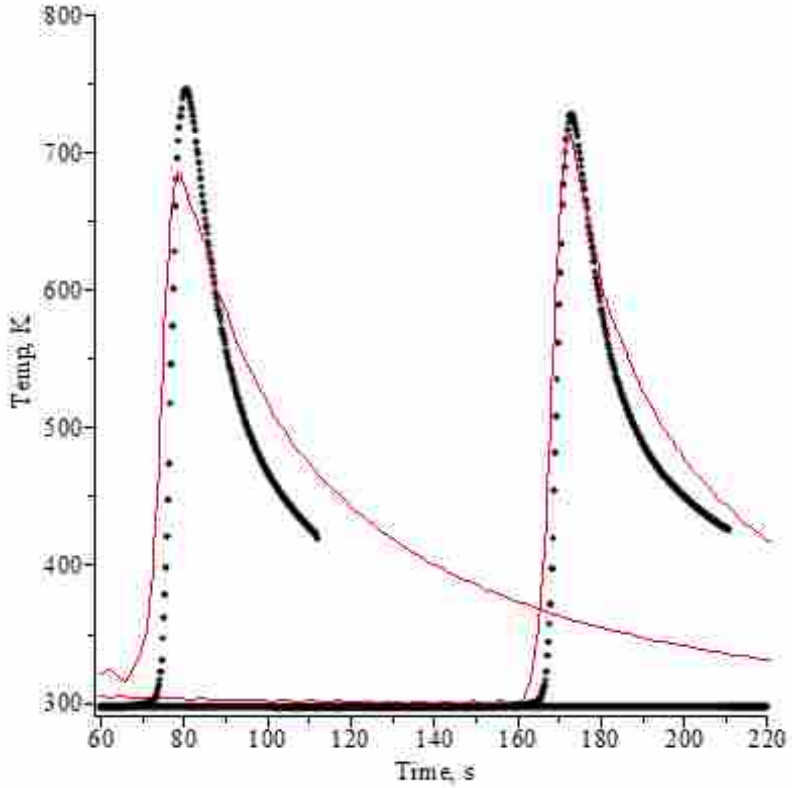

Figure 3-15: Holes 10 and 12, 1.32 mm from center of weld line

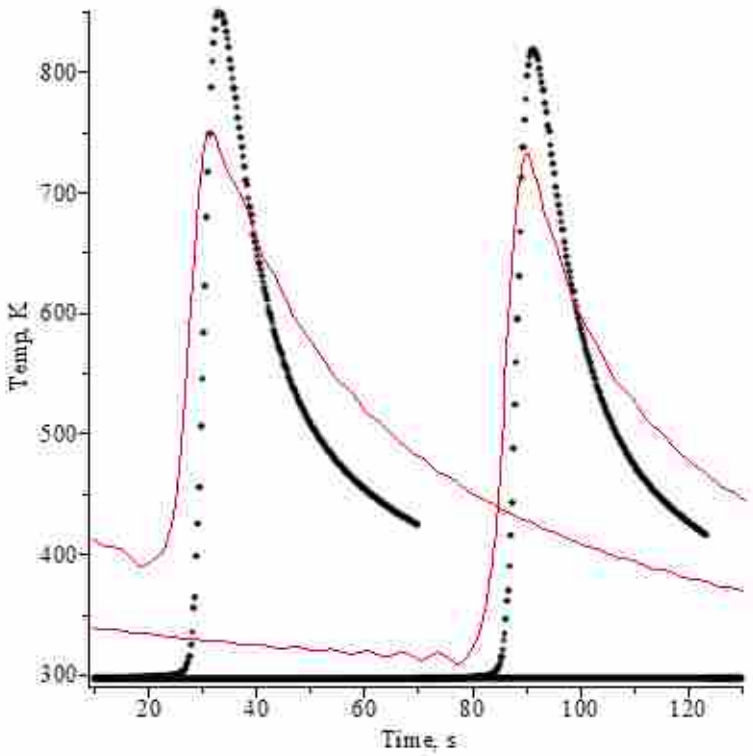

Figure 3-16: Holes 16 and 27, directly on center of weld line

These plots demonstrate that at locations closer to the center of the weld line, the model underestimates the rate of cooling, while at locations farther out, the model overestimates this rate. The accuracy of the predicted peak temperature is more influenced by the depth with in the workpiece, rather than the distance to the center of the weld line.

3.1.3 Model Comparisons Across Weld Line

The third series of plots compare the thermal model with data collected at equal distances on opposite sides of the center of the weld line. The advancing side results are shown in red, while the retreating side results are shown in blue. Modeled temperatures are depicted with dashed lines, and data are shown as with points.

As discussed in Section 2.4.4, the model was also trained to best fit advancing and retreating sides, rather than averaging parameters across the entire weld as was done in the

previous sections. The values of the parameters for the advancing side data used in calculating the model were obtained from Holes 33, 37, 41, and 49. The obtained parameters were averaged, with f_{therm} as 0.446, U as 142 W/m^2-K, and f_o as 0.570.

The values of the parameters for the retreating side data used in calculating the model were obtained from Holes 4, 8, 11, and 19. The obtained parameters were averaged, with f_{therm} as 0.497, U as 149 W/m^2-K, and f_o as 0.683. Note that this difference in parameters can have a significant effect on the resulting model predictions. In the case of this experiment, which was fairly symmetrical across the weld line, training to the advancing and retreating sides of the weld separately had a negative impact on the fit to the measured data, as can be seen in the following plots.

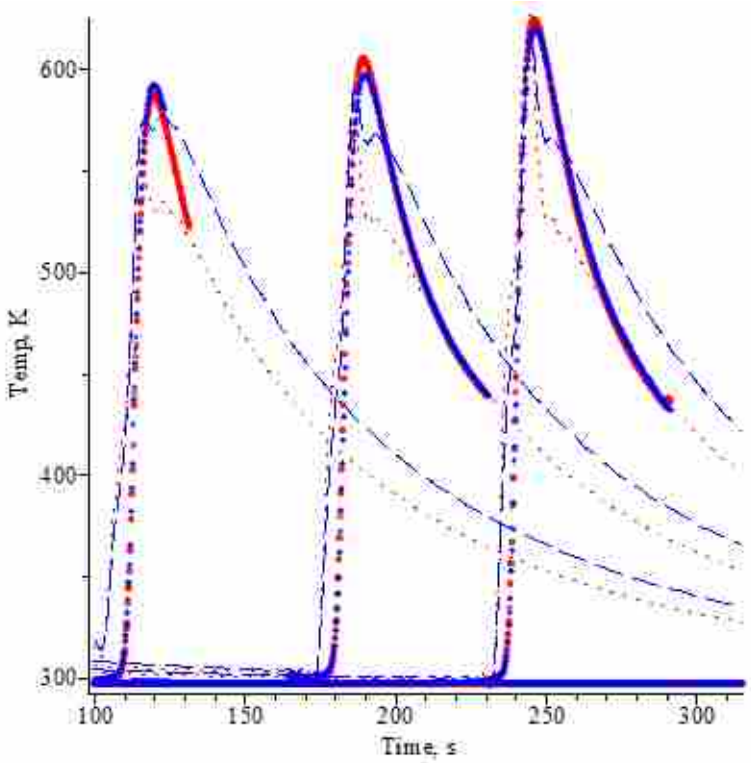

Figure 3-17: Pairs 20-46, 13-43, and 3-32, 10.15mm from center of weld line

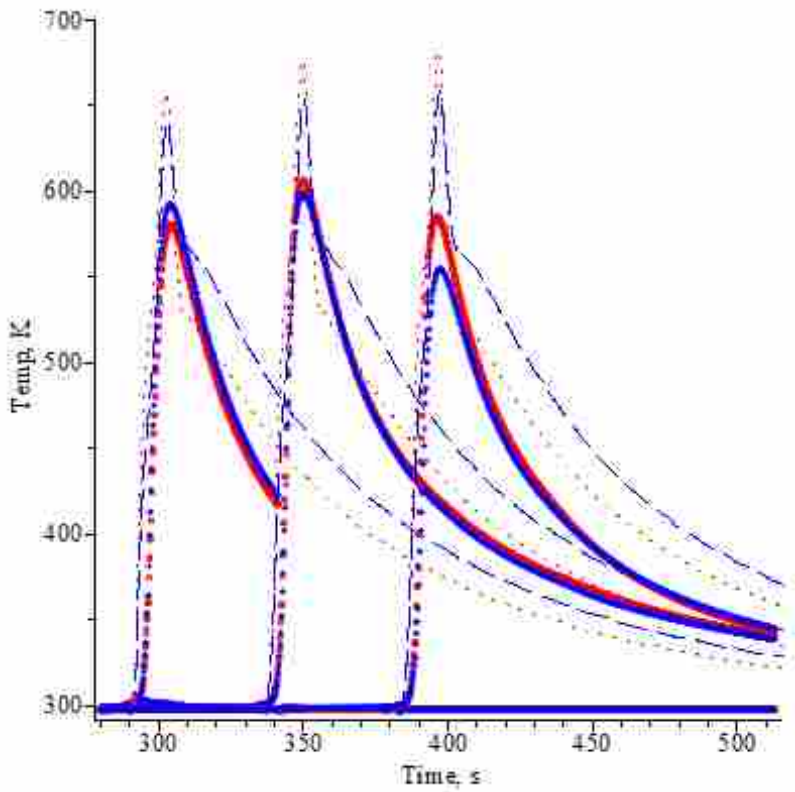

Figure 3-18: Pairs 18-48, 4-33, and 19-49, 10.15mm from center of weld line

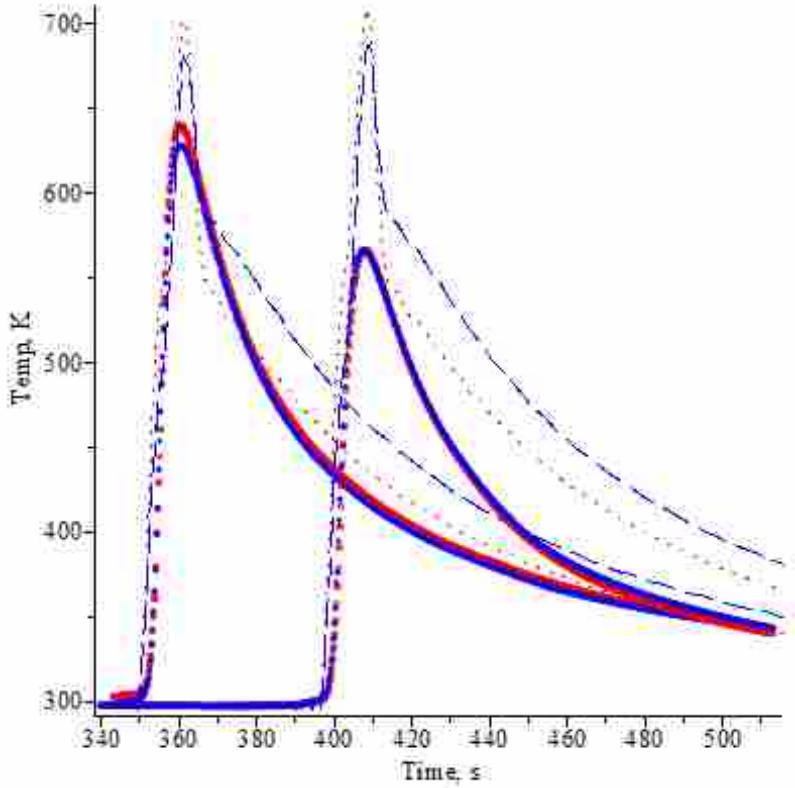

Figure 3-19: Pairs 8-37 and 23-29, 9.65mm from center of weld line

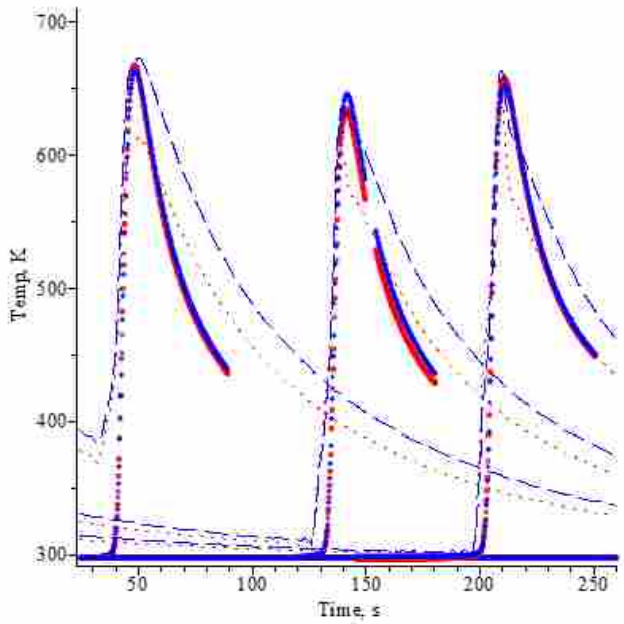

Figure 3-20: Pairs 1-30, 24-50, and 17-47, 8.75mm from center of weld line

The data from this experiment show a minimal temperature difference (at most 15 K) between the advancing and retreating sides of the FSW process. Seven cases of the eleven shown above demonstrate a higher peak temperature on the advancing side, and three cases show a higher temperature on the retreating side.

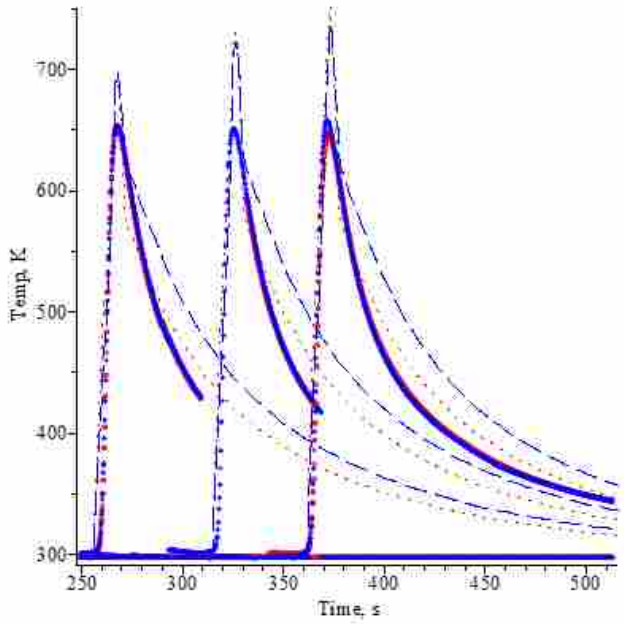

Figure 3-21: Pairs 7-36, 22-28, and 11-41, 8.75mm from center of weld line

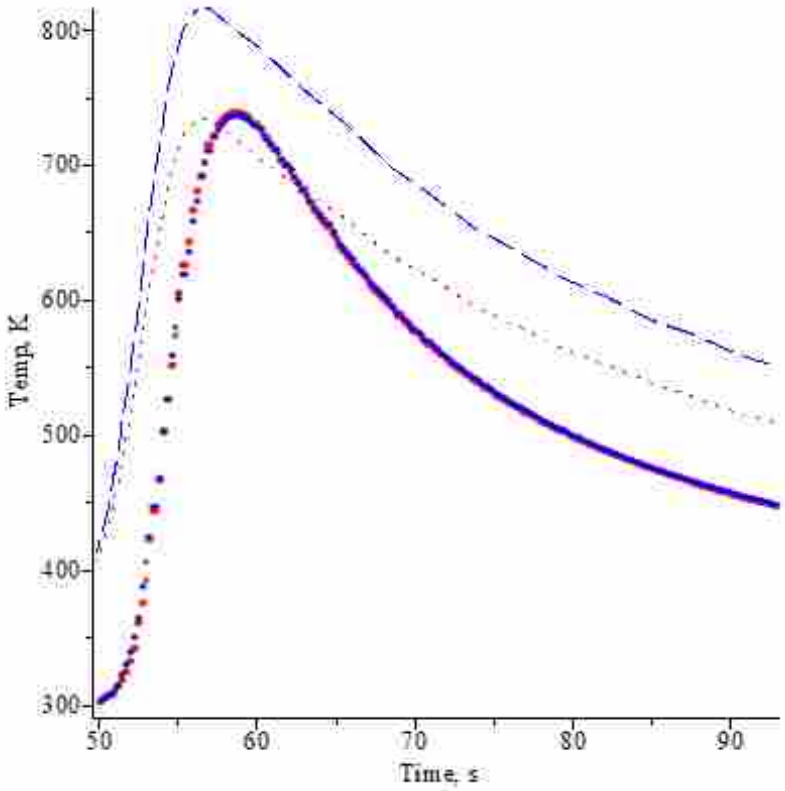

Figure 3-22: Pair 5-34, 5.4mm from center of weld line

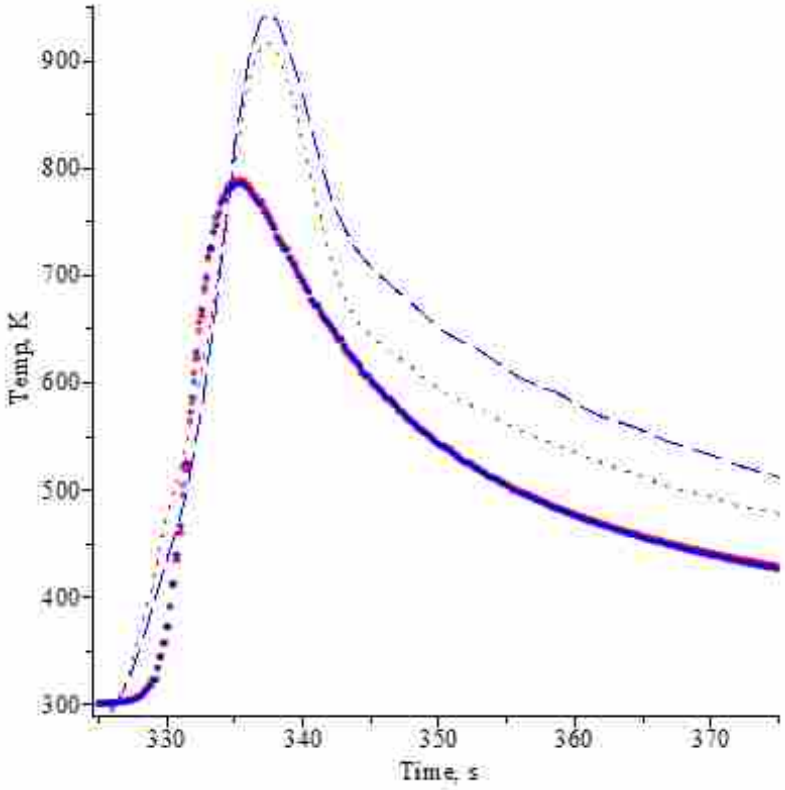

Figure 3-23: Pair 26-52, 5.4 mm from center of weld line

The average value of the squared summed residuals for the model as compared to the temperature data obtained by Huang is 1.35 x 10^7 K^2, corresponding to an overall average error of 76 K.

3.2 Comparison to Furse Data

Furse performed FSW on a 1.22 m X 0.203 m X 6.35 mm plate of 304L stainless steel. 56 holes of varying depths and locations were drilled into the workpiece, into which thermocouples were placed. The polycrystalline boron nitride tool travelled at 1.69 mm/s, rotating at 400 RPM, and with a controlled axial force of 33.3 kN. The locations for the thermocouples are shown in Appendix C.

Four different thermocouple measurements (Holes 4, 16, 39, 50 as shown in Appendix C) were used in the optimization analysis to determine the unobservable parameters for the model. These parameter values used were averaged from the results of the optimization analysis. The fraction f_{therm} was approximated at 0.695, U at 166 W/m^2-K, and f_o at 0.716. Again, the data used to determine these parameters was not used to validate the model.

3.2.1 Model Comparisons at same Depth

The first series of plots compare the thermal model with data collected at the same depth into the workpiece and at locations progressively closer to the center of the weld line. The model is depicted as a solid red line, and the experimental data as black points. Locations for the thermocouples correspond with the hole numbers listed in Appendix C. Note that the displayed plots are all at locations on the advancing side of the workpiece.

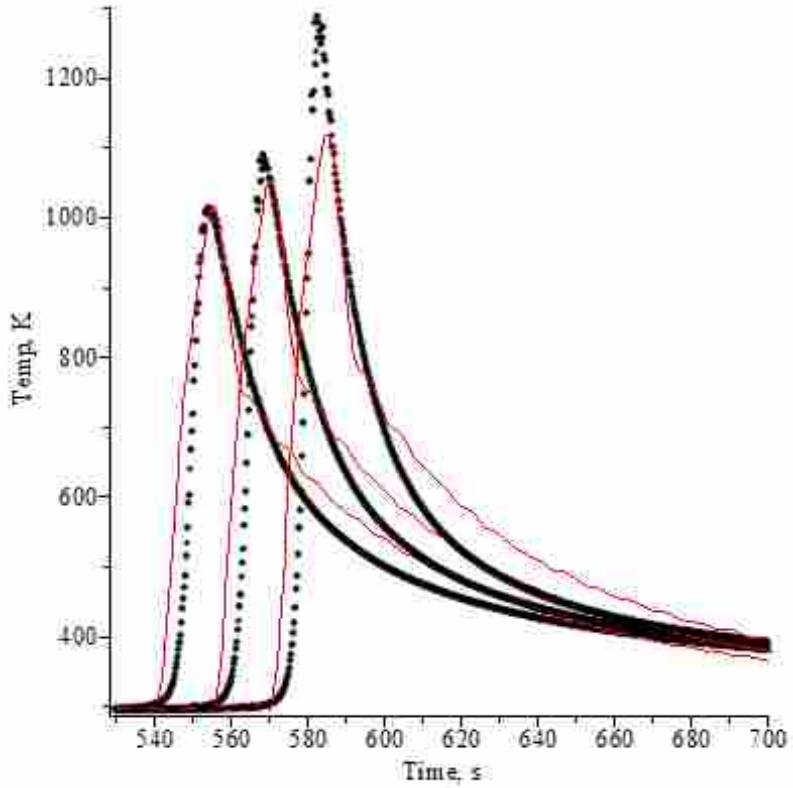

Figure 3-24: Holes 20, 23, and 26, 0.25mm beneath top surface

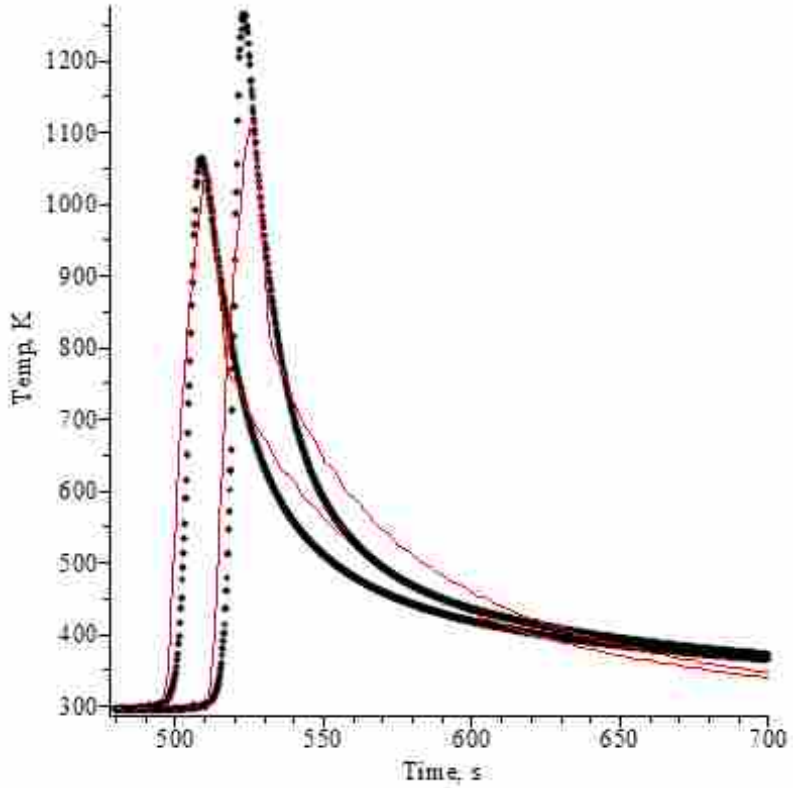

Figure 3-25: Holes 8 and 12, 0.76mm beneath top surface

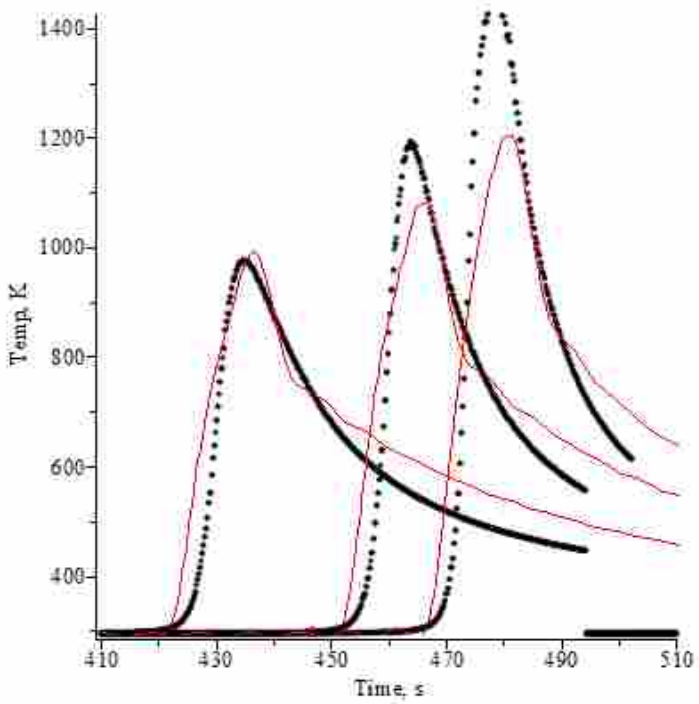

Figure 3-26: Holes 19, 22, and 25, 1.27mm beneath top surface

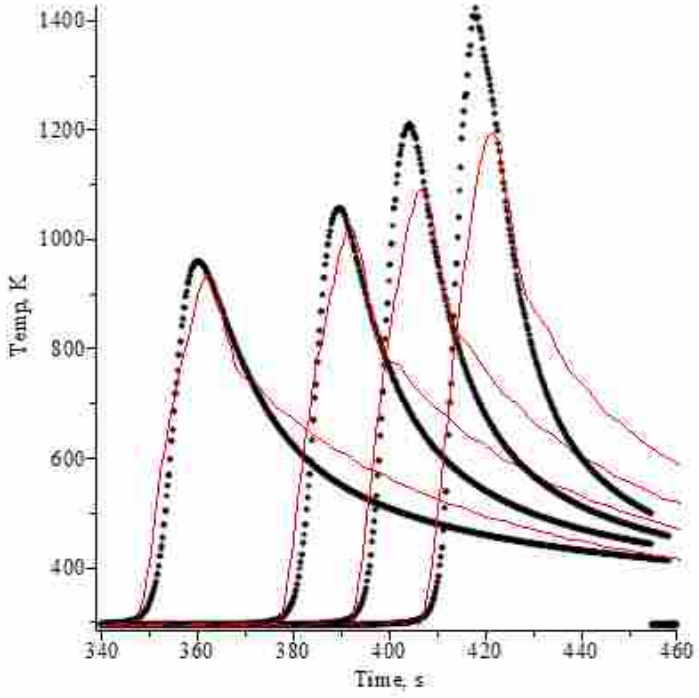

Figure 3-27: Holes 3, 7, 11, and 15, 2.29mm beneath top surface

At these relatively shallow locations, the model underestimates the peak temperature compared to thermocouple measurements. Additionally, the degree to which the peak

temperature is underestimated is increased at locations closer to the center of the weld line. The cooling rate predicted by the model is also significantly higher than the measured cooling rate.

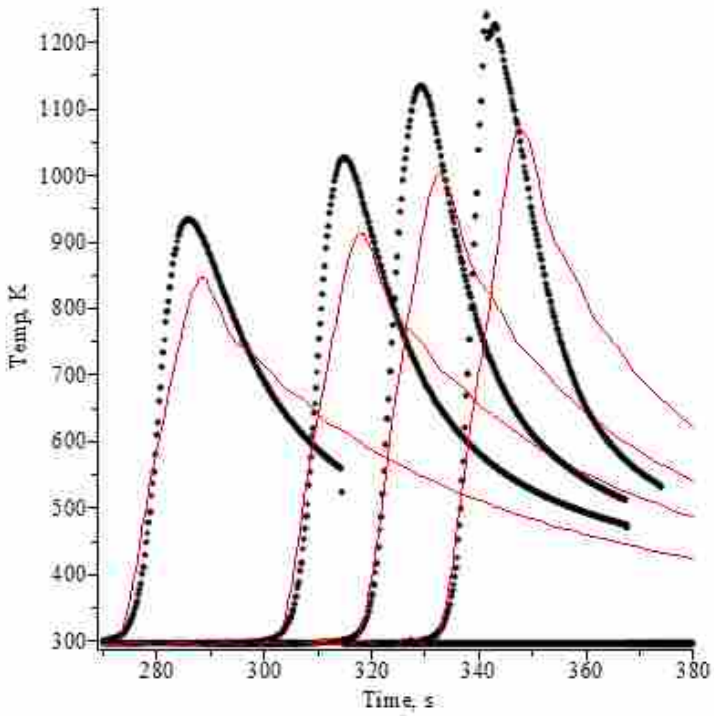

Figure 3-28: Holes 14, 18, 21, and 24, 3.3mm beneath top surface

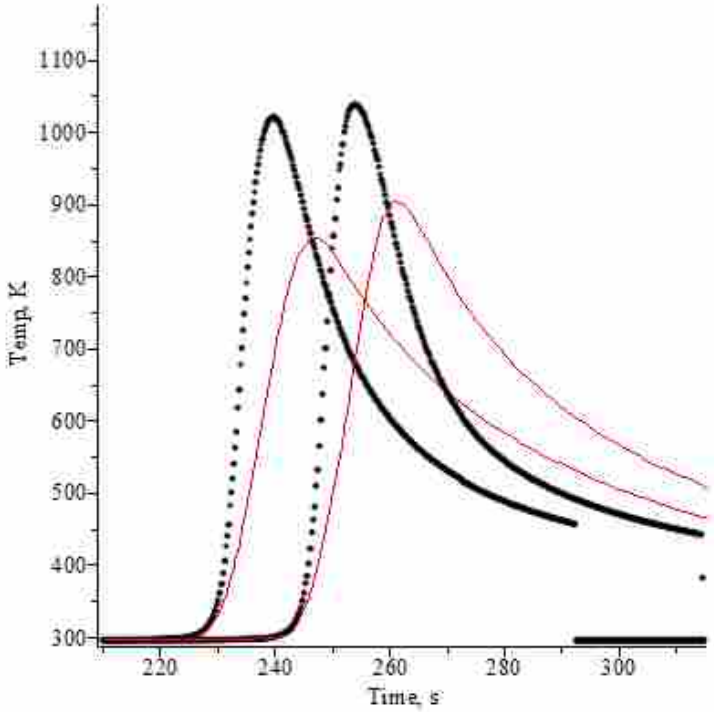

Figure 3-29: Holes 2 and 6, 4.32mm beneath top surface

At these moderate depths within the workpiece, the peak temperature is more accurately predicted than at the depths seen in Figure 3-24 through Figure 3-27. It is also of interest to note that the model predicts a longer heating period than that measured. At these depths, the model overestimates the length of the cooling period as well.

Unlike with the comparison to Huang's experiment, there are significant deviations in the predicted peak temperature. Generally, at locations deeper than 4.32mm, the model overestimates the peak temperature, while above this point the model underestimates, sometimes by as much as 200 K. Additionally, the initial ramp in temperature is predicted to be much slower than observed in the measured data at these deep locations closer to the backing plate. Similar to the comparison with Huang's experiment, the model has best agreement with the cooling rate at moderate depths, overestimating the rate at shallower depths while underestimating below 3.3mm.

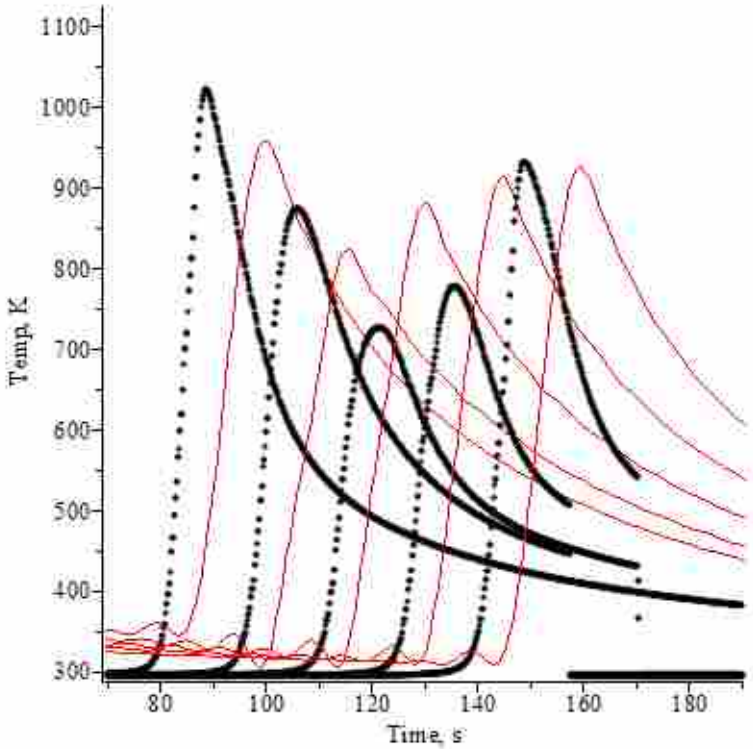

Figure 3-30: Holes 27, 1, 5, 9, and 13, 5.08mm beneath top surface

3.2.2 Model Comparisons at same Distance from Center Line

The second series of plots compare the model with data at locations progressively closer to the surface of the workpiece. In both series, the model is depicted as a solid red line, while the thermocouple data are depicted as black dots. The hole numbers correspond to the locations of the thermocouples shown in Appendix C. Only advancing side data were used in the following plots.

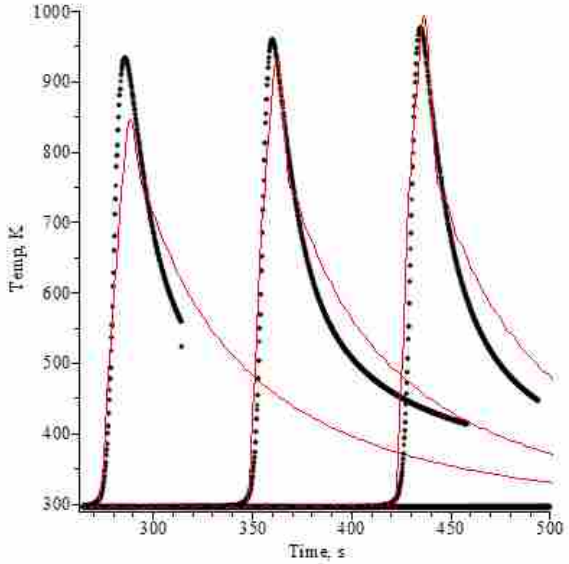

Figure 3-31: Holes 14, 3, and 19, 10.08mm from center of weld line

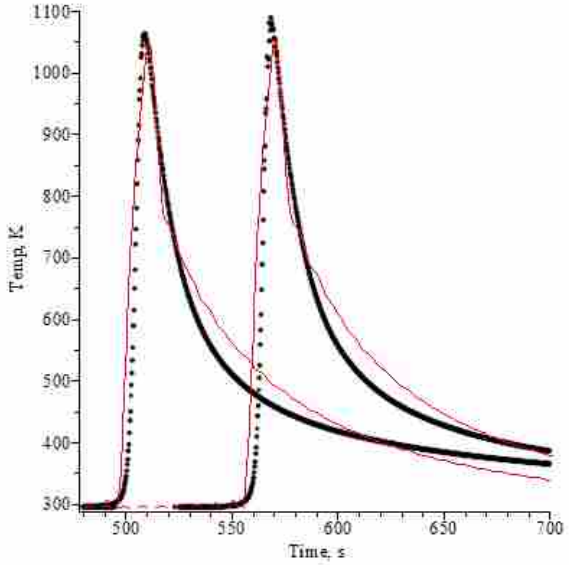

Figure 3-32: Holes 8 and 23, 9.58mm from center of weld line

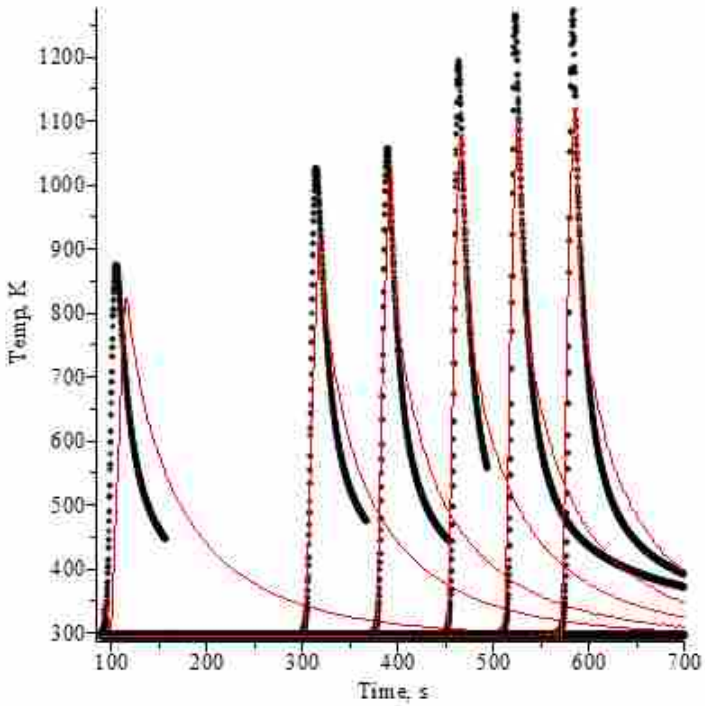

Figure 3-33: Holes 1, 18, 7, 22, 12, and 26, 8.57mm from center of weld line

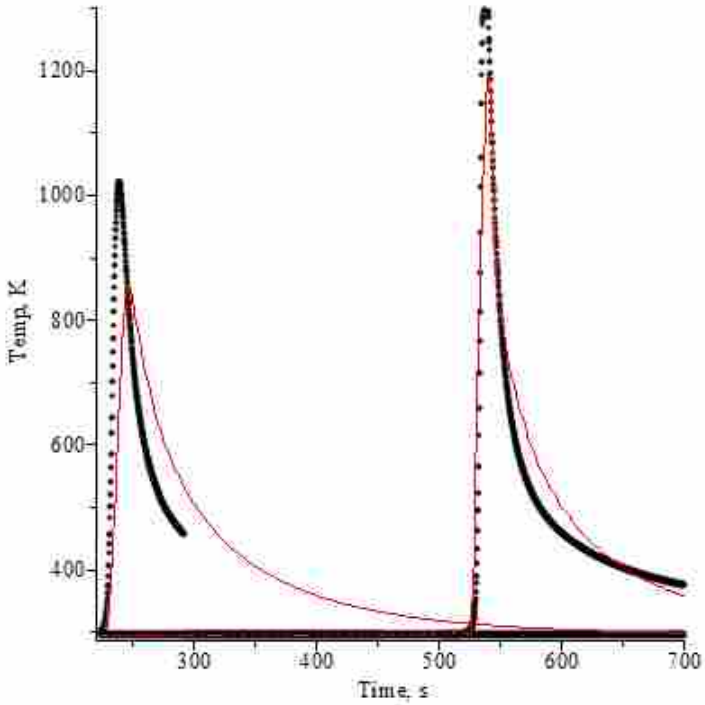

Figure 3-34: Holes 2 and 16, 6.8mm from center of weld line

Figure 3-31 shows that the model underestimates the peak temperature by approximately 50 K 10.08 mm outside of the center of the weld line. The cooling rate is predicted to be more

rapid than the measured rate is from 8.57 mm and farther out. The peak temperature is underestimated to a greater extent at locations closer to the center of the weld line. Figure 3-34 indicates that at 6.8 mm from the center of the weld line, the model begins to predict longer cooling periods than that which is measured.

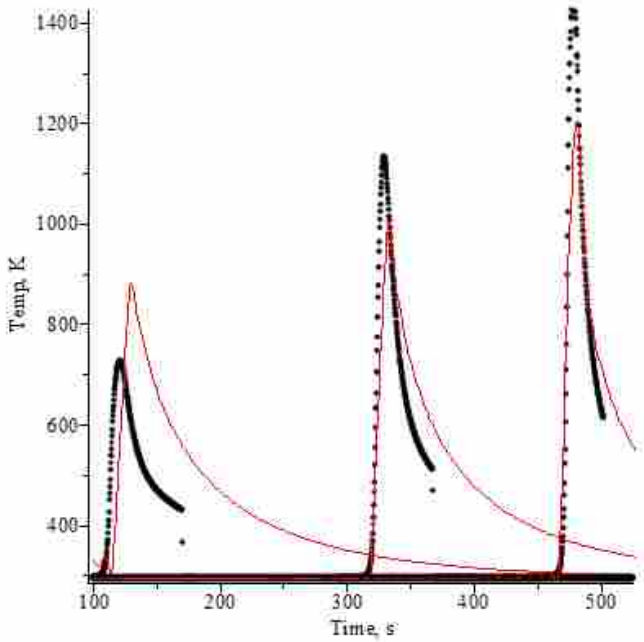

Figure 3-35: Holes 5, 21, and 25, 5.8mm from center of weld line

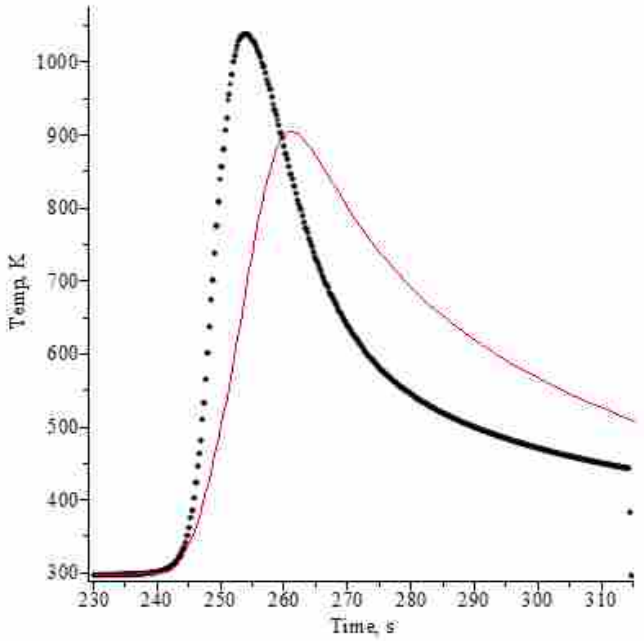

Figure 3-36: Hole 6, 4.54mm from center of weld line

Figure 3-35 demonstrates that the model is most accurate at predicting the peak temperature at depths near the center of the workpiece. Hole 5 is located at a 5.1 mm depth, and the model overestimates the peak temperature there. Hole 21 is located at a 3.3 mm depth, and the model closely predicts the peak temperature at that location. Hole 25 is located at a 1.3 mm depth, and the model underestimates the peak temperature there. In both of the preceding figures, the cooling rate is predicted by the model to be longer than measured data shows.

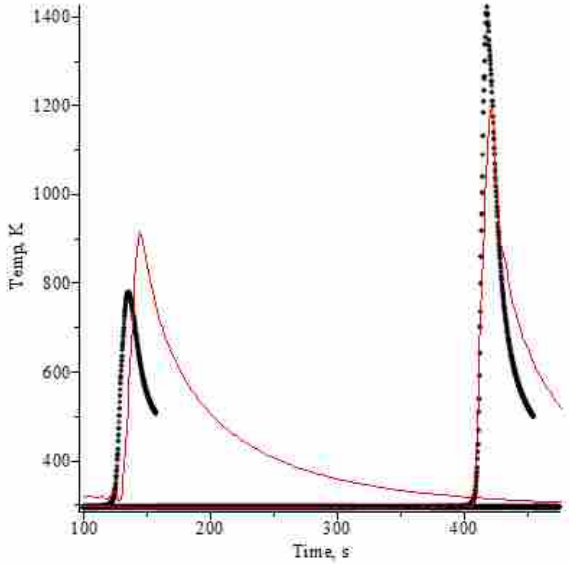

Figure 3-37: Holes 9 and 15, 3.28mm from center of weld line

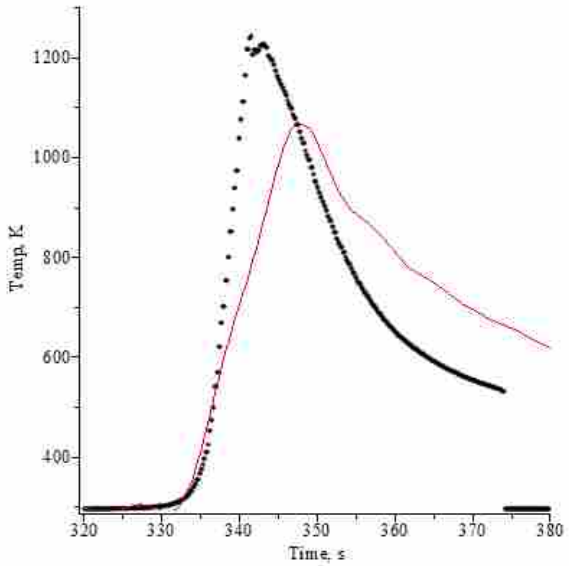

Figure 3-38: Hole 24, 2.27mm from center of weld line

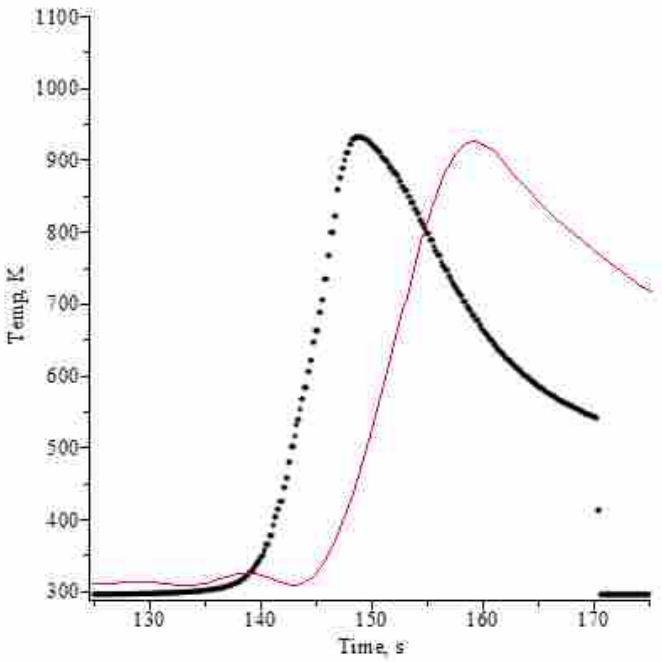

Figure 3-39: Hole 13, 1.26 mm from center of weld line

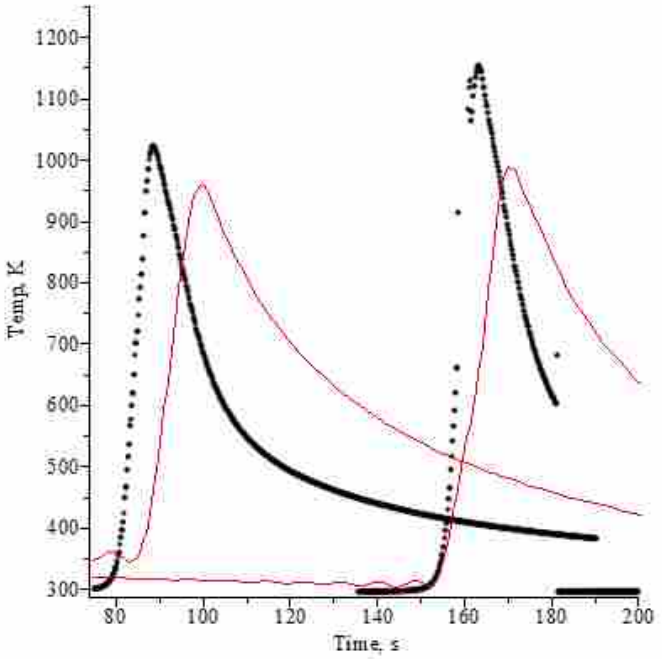

Figure 3-40: Holes 27 and 17, directly on center of weld line

Generally, the model underestimates the peak temperature (by as much as 300 K) at locations farther out than 4.54mm from the center of the weld line. Within this distance, the model overestimates the peak temperature (by as much as 100 K).

3.2.3 Model Comparisons Across the Weld Line

The third series of plots compare the thermal model with data collected at equal distances on opposite sides of the center of the weld line. The advancing side results are shown in red, while the retreating side results are shown in blue. Modeled temperatures are depicted with dashed lines, and data are shown as with points.

As discussed in Section 2.4.4, the model was also trained to best fit advancing and retreating sides, rather than averaging parameters across the entire weld as was done in the previous sections. The values of the parameters for the advancing side data used in calculating the model were obtained from Holes 33, 39, and 50. The obtained parameters were averaged, with f_{therm} as 0.668, U as 211 W/m^2-K, and f_o as 0.594.

The values of the parameters for the retreating side data used in calculating the model were obtained from Holes 4, 12, 16, and 26 (see Appendix C). The obtained parameters were averaged, with f_{therm} as 0.638, U as 166 W/m^2-K, and f_o as 0.716. Note that this difference in parameters can have a significant effect on the resulting model predictions. In the case of this experiment, which demonstrated some amount of asymmetry across the weld line, treating the advancing and retreating sides independently enhances the accuracy of the predicted temperatures as compared to the parameters used in the preceding sections. The difference in temperatures between the retreating and advancing sides can be quite large in some locations, as shown in the following plots (sometimes on the order of 100 K).

The temperature profiles calculated from the ADS model are presented in descending distance from the center of the weld line.

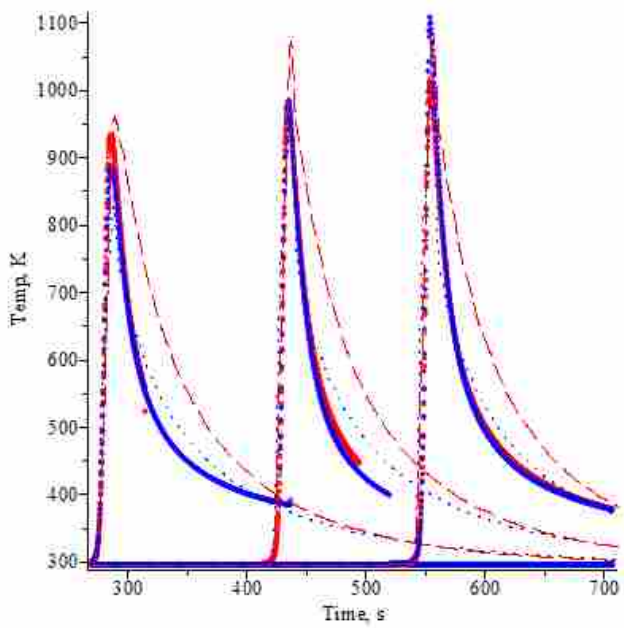

Figure 3-41: Pairs 14-41, 19-45, and 20-46, 10.08mm from center of weld line

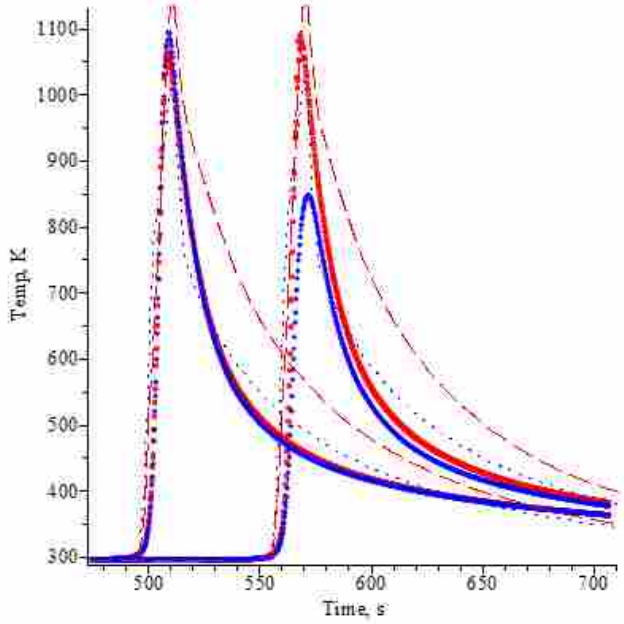

Figure 3-42: Pairs 8-36 and 23-30, 9.58mm from center of weld line

As can be seen from the preceding figures, this experiment demonstrated a greater difference in temperature between the advancing and retreating sides. Since the model was developed with a symmetric boundary condition, it does not account for this variation. Collected

data were somewhat inconsistent, as some cases show higher temperatures on the advancing side, and others show higher temperatures on the retreating side.

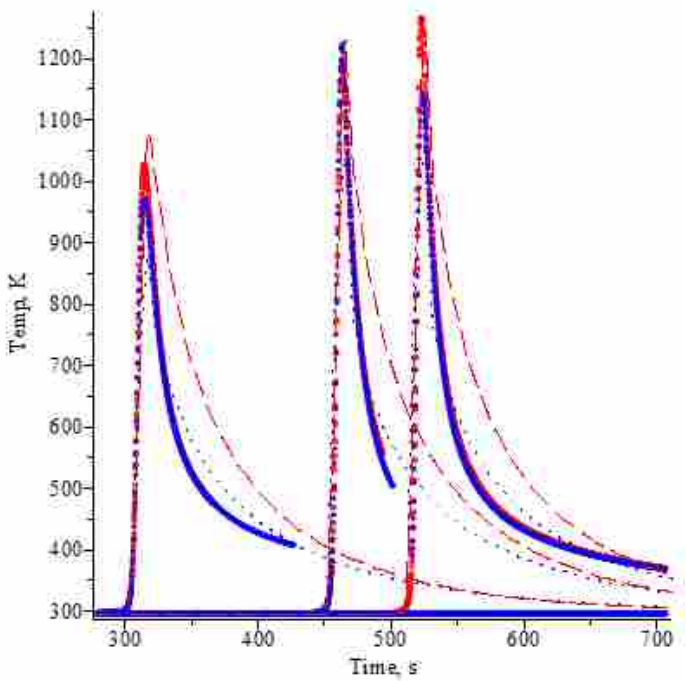

Figure 3-43: 18-44, 22-29, and 12-39, 8.57mm from center of weld line

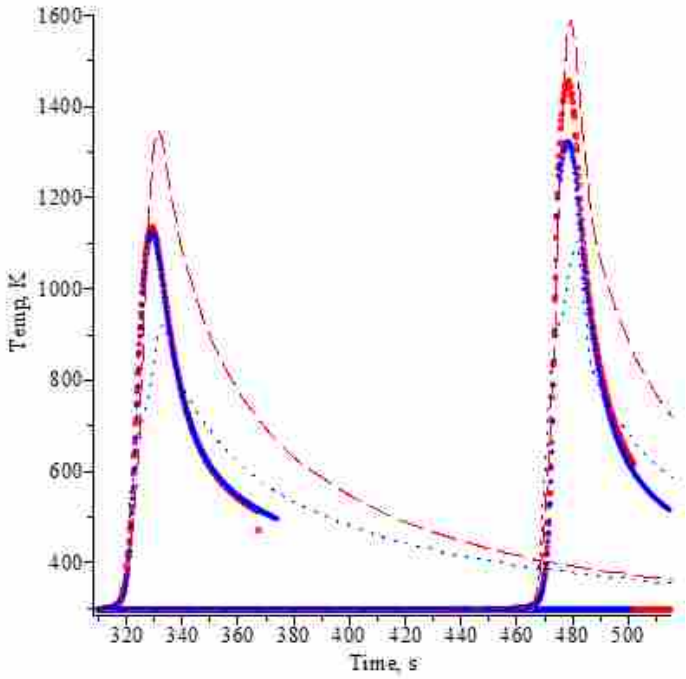

Figure 3-44: Pairs 21-28 and 25-49, 5.8mm from center of weld line

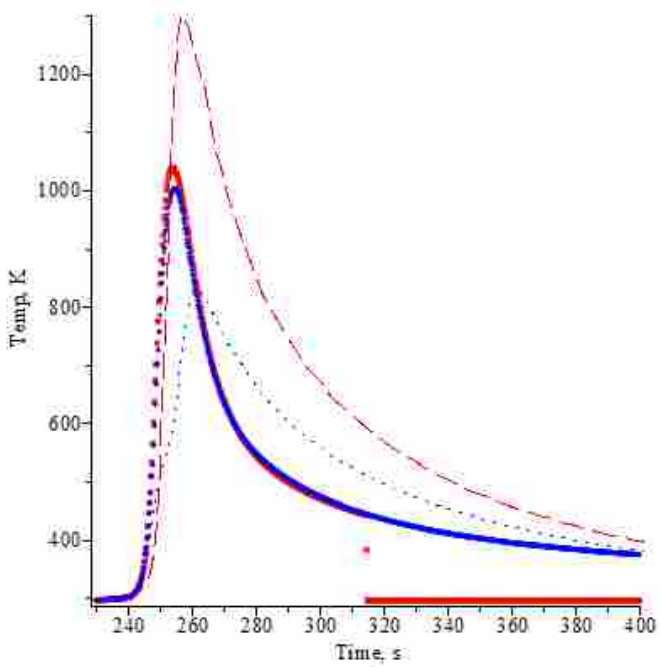

Figure 3-45: Pair 6-35, 4.54mm from center of weld line

In this weld, the differences between the advancing and retreating sides are more pronounced. The advancing side of the weld is warmer than the retreating side, as the relative velocity of the FSW tool is greater there, generally contributing to greater heat input. This results in temperature differences across the center of the weld line of at times over 100 K.

The average value for the squared sum residuals of the model as compared to the data obtained by Furse is 8.4 x 10^7 K^2, corresponding to an overall average temperature error of 200 K.

3.3 **Modeled Contours in Weld Zone**

Having compared the model to experimental data, the model was then examined along the weld line where it was not possible to obtain direct temperature readings. The model was first evaluated in a longitudinal cross-section of the workpiece, and then examined along the top surface of the workpiece.

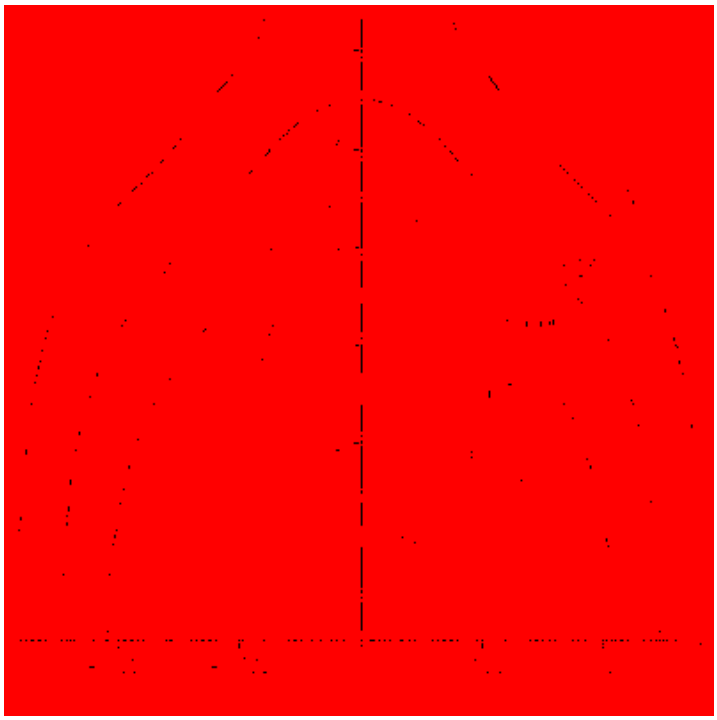

Figure 3-46: Temperature contours (K) of model corresponding to the Huang weld. Depth is measured from the surface of the workpiece (top surface is at z=0)

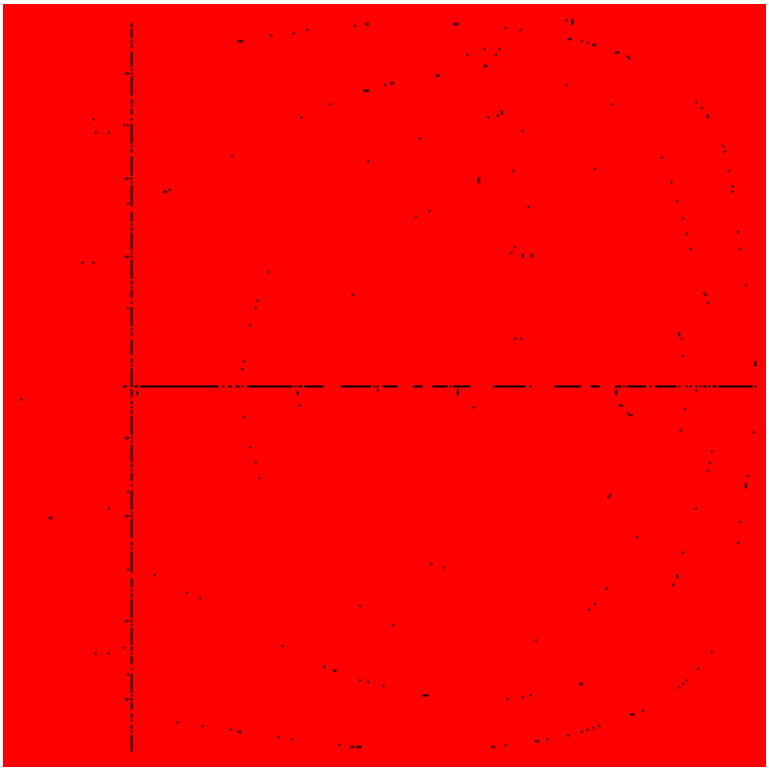

Figure 3-47: Temperature contours (K) of model on the top surface of the workpiece corresponding to Huang weld.

The contours generated from the model estimate the maximum temperature in the workpiece to be about 825 K, near the surface. Huang estimated the maximum temperature to be about 1300 K by finite element methods (Huang 2008). Additionally, the contours show steep temperature gradients just ahead of the FSW tool in the *x* direction, as well as to either side of the tool in the *y* direction (Figure 3-47).

The model predicted a much higher maximum temperature with the parameters from the Furse weld than that predicted with the Huang weld parameters. As can be seen in Figure 3-48, the maximum temperature near the surface of the workpiece is about 1250 K, as compared to 1600 K as predicted with the finite element model employed by Furse (Furse 2010). The contours also exhibit the same steep gradients in the *x* and *y* directions as seen using the Huang weld parameters.

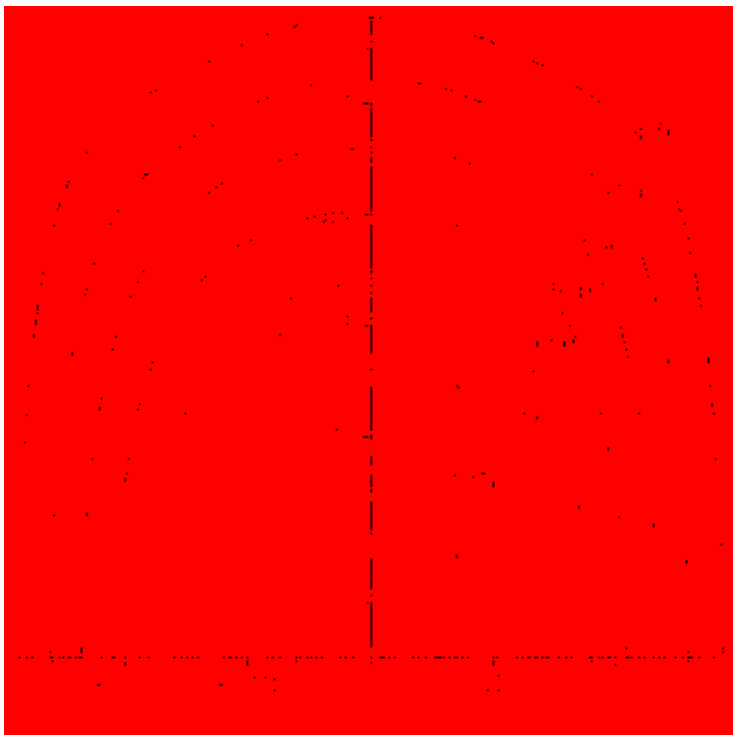

Figure 3-48: Temperature contours (K) of model corresponding to the Furse weld. Depth is measured from the surface of the workpiece (top surface is at z=0)

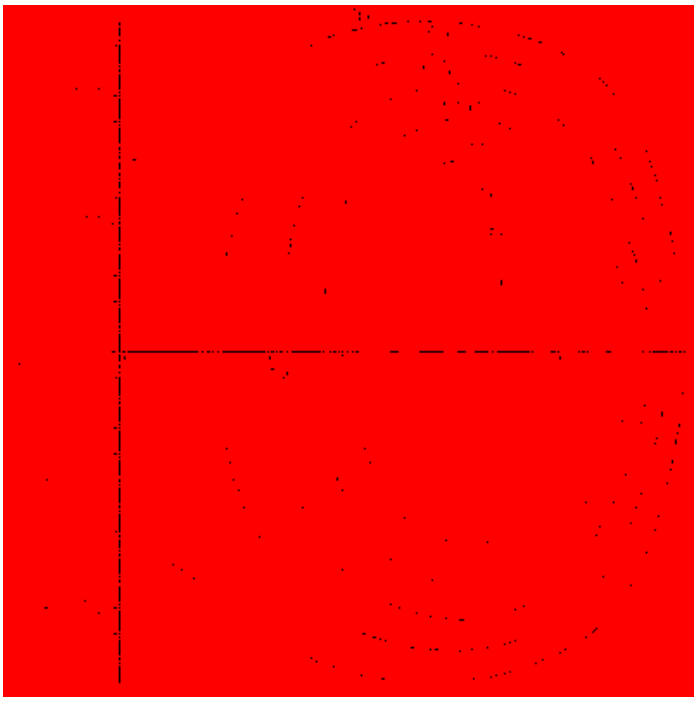

Figure 3-49: Temperature contours (K) of model on the top surface of the workpiece corresponding to Furse weld.

For additional consideration, the results obtained from the Penn State finite element model employed by Furse, as developed by (Nandan 2006) are show in Figure 3-50. The top contour plot places the bottom surface of the workpiece on the *z* axis, rather than on the top surface as in Figure 3-48. Note the higher temperatures near the surface centered around 6 mm from the center of the weld line, which are a result of the interfacial heat generation of the shoulder of the tool. Except for these regions of elevated temperature and the asymmetry between the advancing and retreating sides, the contours in the *z* direction for the Penn State model are comparable to those seen in Figure 3-48. The FSW tool is depicted as moving to the left in Figure 3-50, and the temperature gradients in the *x* direction are steeper than those seen in the analytical model in Figure 3-49.

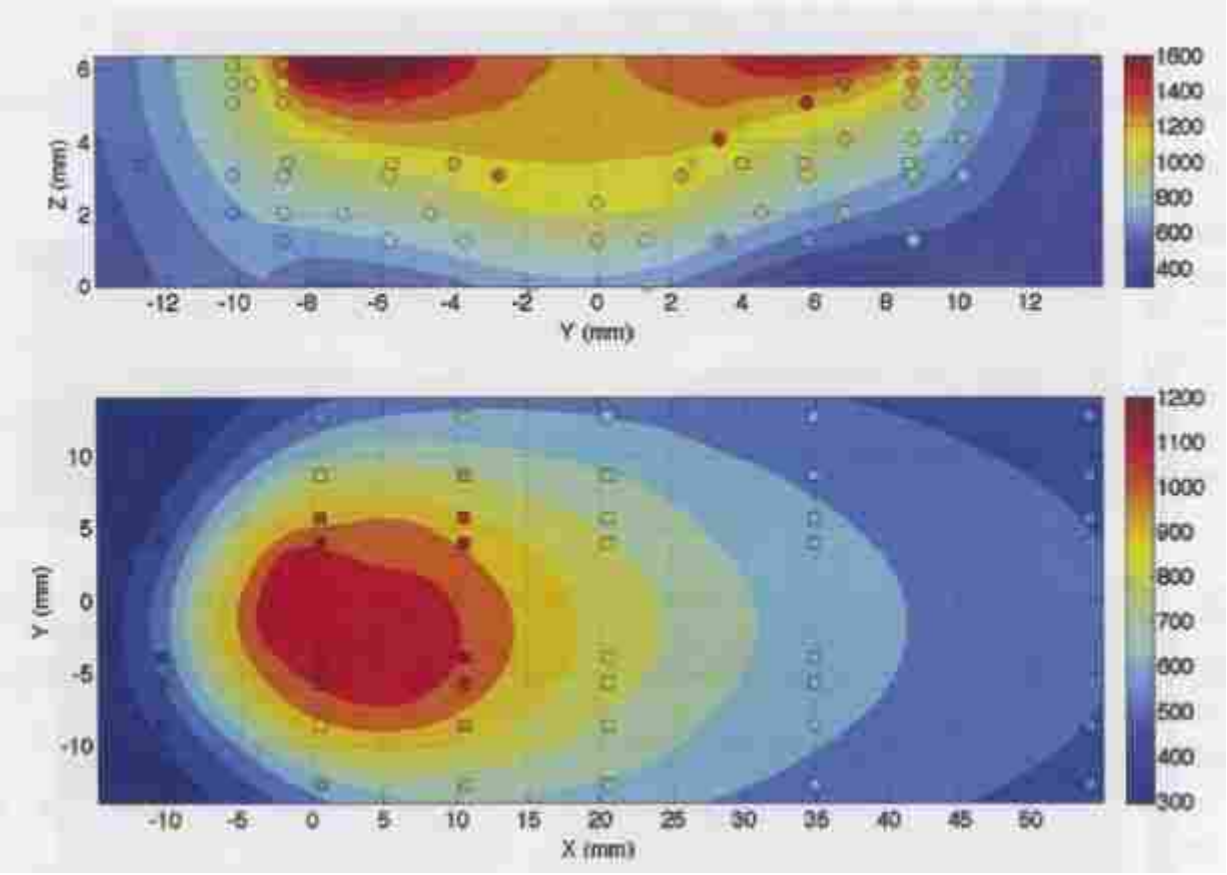

Figure 3-50: Quasi-steady temperature contours generated by the Penn State model for the Furse weld

4 CONCLUSIONS

An analytical model of a FSW process based on a distributed volumetric heat generation rate was developed, and the predicted near-field temperatures obtained using this model remained finite. Key physical parameters of the model were optimized with a limited set of experimental data, taken from different depths and distances from the center of the stir zone. The model was then compared with data taken at various locations within the workpiece in order to validate the results obtained.

The ADS model matches the Huang data better than the Furse data. The average difference between the temperature profile and the Huang data is 76 K. The maximum temperature in the workpiece during the FSW process was predicted to be 845 K, as compared to the finite element analysis estimate of 1300 K, as conducted by Huang (Huang 2008). The total heat input into the model was 889.8 W. The model's accuracy was best at locations farther from the center of the weld line, close to the midplane.

The Furse data showed significant differences from the temperature profiles generated by the analytical model, resulting in an average temperature error of 200 K. The maximum temperature in the workpiece predicted by the model was 1560 K, which compares well to the peak value obtained using the Penn State model (Nandan 2006). The total heat input into the model for this weld was 1965.6 W. Again, the model performed best at locations farther from the center of the weld line, close to the midplane.

The model exhibited two main areas of difficulty when compared to data. The peak temperature tended to be lower than measurements at locations near the top surface of the workpiece, while it tended to be higher than measurements at locations near the bottom surface of the workpiece, near the supporting plate. The cooling rate is more rapid than the measurements indicate farther from the center of the weld line, and lower than the measurements depict nearer to the center of the weld line. The locations used in optimization to obtain the physical parameters used in the model were spread throughout the workpiece (different depths and distances from the weld line). The optimization algorithm drove to reduce the overall difference between the training data and the ADS predicted temperatures, in order to give values that would be the best fit for the variety of locations observed. If only locations near the surface were used in optimization, for example, the resulting parameters would skew predicted temperatures to be much higher than what is measured deeper within the workpiece.

Previous analytical thermal models, discussed in the introduction, have been demonstrated to fairly accurately predict temperature profiles for several FSW cases. However, in studies using these models only a few sets of temperature data, taken at mid-depth within the workpiece far outside the stirred zone, were compared to the model outputs. Thus, their performance at a wider range of depths and distances from the weld line cannot be adequately compared to the model developed here. This model does perform as well as these other models in the locations examined.

The model developed in this work has demonstrated that finite temperature fields throughout the entire workpiece can be predicted with a small set of experimental data. When compared with measured data, the model maintains, on average, a peak temperature accuracy within 40-50 K. There are only a few parameters determined by regression analysis, but they

have been demonstrated to have a significant degree of influence of the temperature history of the process. It is hoped that future researchers may utilize this model for an early prediction of expected temperatures and cooling rates for friction stir welding experiments.

Despite all the work put into thermal modeling, no model can as of yet be fully validated with experimental data, as temperature measurements in the primary area of interest, the center of the weld line, are as of yet unobtainable. Finite element models incorporate the greatest amount of physical phenomena in their formulation, while analytical models must make certain assumptions to be mathematically tractable. Without data, it is not possible to definitively state if one model is more accurate than another within the weld zone.

In order to improve the model, the heat generation model will need to more accurately predict the heat input for a given FSW process. The interaction between the FSW tool and the workpiece is complex, requiring modeling of the flow of stirred material around the pin and shoulder to determine the stresses and the resulting frictional generation of heat. Without an accurate value of input heat, peak temperature cannot be very accurately predicted. Also, the heat transfer into the supporting plate will need to be more thoroughly addressed, i.e., there is increased thermal contact resistance at locations farther from the center of the weld line due to bending of the workpiece by the FSW tool. The mathematical model also required isotropic and constant values of thermal diffusivity throughout the workpiece, which does vary to some Differences in temperature between the advancing and retreating side also need to be accounted for—this would necessitate more detailed modeling of plastic flow about the FSW tool.

REFERENCES

Bonnans, J.F., Glibert, J.C., Lemarechal, C., Sagastizabal, C.A. *Numerical Optimization.* 2. Springer Berlin Heidelberg, 2006.

Carslaw, H.S. and Jaeger, J.C. *Conduction of heat in solids.* 2. Oxford: Clarendon Press, 1959.

Chao, Y.J. and Qi, X.H. "Thermal and thermo-mechanical modeling of friction stir welding of aluminum alloy 6061-T6." *Journal of Materials Processing & Manufacturing Science* 7, no. 2 (1998): 215-233.

Cho, J.H., Boyce, D.E., Dawson, P.R. "Modeling strain hardening and texture evolution in friction stir welding of stainless steel." *Materials Science and Engineering A*, no. 398 (2005): 146-163.

Ferro, P. and Bonollo, F. "A Semianalytical Thermal Model for Friction Stir Welding." *Metallurgical and Materials Transactions A* 41A (2009): 440-449.

Furse, D. ""Optimization and Correlation of the Penn State Model of Friction Stir Welding to Experimental Welds in 304L Stainless Steel"." Brigham Young University, 2010.

Gould, J.E. and Feng, Z. "Heat Flow Model for Friction Stir Welding of Aluminum Alloys." *Journal of Materials Processing & Manufacturing Science* 7 (October 1998): 185-194.

Hamilton, C., Dymeck, S., Sommers, A. "A thermal model of friction stir welding in aluminum alloys." *International Journal of Machine Tools & Manufacture* 48 (2008): 1120-1130.

Huang, D. ""Investigation of Heterogeneity of FSW Inconel 718 Coupled with Welding Thermal Cycles"." Brigham Young University, 2008.

Incropera F.P., DeWitt D.P., Bergman T.L., Lavine A.S. *Fundamentals of Heat and Mass Transfer.* 6. John Wiley & Sons, Inc., 2007.

Khandkar, M.Z.H., Khan, J.A., Reynolds, A.P. "Prediction of temperature distribution and thermal history during friction stir welding: input torque based model." *Science and Technology of Welding and Joining* 8, no. 3 (2003): 165-174.

Lienert T.J., Stellwag Jr W.L., Grimmet B.B., Warke R.W. *Welding Journal* 82, no. 1 (2003): 1s-9s.

Maalekian, M. "Thermal Modeling of Friction Welding." *ISIJ International* 48, no. 10 (2008): 1429-1433.

McClure, J.C., Tang, W., Murr, L.E., Guo, X., Feng, Z., Gould, J.E. "A Thermal Model of Friction Stir Welding." *Trends in welding research; proceedings of the 5th International Conference.* Pine Mountain, GA, 1998. 590-596.

Moraitis, G.A. and Labeas, G.N. "Investigation of friction stir welding process with emphasis on calculation of heat generated due to material stirring." *Science and Technology of Welding and Joining* 15, no. 2 (2010): 177-184.

Nandan, R., DebRoy, T., Bhadesia, H.K.D.H. "Recent advances in friction-stir welding – Process, weldment structure and properties." *Progress in Materials Science* 53 (2008): 980-1023.

Nandan, R., Roy, G.G., Lienert, T.J., DebRoy, T. "Numerical modelling of 3D plastic flow and heat transfer during friction stir welding of stainless steel." *Science and Technology of Welding and Joining* 11, no. 5 (2006): 526-537.

Nandan, R., Roy, G.G., Lienert, T.J., Debroy, T. "Three-dimensional heat and material flow during friction stir welding of mild steel." *Acta Materiala* 55 (2007): 883-895.

Owen, B. ""Two Dimensional Friction Stir Welding Model With Experimental Validation"." Brigham Young University, 2006.

Rosenthal, D. "Mathematical Theory of Heat Distribution During Welding and Cutting." *Welding Journal - Research Supplement* 20 (1941): 220-234.

Schmidt, H. and Hattel, J. "Modelling heat flow around tool probe in friction stir welding." *Science and Technology of Welding and Joining* 10, no. 2 (2005): 176-186.

Schmidt, H., Hattel, J., Wert, J. "An analytical model for the heat generation in friction." *Modelling and Simulation in Materials Science and Engineering* 12 (2004): 143-157.

Schmidt, H.B. and Hattel, J.H. "Thermal modelling of friction stir welding." *Scripta Materiala* 58 (2008): 332-337.

Soundararajan, V., Zekovic, S., Kovacevic, R. "Thermo-mechanical model with adaptive boundary conditions for friction stir welding of Al 6061." *International Journal of Machine Tools & Manufacture* 45 (2005): 1577-1587.

Thomas, W.M., Nicholas, E.D., Needham, J.C., Church, M.G., Templesmith, P., Dawes, C. Friction Welding. Great Britain Patent PCT/GB92/02203. December 6, 1991.

Uday, M.B., Ahmad Fauzi, M.N., Zuhailawati, H., and Ismail, A.B. "Advances in friction welding process: a review." *Science and Technology of Welding and Joining* 15, no. 7 (2010): 534-558.

Vilaca, P., Quintino, L., dos Santos, J.F. "iSTIR--Analytical thermal model for friction stir welding." 169 (2005): 452-465.

APPENDIX A. SOLUTION TO STURM-LIOUVILLE PROBLEM

Beginning with the dimensional form of 2-1, apply the following nondimensionalization.

$$\frac{\partial^2 T}{\partial x^2}+\frac{\partial^2 T}{\partial y^2}+\frac{\partial^2 T}{\partial z^2}+\frac{\dot{q}}{k}=\frac{1}{\alpha_t}\frac{\partial T}{\partial t} \quad \textbf{A-1}$$

$$\xi=\frac{x}{L} \quad \textbf{A-2}$$

$$\eta=\frac{y}{W} \quad \textbf{A-3}$$

$$\zeta=\frac{z}{S} \quad \textbf{A-4}$$

$$\tau=\frac{\alpha_t t}{L^2} \quad \textbf{A-5}$$

$$\xi_o=\frac{vt}{L} \quad \textbf{A-6}$$

$$\xi_s=\frac{r_s}{L} \quad \textbf{A-7}$$

$$\xi_p=\frac{r_p}{L} \quad \textbf{C-8}$$

$$\eta_s=\frac{r_s}{W} \quad \textbf{C-9}$$

$$\eta_p = \frac{r_p}{W} \quad \textbf{A-10}$$

$$\zeta_s = \frac{r_s \tan(\alpha)}{S} \quad \textbf{A-11}$$

$$\zeta_p = \frac{h_p}{S} \quad \textbf{A-12}$$

$$A = \frac{W}{L} \quad \textbf{A-13}$$

$$B = \frac{S}{L} \quad \textbf{A-14}$$

$$\theta = \frac{WSk}{Q_{tot}L}(T - T_\infty) \quad \textbf{A-15}$$

Nondimensional form of 2-1.

$$\frac{\partial^2\theta}{\partial\xi^2} + \frac{1}{A^2}\frac{\partial^2\theta}{\partial\eta^2} + \frac{1}{B^2}\frac{\partial^2\theta}{\partial\zeta^2} + \mathcal{Q} = \frac{\partial\theta}{\partial\tau} \quad \textbf{A-1}$$

Nondimensional form of 2-2.

$$\begin{aligned}\mathcal{Q} = {} & \frac{f_s}{4\zeta_s(\xi_s\eta_s - \xi_p\eta_p)}\,[(H(\xi - \xi_o + \xi_s) \\ & - H(\xi - \xi_o - \xi_s))(1 - H(\eta \\ & - \eta_s))(1 - H(\zeta - \zeta_s)) - (H(\xi \\ & - \xi_o + \xi_p) - H(\xi - \xi_o \\ & - \xi_p))(1 - H(\eta - \eta_p))(1 \\ & - H(\zeta - \zeta_s))] \\ & + \frac{f_p}{4\xi_p\eta_p\zeta_p}\,[(H(\xi - \xi_o + \xi_p) \\ & - H(\xi - \xi_o - \xi_p))(1 - H(\eta \\ & - \eta_p))(1 - H(\zeta - \zeta_p))] \\ & - \frac{f_o}{4\xi_s\,\eta_s}\,[(H(\xi - \xi_o + \xi_s) \\ & - H(\xi - \xi_o - \xi_s))(1 - H(\eta \\ & - \eta_s))\delta(\zeta - 1)]\end{aligned} \quad \textbf{A-2}$$

Divide A-1 into spatial components, representing them as X_l, Y_m, and Z_n with eigenvalues λ_l, β_m, and γ_n respectively. This results in the solution to A-1, as seen in 2-10. X_l will be solved for first.

$$\frac{d^2X_l}{d\xi^2} + \lambda_l^2 X_l = 0 \quad \textbf{A-3}$$

Solve A-3.

$$X_l = c_1 \sin(\lambda_l \xi) + c_2 \cos(\lambda_l \xi) \quad \textbf{A-4}$$

Solve for the unknown constants in A-4 by applying the nondimensionalized boundary conditions by differentiating and evaluating at the boundaries.

$$\frac{dX_l}{d\xi}|_{\xi=0} = \lambda_l c_1 \cos(0) - \lambda_l c_2 \sin(0) = \lambda_l c_1 \quad \textbf{A-5}$$

Nondimensional form of 2-3.

$$\frac{dX_l}{d\xi}|_{\xi=0} = BiX_l(0) = Bi(c_1 \sin(0) + c_2 \cos(0)) = Bic_2 \quad \textbf{A-6}$$

Set A-6 equal to A-5, solve for c_2.

$$c_2 = \frac{\lambda_l}{Bi} c_1 \quad \textbf{A-7}$$

$$\frac{dX_l}{d\xi}|_{\xi=1} = \lambda_l c_1 \cos(\lambda_l) - \frac{\lambda_l^2}{Bi} c_1 \sin(\lambda_l) \quad \textbf{A-8}$$

Nondimensional form of 2-4.

$$\frac{dX_l}{d\xi}|_{\xi=1} = -BiX_l(1) = -Bic_1 \left(\cos(\lambda_l) - \frac{\lambda_l}{Bi} \sin(\lambda_l)\right) \quad \textbf{A-9}$$

Set A-8 equal to A-9.

$$\lambda_l c_1 \cos(\lambda_l) - \frac{\lambda_l^2}{Bi} c_1 \sin(\lambda_l) = -Bic_1 \left(\cos(\lambda_l) - \frac{\lambda_l}{Bi} \sin(\lambda_l)\right) \quad \textbf{A-10}$$

Rearranging A-10 results in the eigencondition found in 2-11. The unknown constant c_1 will be solved later.

$$\tan(\lambda_p) = \frac{2\lambda_p Bi}{\lambda_p^2 - Bi^2} \quad \textbf{A-11}$$

Now solve for Y_m.

$$\frac{1}{\mathrm{A}^2}\frac{d^2Y_m}{d\eta^2} + \beta_m^2 Y_m = 0 \quad \textbf{A-12}$$

Solve A-11.

$$Y_m = c_3 \sin(A\beta_m\eta) + c_4\cos(A\beta_m\eta) \quad \textbf{A-13}$$

Differentiate and evaluate.

$$\frac{dY_m}{d\eta}|_{\eta=0} = A\beta_m c_3 \cos(0) - A\beta_m c_4 \sin(0) = A\beta_m c_3 \quad \textbf{A-14}$$

Nondimensional form of 2-5.

$$\frac{dY_m}{d\eta}|_{\eta=0} = 0 \quad \textbf{A-15}$$

Set A-15 equal to A-14, solve for c_3.

$$c_3 = 0 \quad \textbf{A-16}$$

$$\frac{dY_m}{d\eta}|_{\eta=1} = -A\beta_m c_4 \sin(A\beta_m) \quad \textbf{A-17}$$

Nondimensional form of 2-6.

$$\frac{dY_m}{d\eta}|_{\eta=1} = -BiAY_m(1) = -BiA(c_4 \cos(A\beta_m)) \quad \textbf{A-18}$$

Set A-17 equal to A-18.

$$-A\beta_m c_4 \sin(A\beta_m) = -BiA(c_4 \cos(A\beta_m)) \quad \textbf{A-19}$$

Rearranging A-19 results in the eigencondition found in 2-12. The unknown constant c_4 will be solved for later.

$$\tan(A\beta_m) = \frac{Bi}{\beta_m} \quad \textbf{A-20}$$

Now solve for Z_n.

$$\frac{1}{B^2}\frac{d^2Z_n}{d\zeta^2} + \gamma_n^2 Z_n = 0 \quad \textbf{A-21}$$

Solve A-21.

$$Z_n = c_5 \sin(B\gamma_n\zeta) + c_6 \cos(B\gamma_n\zeta) \quad \textbf{A-22}$$

Differentiate and evaluate.

$$\frac{dZ_n}{d\zeta}|_{\zeta=0} = B\gamma_n c_5 \cos(0) - B\gamma_n c_6 \sin(0) = B\gamma_n c_5 \quad \textbf{A-23}$$

Nondimensional form of 2-7.

$$\frac{dZ_n}{d\zeta}|_{\zeta=0} = BiBZ_n(0) = BiB(c_5 \sin(0) + c_6 \cos(0)) = BiBc_6 \quad \textbf{A-24}$$

Set A-23 equal to A-24, solve for c_6.

$$c_6 = \frac{\gamma_n}{Bi} c_5 \quad \textbf{A-25}$$

$$\frac{dZ_n}{d\zeta}|_{\zeta=1} = B\gamma_n c_5 \cos(B\gamma_n) - \frac{B\gamma_n^2}{Bi}\sin(B\gamma_n) \quad \textbf{A-26}$$

Nondimensional form of 2-8.

$$\frac{dZ_n}{d\zeta}|_{\zeta=1} = -BiB\mu Z_n(1) = -BiB\mu\left(c_5 \sin(B\gamma_n) + \frac{\gamma_n}{Bi} c_5 \cos(B\gamma_n)\right) \quad \textbf{A-27}$$

Set A-26 equal to A-27.

$$\gamma_n c_5 \left(\cos(B\gamma_n) - \frac{\gamma_n}{Bi}\sin(B\gamma_n)\right) = -Bi\mu c_5 \left(\sin(B\gamma_n) + \frac{\gamma_n}{Bi}\cos(B\gamma_n)\right) \quad \textbf{A-28}$$

Rearranging A-28 results in the eigencondition found in 2-13. The unknown constant c_5 will be solved for later.

$$\tan(B\gamma_n) = \frac{Bi\gamma_n(1+\mu)}{\gamma_n^2 - Bi^2\mu} \quad \textbf{A-29}$$

Substituting A-4, A-13, and A-22 into 2-10 results in the following equation.

$$\theta(\xi,\eta,\zeta,\tau) = \sum_{l=1}^{\infty}\sum_{m=1}^{\infty}\sum_{n=1}^{\infty} c_{lmn}(\tau)\left(c_1\sin(\lambda_l\xi) + \frac{\lambda_l}{Bi}c_1\cos(\lambda_l\xi)\right)(c_4\cos(A\beta_m\eta))\left(c_5\sin(B\gamma_n\zeta) + \frac{\gamma_n}{Bi}c_5\cos(B\gamma_n\zeta)\right) \quad \textbf{A-30}$$

The unknown constants can all be absorbed into c_{lmn}, resulting in the expressions for X_l, Y_m, and Z_n as seen in Equations 2-11, 2-12, and 2-13.

$$\theta(\xi,\eta,\zeta,\tau) = \sum_{l=1}^{\infty}\sum_{m=1}^{\infty}\sum_{n=1}^{\infty} c_{lmn}(\tau)\left(\sin(\lambda_l\xi) + \frac{\lambda_l}{Bi}\cos(\lambda_l\xi)\right)(\cos(A\beta_m\eta))\left(\sin(B\gamma_n\zeta) + \frac{\gamma_n}{Bi}\cos(B\gamma_n\zeta)\right) \quad \textbf{A-31}$$

It is necessary to determine whether zero eigenvalues should be included in the summations shown in A-31. To do this, Equations A-3, A-12, and A-22 are to be solved with their respective zero eigenvalues. The case for X_o will be examined first.

$$\frac{d^2X_o}{d\xi^2} = 0 \quad \textbf{A-32}$$

Solve A-32.

$$X_o = c_1\xi + c_2 \quad \textbf{A-33}$$

Differentiate and evaluate.

$$\frac{dX_o}{d\xi} = c_1 \quad \textbf{A-34}$$

$$\frac{dX_o}{d\xi}|_{\xi=0} = BiX_o(0) = Bi(c_1(0) + c_2) \quad \textbf{A-35}$$

Set A-34 equal to A-35, solve for c_1.

$$c_1 = Bic_2 \quad \textbf{A-36}$$

$$\frac{dX_o}{d\xi}|_{\xi=1} = -BiX_o(1) = -Bi(c_2(1) + c_2) \quad \textbf{A-37}$$

Set A-34 equal to A-37, rearrange.

$$Bi = -2 \quad \textbf{A-38}$$

Since the Biot number must always be positive, the zero eigenvalue should not be used when summing over *l*. The case for Y_o will be examined next.

$$\frac{1}{A}\frac{d^2Y_o}{d\eta^2} = 0 \quad \textbf{A-39}$$

Solve A-39.

$$Y_o = c_3\eta + c_4 \quad \textbf{A-40}$$

Differentiate and evaluate.

$$\frac{dY_o}{d\eta} = c_3 \quad \textbf{A-41}$$

Solve for c_3.

$$\frac{dY_o}{d\eta}|_{\eta=0} = 0 = c_3 \quad \textbf{A-42}$$

$$\frac{dY_o}{d\eta}|_{\eta=1} = -BiAY_o(1) = -BiAc_4 \quad \textbf{A-43}$$

Set A-43 equal to A-41.

$$BiAc_4 = 0 \quad \textbf{A-44}$$

Since the Biot number and *A* are nonzero values, Y_o reduces to the trivial case. Thus, the zero eigenvalue should not be used when summing over *m*. The case for Z_o will be examined next.

$$\frac{1}{B}\frac{d^2Z_o}{d\zeta^2} = 0 \quad \textbf{A-45}$$

Solve A-45.

$$Z_o = c_5\zeta + c_6 \quad \textbf{A-46}$$

Differentiate and evaluate.

$$\frac{dZ_o}{d\zeta} = c_5 \quad \textbf{A-47}$$

$$\frac{dZ_o}{d\zeta}|_{\zeta=0} = BiBZ_o(0) = BiB(c_5(0) + c_6) \quad \textbf{A-48}$$

Set A-47 equal to A-48, solve for c_5.

$$c_5 = BiBc_6 \quad \textbf{A-49}$$

$$\frac{dZ_o}{d\zeta}|_{\zeta=1} = -BiB\mu Z_o(1) = -BiB\mu(c_5(1) + c_6) \quad \textbf{A-50}$$

Set A-50 equal to A-47, rearrange.

$$Bi = -\frac{\mu + 1}{B\mu} \quad \textbf{A-51}$$

Since the Biot number, B, and μ are positive, the zero eigenvalue should not be used when summing over n.

The expression for the nondimensional temperature in Equation A-31 can be substituted into Equation A-1, the nondimensional governing equation. The terms found in Equation A-31 are replaced with X_l, Y_m, and Z_n. The summation describing the heat source, is also included in the following equation.

$$\sum_{l=1}^{\infty}\sum_{m=1}^{\infty}\sum_{n=1}^{\infty} c_{lmn}\left(\frac{d^2X_l}{d\xi^2}Y_mZ_n + \frac{1}{A^2}X_l\frac{d^2Y_m}{d\eta^2}Z_n + \frac{1}{B^2}X_lY_m\frac{d^2Z_n}{d\zeta^2}\right) + b_{lmn}X_lY_mZ_n = \frac{dc_{lmn}}{d\tau}X_lY_mZ_n \quad \textbf{A-52}$$

Substituting from Equations A-3, A-12, and A-22, the derivatives can be substituted as follows.

$$\sum_{l=1}^{\infty}\sum_{m=1}^{\infty}\sum_{n=1}^{\infty} c_{lmn}\left(-\lambda_l^2X_lY_mZ_n - \frac{1}{A^2}X_l\beta_m^2A^2Y_mZ_n - \frac{1}{B^2}X_lY_m\gamma_n^2B^2Z_n\right) + b_{lmn}X_lY_mZ_n = \frac{dc_{lmn}}{d\tau}X_lY_mZ_n \quad \textbf{A-53}$$

Simplifying and rearranging A-53.

$$\sum_{l=1}^{\infty}\sum_{m=1}^{\infty}\sum_{n=1}^{\infty}\left[-\frac{dc_{lmn}}{d\tau} - (\lambda_l^2 + \beta_m^2 + \gamma_n^2)c_{lmn} + b_{lmn}\right]X_lY_mZ_n = 0 \quad \textbf{A-54}$$

According to theory for Sturm-Liouville problems, X_l, Y_m, and Z_n form an orthogonal set, with the following properties.

$$\int_0^1 X_lX_p\,d\xi = \begin{cases} 0 \; if \; l \neq p \\ N_p \; if \; l = p \end{cases} \quad \textbf{A-55}$$

$$\int_0^1 Y_mY_q\,d\eta = \begin{cases} 0 \; if \; m \neq q \\ N_q \; if \; m = q \end{cases} \quad \textbf{A-56}$$

$$\int_0^1 Z_nZ_r\,d\zeta = \begin{cases} 0 \; if \; n \neq r \\ N_r \; if \; n = r \end{cases} \quad \textbf{A-57}$$

Equation A-54 can then be multiplied by $\int_0^1 X_p\,d\xi \int_0^1 Y_q\,d\eta \int_0^1 Z_r\,d\zeta$, resulting in the following equation after simplification (for the nontrivial case).

$$\sum_{l=1}^{\infty}\sum_{m=1}^{\infty}\sum_{n=1}^{\infty}\left[-\frac{dc_{lmn}}{d\tau}-(\lambda_l^2+\beta_m^2+\gamma_n^2)c_{lmn}+b_{pqr}\right]N_pN_qN_r=0 \quad \textbf{A-58}$$

Simplify further.

$$\left[\frac{dc_{pqr}}{d\tau}+\left(\lambda_p^2+\beta_q^2+\gamma_r^2\right)c_{pqr}-b_{pqr}\right]=0 \quad \textbf{A-59}$$

It is necessary to determine b_{pqr} before the solution can be evaluated. Recall that it describes the heat source. Multiplying by $\int_0^1 X_p d\xi \int_0^1 Y_q d\eta \int_0^1 Z_r d\zeta$ and simplifying results in the following equation.

$$b_{pqr}=\frac{1}{N_pN_qN_r}\int_0^1\int_0^1\int_0^1 \mathcal{Q}(X_pY_qZ_r)d\xi d\eta d\zeta \quad \textbf{A-60}$$

Equation A-2 is the nondimensionalized expression for the moving heat source in the model, and it is a function of ξ, η, ζ, and τ. The required integration is extensive, so it will be divided into three smaller portions, representing the different parts of the heat source. The sum of all these portions yields the entire moving heat source.

The first portion examined is f_s, the outer portion of the heat source, representing the shoulder of the tool. The Heaviside step functions, when integrated, alter the limits of integration to the interval where there are nonzero.

$$b_{pqr_{fs}}=\frac{f_s}{\left(4\zeta_s(\xi_s\eta_s-\xi_p\eta_p)\right)N_pN_qN_r}\left(\int_{\xi_o-\xi_s}^{\xi_o+\xi_s}\int_0^{\eta_s}\int_0^{\zeta_s}X_pY_qZ_rd\xi d\eta d\zeta-\int_{\xi_o-\xi_p}^{\xi_o+\xi_p}\int_0^{\eta_p}\int_0^{\zeta_s}X_pY_qZ_rd\xi d\eta d\zeta\right) \quad \textbf{A-61}$$

$$b_{pqr_{f_s}} = \frac{2f_s}{\left(\zeta_s\left(\xi_s\eta_s - \xi_p\eta_p\right)\right)N_pN_qN_rAB\lambda_p\beta_q\gamma_r}$$

Integrate.

$$\left[-\sin\left(\beta_qA\eta_s\right)\sin\left(\lambda_p\xi_s\right)\left(\sin\left(\lambda_p\xi_o\right) + \frac{\lambda_p\cos\left(\lambda_p\xi_o\right)}{Bi}\right)\left(\cos\left(\gamma_rB\zeta_s\right) - 1 - \frac{\gamma_r}{Bi}\sin\left(\gamma_rB\zeta_s\right)\right) + 2\sin\left(\beta_qA\eta_p\right)\sin\left(\lambda_p\xi_p\right)\left(\sin\left(\lambda_p\xi_o\right) + \frac{\lambda_p\cos\left(\lambda_p\xi_o\right)}{Bi}\right)\left(\cos\left(\gamma_rB\xi_s\zeta_s\right) - 1 - \frac{\gamma_r}{Bi}\sin\left(\gamma_rB\xi_s\zeta_s\right)\right)\right] \quad \textbf{A-62}$$

The next portion examined is f_p, which represents the FSW tool probe, the inner portion of the moving heat source. Like with the previous portion, the Heaviside step functions change the limits of integration.

$$b_{pqr_{fp}} = \frac{f_p}{\left(\xi_p\eta_p\zeta_p\right)N_pN_qN_r}\int_{\xi_o-\xi_p}^{\xi_o+\xi_p}\int_0^{\eta_p}\int_0^{\zeta_p}X_pY_qZ_rd\xi d\eta d\zeta \quad \textbf{A-63}$$

Integrate.

$$b_{pqr_{fp}} = \frac{2f_p}{\left(\xi_p\eta_p\zeta_p\right)N_pN_qN_rAB\lambda_p\beta_q\gamma_r}\left[\sin\left(\beta_qA\eta_p\right)\sin\left(\lambda_p\xi_p\right)\left(\sin\left(\lambda_p\xi_o\right) + \frac{\lambda_p\cos\left(\lambda_p\xi_o\right)}{Bi}\right)\left(\cos\left(\gamma_rB\zeta_p\right) - 1 - \frac{\gamma_r}{Bi}\sin\left(\gamma_rB\zeta_p\right)\right)\right] \quad \textbf{A-64}$$

The last portion examined is f_o, which represents the region of reduced thermal contact resistance beneath the moving heat source. Like with the previous portions, the Heaviside step functions change the limits of integration. The Dirac delta function results in the evaluation of its dependent functions at the location of its impulse when integrated.

$$b_{pqr_{qo}} = \frac{-f_o}{\left(\xi_s\eta_s\right)N_pN_qN_r}\int_{\xi_o-\xi_s}^{\xi_o+\xi_s}\int_0^{\eta_s}X_pY_qZ_r(1)d\xi d\eta \quad \textbf{A-65}$$

Integrate.

$$b_{pqr_{fo}} = \frac{-f_o}{(2\xi_s\eta_s)N_pN_qN_rAB\lambda_p\beta_q}\left[\sin\left(\beta_q A\eta_s\right)\sin\left(\lambda_p\xi_s\right)\left(\sin\left(\lambda_p\xi_o\right) + \frac{\lambda_p\cos\left(\lambda_p\xi_o\right)}{Bi}\right)\left(\sin\left(\gamma_r B\right) + \frac{\gamma_r}{Bi}\cos\left(\gamma_r B\right)\right)\right] \quad \textbf{A-66}$$

Note that b_{pqr} contains ξ_o, which is a function of τ. It is necessary to separate out all the terms that contain it. The portion not containing ξ_o is lumped into the following parameter.

$$D = \frac{1}{N_pN_qN_rAB\lambda_p\beta_q}\left\{\left[\frac{f_s}{\left(\zeta_s(\xi_s\eta_s-\xi_p\eta_p)\right)\gamma_r}\left(-sin\left(\beta_q A\eta_s\right)sin\left(\lambda_p\xi_s\right)\left(cos(\gamma_r B\zeta_s) - 1 - \frac{\gamma_r}{Bi}sin(\gamma_r B\zeta_s)\right) + 2sin\left(\beta_q A\eta_p\right)sin\left(\lambda_p\xi_p\right)\left(cos(\gamma_r B\xi_s\zeta_s) - 1 - \frac{\gamma_r}{Bi}sin(\gamma_r B\xi_s\zeta_s)\right)\right)\right] + \frac{2f_p}{(\xi_p\eta_p\zeta_p)\gamma_r}\left[sin\left(\beta_q A\eta_p\right)sin\left(\lambda_p\xi_p\right)\left(cos\left(\gamma_r B\zeta_p\right) - 1 - \frac{\gamma_r}{Bi}sin\left(\gamma_r B\zeta_p\right)\right)\right] - \frac{f_o}{(2\xi_s\eta_s)}\left[sin\left(\beta_q A\eta_s\right)sin\left(\lambda_p\xi_s\right)\left(sin(\gamma_r B) + \frac{\gamma_r}{Bi}cos(\gamma_r B)\right)\right]\right\} \quad \textbf{A-67}$$

The remainder can simply be described as $X_p(\xi_o)$, thus b_{pqr} can then be defined as the following equation.

$$b_{pqr} = DX_p(\xi_o) \quad \textbf{A-68}$$

Now it is possible to solve for c_{pqr}, as described in Equation A-59, with b_{pqr} known. Because b_{pqr} is a function of τ, the differential equation will need to be solved with an integrating factor.

$$E = \lambda_p^2 + \beta_q^2 + \gamma_r^2 \quad \textbf{A-69}$$

Substitute A-69 into A-59.

$$e^{(E)\tau}c_{pqr} = \int_0^\tau DX_p(\xi_o)\, e^{(E)\tau}d\tau \quad \textbf{A-70}$$

Rearrange and expand.

$$\frac{c_{pqr}}{D}e^{E\tau} = \int_0^{\tau}\left[\sin\left(\frac{\lambda_p v L\tau}{\alpha}\right) + \frac{\lambda_p}{Bi}\cos\left(\frac{\lambda_p v L\tau}{\alpha}\right)\right]e^{E\tau}d\tau \quad \textbf{A-71}$$

$$F = \left(\frac{\lambda_p v L\tau}{\alpha}\right) \quad \textbf{A-72}$$

Substitute A-72 into A-71.

$$\frac{c_{pqr}}{D}e^{E\tau} = \int_0^{\tau}\left[\sin(F\tau) + \frac{\lambda_p}{Bi}\cos(F\tau)\right]e^{E\tau}d\tau \quad \textbf{A-73}$$

Integrate.

$$\frac{c_{pqr}}{D}e^{E\tau} = \frac{(F - Fe^{E\tau}\cos(F\tau) + Ee^{E\tau}\sin(F\tau))}{E^2+F^2} + \frac{\lambda_p}{Bi}\frac{(-E + Fe^{E\tau}\cos(F\tau) + Fe^{E\tau}\sin(F\tau))}{E^2+F^2} \quad \textbf{A-74}$$

After simplifying and expanding Equation A-74, c_{pqr} becomes as Equation 2-14 shows.

$$c_{pqr} = \frac{\left[Bi(\lambda_p^2+\beta_q^2+\gamma_r^2)+\frac{\lambda_p^2 vL}{\alpha}\right]\sin(\lambda_p\xi_o)+\left[\lambda_p(\lambda_p^2+\beta_q^2+\gamma_r^2)-\frac{Bi\lambda_p vL}{\alpha}\right]\cos(\lambda_p\xi_o)}{2N_pN_qN_rA\lambda_p\beta_qBi\left[\left(\lambda_p^2+\beta_q^2+\gamma_r^2\right)^2+\frac{\lambda_p^2v^2L^2}{\alpha^2}\right]}\left\{\left[\frac{f_s}{(\zeta_s(\xi_s\eta_s-\xi_p\eta_p))B\gamma_r}\left(\left(sin(\beta_qA\eta_p)\,sin(\lambda_p\xi_p) - sin(\beta_qA\eta_s)\,sin(\lambda_p\xi_s)\right)\left(cos(\gamma_rB\zeta_s) - 1 - \frac{\gamma_r}{Bi}sin(\gamma_rB\zeta_s)\right)\right)\right] - \frac{f_p}{(\xi_p\eta_p\zeta_p)B\gamma_r}\left[sin(\beta_qA\eta_p)\,sin(\lambda_p\xi_p)\left(cos(\gamma_rB\zeta_p) - 1 - \frac{\gamma_r}{Bi}sin(\gamma_rB\zeta_p)\right)\right] - \frac{f_o}{(\xi_s\eta_s)}\left[sin(\beta_qA\eta_s)\,sin(\lambda_p\xi_s)\left(sin(\gamma_rB) + \frac{\gamma_r}{Bi}cos(\gamma_rB)\right)\right]\right\} \quad \textbf{A-75}$$

By substituting 2-14 into 2-10, the nondimensional temperature θ can be found at any nondimensional location and time. The temperature can be obtained by using the relations in Section 2.1.6.

APPENDIX B. HUANG THERMOCOUPLE PLACEMENT

The following table shows the locations of the 53 thermocouples used in validation and comparison with the analytical model. The x origin is relative to the lengthwise edge of the workpiece, from where the FSW tool began to advance. The y origin is on the weld line, with negative y positions being on the advancing side of the weld line. The z origin is relative to the top of the workpiece plate, positive with increasing depth into the plate.

Table B-1: Location data for Huang Thermocouples

Hole No.	*Channel-Switch*	*X (cm)*	*Y (cm)*	*Z (cm)*	*Hole No.*	*Channel-Switch*	*X (cm)*	*Y (cm)*	*Z (cm)*
1	1-1	8.79	0.875	0.340	28	8-3	69.75	-0.875	0.120
2	1-2	31.65	0.685	0.290	29	8-4	87.53	-0.965	0.010
3	1-3	51.97	1.015	0.180	30	9-1	8.79	-0.875	0.340
4	1-4	74.83	1.015	0.060	31	9-2	31.65	-0.710	0.290
5	2-1	11.33	0.580	0.340	32	9-3	51.97	-1.015	0.180
6	2-2	34.19	0.452	0.290	33	9-4	74.83	-1.015	0.060
7	2-3	57.05	0.875	0.180	34	10-1	11.33	-0.580	0.340
8	2-4	77.37	0.965	0.060	35	10-2	34.19	-0.465	0.290
9	3-1	13.87	0.335	0.340	36	10-3	57.05	-0.875	0.180
10	3-2	36.73	0.132	0.290	37	10-4	77.37	-0.965	0.060
11	3-4	79.91	0.875	0.060	38	11-1	13.87	-0.370	0.340
12	4-1	16.41	0.130	0.340	39	11-2	36.73	-0.185	0.290
13	4-2	39.27	1.015	0.240	40	11-3	59.59	-0.710	0.180
14	4-3	62.13	0.335	0.180	41	11-4	79.91	-0.875	0.060
15	4-4	82.45	0.685	0.060	42	12-1	16.41	-0.190	0.340
16	5-1	18.95	0.000	0.295	43	12-2	39.27	-1.015	0.240
17	5-2	44.35	0.875	0.240	44	12-3	62.13	-0.370	0.180
18	5-3	64.67	1.015	0.120	45	12-4	82.45	-0.710	0.060
19	5-4	84.99	1.015	0.010	46	13-1	24.03	-1.015	0.290
20	6-1	24.03	1.015	0.290	47	13-2	44.35	-0.875	0.240
21	6-2	46.89	0.580	0.240	48	13-3	64.67	-1.015	0.120
22	6-3	69.75	0.875	0.120	49	13-4	84.99	-1.015	0.010
23	6-4	87.53	0.965	0.010	50	15-1	29.11	-0.875	0.290
24	7-1	29.11	0.875	0.290	51	15-2	49.43	-0.275	0.240
25	7-2	49.43	0.232	0.240	52	15-3	72.29	-0.580	0.120
26	7-3	72.29	0.580	0.120	53	15-4	90.07	-0.875	0.010
27	8-1	6.25	0.000	0.340					

APPENDIX C. FURSE THERMOCOUPLE PLACEMENT

The following table shows the locations of the 50 thermocouples used in validation and comparison with the analytical model. The x origin is relative to the lengthwise edge of the workpiece, from where the FSW tool began to advance. The y origin is on the weld line, with negative y positions being on the advancing side of the weld line. The z origin is relative to the top of the workpiece plate, positive with increasing depth into the plate.

Table C-1: Location data for Furse Thermocouples

Hole No.	*Channel-Switch*	*X (cm)*	*Y (cm)*	*Z (cm)*	*Hole No.*	*Channel-Switch*	*X (cm)*	*Y (cm)*	*Z (cm)*
1	1-1	17.64	0.857	0.508	26	7-4	98.28	0.857	0.025
2	1-2	40.32	0.680	0.432	27	8-1	15.12	0	0.508
3	1-3	60.48	1.008	0.229	28	8-2	55.44	-0.580	0.330
4	1-4	83.16	1.008	0.076	29	8-3	78.12	-0.857	0.127
5	2-1	20.16	0.580	0.508	30	8-4	95.76	-0.958	0.025
6	2-2	42.84	0.454	0.432	31	9-1	17.64	-0.857	0.508
7	2-3	65.52	0.857	0.229	32	9-2	40.32	-0.706	0.432
8	2-4	85.68	0.958	0.076	33	9-4	83.16	-1.008	0.076
9	3-1	22.68	0.328	0.508	34	10-1	20.16	-0.580	0.508
10	3-2	45.36	0.126	0.635	35	10-2	42.84	-0.454	0.432
11	3-3	68.04	0.680	0.229	36	10-4	85.68	-0.958	0.076
12	3-4	88.20	0.857	0.076	37	11-1	22.68	-0.378	0.508
13	4-1	25.20	0.126	0.508	38	11-0	45.36	-0.176	0.432
14	4-2	47.88	1.008	0.330	39	11-4	88.20	-0.857	0.076
15	4-3	70.56	0.328	0.229	40	12-1	25.20	-0.202	0.635
16	4-4	90.72	0.680	0.076	41	12-2	47.88	-1.008	0.330
17	5-1	27.72	0	0.406	42	12-4	90.72	-0.706	0.076
18	5-2	52.92	0.857	0.330	43	13-1	32.76	-1.008	0.432
19	5-3	73.08	1.008	0.127	44	13-2	52.92	-0.857	0.330
20	5-4	93.24	1.008	0.025	45	13-3	73.08	-1.008	0.127
21	6-2	55.44	0.580	0.330	46	13-4	93.24	-1.008	0.025
22	6-3	78.12	0.857	0.127	47	15-1	37.80	-0.857	0.432
23	6-4	95.76	0.958	0.025	48	15-2	57.96	-0.277	0.330
24	7-2	57.96	0.227	0.330	49	15-3	80.64	-0.580	0.127
25	7-3	80.64	0.580	0.127	50	15-4	98.28	-0.857	0.025

APPENDIX D. MAPLE PROCEDURE FOR EVALUATING FURSE TEMPERATURE

```
> restart;
> with(plots);
> L := 1.2192;
> W := .2032;
> S := 0.635e-2;
> rprobe := 0.254e-1*(.5*.284);
> hprobe := .19*0.254e-1;
> rshoulder := 0.254e-1*(.5*.93);
> NULL;
> k := 22.6;
> cp := 557;
> rho := 7900;
> alpha := k/(cp*rho);
> m^2*per*s;
> sigma := 0.16e9;
> `&tau;y` := evalf(sigma/sqrt(3));
>
> FTHERM := 0.333e5;
> omega := evalf((1/60)*(400*2)*Pi);
> ang := (10*(1/360))*Pi;
> Qslide := evalf(((2/3)*FTHERM/rshoulder^2*.25)*omega*((rshoulder^3-
rprobe^3)*evalf(1+tan(-ang))+rprobe^3+3*rprobe^2*hprobe));
                          2826.289097
> Qstick := evalf((2/3)*`&tau;y`*omega*((rshoulder^3-rprobe^3)*evalf(1+tan(-
ang))+rprobe^3+3*rprobe^2*hprobe));
                          4374.868821
> h := 10;
> U := 210.5;
                             210.5
> fractionp := .695478;
> Qin := fractionp*Qslide;
>
> fs := .884693;
> fp := .115306;

> fo := .715615;
> Tinf := 295;
> v := 0.1693e-2;
> m*per*s;

> tau := alpha*t/L^2;

> Bi := h*L/k;
> mu := U/h;
> `&xi;not` := v*t/L;
> A := W/L;
> B := S/L;
> `&xi;s` := rshoulder/L;
```

```
> `&eta;s` := rshoulder/W;
> `&xi;p` := rprobe/L;
> `&eta;p` := rprobe/W;


> `&zeta;s` := hprobe/S;
> `&zeta;p` := evalf(rshoulder*tan(ang))/S;
> tend := L/v;

#Sturm-Liouville Problem
%;


> lambdafinder := (lambda^2-Bi^2)*tan(lambda)-2.0*lambda*Bi;
plot(lambdafinder, lambda = 0 .. 10, y = -20 .. 20);
%;
   /      2                \
   \lambda  - 0.2910268306/ tan(lambda) - 1.078938053 lambda
> n := 1;
> for m to 210 do a := fsolve(lambdafinder = 0, lambda = (m-.9999999)*2.5 ..
2.5*m); if type(a, float) then lambda[n] := a; n := n+1 end if end do; for i
to 4 do lambda[i] end do;
                          0.9942614112
                          3.451668608
                          6.450072235
                          9.537780113
> P := n-1;
                              168
> NULL;
>
                              NULL
>
>
> betafinder := beta*tan(A*beta)-Bi; plot(betafinder, beta = -5 .. 100, y = -
80 .. 80);
%;
           beta tan(0.1666666667 beta) - 0.5394690265

> n := 1;


for m to 160 do b := fsolve(betafinder = 0, beta = (m-1)*10 .. 10*m); if
type(b, float) then beta[n] := b; n := n+1 end if end do; for i to 4 do
beta[i] end do;
                          1.772594584
                          19.01969256
                          37.78477053
                          56.60584764
> Q := n-1;
                               85
>
>
> NULL;

> gammafinder := (g^2-Bi^2*mu)*tan(B*g)-Bi*g*(mu+1.0); plot(gammafinder, g =
-100 .. 1000, y = -50000 .. 50000);
%;
```

```
    / 2              \
    \g  - 6.126114784/ tan(0.005208333333 g) - 11.89529203 g
>
> n := 1;


for m to 90 do c := fsolve(gammafinder = 0, g = (m-.99999)*200 .. 200*m); if
type(c, float) then g[n] := c; n := n+1 end if end do; for i to 4 do g[i] end
do;
                          47.36561339
                          606.9482875
                          1208.261759
                          1810.818603
> R := n-1;
                               30
                             n := 1


> for i to P do NX[i] := (Bi^2+lambda[i]^2+2*Bi)/(2*Bi^2) end do; for i to 4
do NX[i] end do;
                          4.052067351
                          22.82260545
                          73.83064410
                          158.6438168
 (??); #

> for i to P do X[i] := sin(lambda[i]*xi)+lambda[i]*cos(lambda[i]*xi)/Bi end
do; for i to 4 do X[i] end do;
    sin(0.9942614112 xi) + 1.843037065 cos(0.9942614112 xi)
     sin(3.451668608 xi) + 6.398270222 cos(3.451668608 xi)
     sin(6.450072235 xi) + 11.95633469 cos(6.450072235 xi)
     sin(9.537780113 xi) + 17.67994017 cos(9.537780113 xi)
> for i to Q do NY[i] := (A*Bi^2+A*beta[i]^2+Bi)/(2*A*(beta[i]^2+Bi^2)) end
do; for i to 4 do NY[i] end do;
                          0.9714102155
                          0.5044702470
                          0.5011333540
                          0.5005050400
> for i to Q do Y[i] := cos(A*beta[i]*eta) end do; for i to 4 do Y[i] end do;
%;
                     cos(0.2954324307 eta)
                      cos(3.169948761 eta)
                      cos(6.297461756 eta)
                      cos(9.434307942 eta)
> for i to R do NZ[i] := 1/2+g[i]^2/(2*Bi^2)+(g[i]/(2*B*Bi^2)-
1/(2*B*g[i]))*sin(B*g[i])*cos(B*g[i])+sin(B*g[i])^2/(B*Bi) end do; for i to 4
do NZ[i] end do;
                          7575.667186
                                                5
                        6.368307154 10
                                                6
                        2.512105962 10
                                                6
                        5.637535390 10
> for i to R do Z[i] := sin(B*g[i]*zetta)+g[i]*cos(B*g[i]*zetta)/Bi end do;
for i to 4 do Z[i] end do;
sin(0.2466959031 zetta) + 87.80043165 cos(0.2466959031 zetta)
```

```
  sin(3.161188997 zetta) + 1125.084588 cos(3.161188997 zetta)
  sin(6.293029994 zetta) + 2239.724061 cos(6.293029994 zetta)
  sin(9.431346890 zetta) + 3356.668342 cos(9.431346890 zetta)

> p := 'p'; q := 'q'; r := 'r';

NULL;
>
> for p to P do for q to Q do for r to R do c[p, q, r] :=
((Bi*(lambda[p]^2+beta[q]^2+g[r]^2)+lambda[p]^2*v*L/alpha)*sin(lambda[p]*`&xi
;not`)+(lambda[p]*(lambda[p]^2+beta[q]^2+g[r]^2)-
Bi*lambda[p]*v*L/alpha)*cos(lambda[p]*`&xi;not`))/(NX[p]*NY[q]*NZ[r]*Bi*((lam
bda[p]^2+beta[q]^2+g[r]^2)^2+lambda[p]^2*v^2*L^2/alpha^2))*(-
(1/2)*(Bi*fo*sin(A*beta[q]*`&eta;s`)*sin(B*g[r])*sin(lambda[p]*`&xi;s`)*`&zet
a;s`*B*g[r]*`&zeta;p`*`&xi;p`^2*`&eta;p`^2+Bi*fp*sin(A*beta[q]*`&eta;p`)*cos(
`&zeta;p`*B*g[r])*sin(lambda[p]*`&xi;p`)*`&zeta;s`*`&xi;s`*`&eta;s`*`&xi;p`*`
&eta;p`-
Bi*fo*sin(A*beta[q]*`&eta;s`)*sin(B*g[r])*sin(lambda[p]*`&xi;s`)*`&zeta;s`*B*
g[r]*`&zeta;p`*`&xi;p`*`&eta;p`*`&xi;s`*`&eta;s`-
Bi*fp*sin(A*beta[q]*`&eta;p`)*sin(lambda[p]*`&xi;p`)*`&zeta;s`*`&xi;s`*`&eta;
s`*`&xi;p`*`&eta;p`-
Bi*fp*sin(A*beta[q]*`&eta;p`)*cos(`&zeta;p`*B*g[r])*sin(lambda[p]*`&xi;p`)*`&
zeta;s`*`&xi;s`^2*`&eta;s`^2+Bi*fs*sin(A*beta[q]*`&eta;p`)*cos(B*g[r]*`&zeta;
s`)*sin(lambda[p]*`&xi;p`)*`&zeta;p`*`&xi;p`*`&eta;p`*`&xi;s`*`&eta;s`+Bi*fs*
sin(A*beta[q]*`&eta;s`)*sin(lambda[p]*`&xi;s`)*`&zeta;p`*`&xi;p`*`&eta;p`*`&x
i;s`*`&eta;s`-
Bi*fs*sin(A*beta[q]*`&eta;s`)*cos(B*g[r]*`&zeta;s`)*sin(lambda[p]*`&xi;s`)*`&
zeta;p`*`&xi;p`*`&eta;p`*`&xi;s`*`&eta;s`+Bi*fp*sin(A*beta[q]*`&eta;p`)*sin(l
ambda[p]*`&xi;p`)*`&zeta;s`*`&xi;s`^2*`&eta;s`^2-
Bi*fs*sin(A*beta[q]*`&eta;p`)*sin(lambda[p]*`&xi;p`)*`&zeta;p`*`&xi;p`*`&eta;
p`*`&xi;s`*`&eta;s`+fp*sin(A*beta[q]*`&eta;p`)*sin(`&zeta;p`*B*g[r])*sin(lamb
da[p]*`&xi;p`)*`&zeta;s`*g[r]*`&xi;s`^2*`&eta;s`^2+fo*sin(A*beta[q]*`&eta;s`)
*g[r]^2*cos(B*g[r])*sin(lambda[p]*`&xi;s`)*`&zeta;s`*B*`&zeta;p`*`&xi;p`^2*`&
eta;p`^2+fs*sin(A*beta[q]*`&eta;s`)*sin(B*g[r]*`&zeta;s`)*sin(lambda[p]*`&xi;
s`)*g[r]*`&zeta;p`*`&xi;p`*`&eta;p`*`&xi;s`*`&eta;s`-
fp*sin(A*beta[q]*`&eta;p`)*sin(`&zeta;p`*B*g[r])*sin(lambda[p]*`&xi;p`)*`&zet
a;s`*g[r]*`&xi;s`*`&eta;s`*`&xi;p`*`&eta;p`-
fo*sin(A*beta[q]*`&eta;s`)*g[r]^2*cos(B*g[r])*sin(lambda[p]*`&xi;s`)*`&zeta;s
`*B*`&zeta;p`*`&xi;p`*`&eta;p`*`&xi;s`*`&eta;s`-
fs*sin(A*beta[q]*`&eta;p`)*sin(B*g[r]*`&zeta;s`)*sin(lambda[p]*`&xi;p`)*g[r]*
`&zeta;p`*`&xi;p`*`&eta;p`*`&xi;s`*`&eta;s`)/(`&zeta;s`*(-
`&xi;s`*`&eta;s`+`&xi;p`*`&eta;p`)*B*g[r]*A*beta[q]*lambda[p]*Bi^2*`&zeta;p`*
`&xi;p`*`&eta;p`*`&xi;s`*`&eta;s`)) end do end do end do;
%;
> c[1, 1, 1];
                        -7
          4.684724000 10   sin(0.001380646793 t)

                             -7
             + 5.875984466 10   cos(0.001380646793 t)
>
> p := 'p'; q := 'q'; r := 'r';
> theta := sum(sum(sum(c[p, q, r]*X[p]*Y[q]*Z[r], r = 1 .. R), q = 1 .. Q), p
= 1 .. P);
> `&theta;XYZ` := subs([xi = x/L, eta = y/W, zetta = z/S], theta);
> Tfinal := Qin*L*`&theta;XYZ`/(W*S*k)+Tinf;
>
```

APPENDIX E. MAPLE PROCEDURE FOR OPTIMIZING PARAMETERS FOR FURSE DATA

```
> restart;
> with(plots);
> L := 1.2192;
> W := .2032;
> S := 0.635e-2;
> k := 22.6;
> cp := 557;
> rho := 7900;
> alpha := k/(cp*rho);
> Tinf := 295;
> v := 0.1693e-2;
> tau := alpha*t/L^2;
> `&xi;not` := v*t/L;
> A := W/L;
> B := S/L;
> tend := L/v;
> rshoulder := 0.254e-1*(.5*.93);
> rprobe := 0.254e-1*(.5*.284);
> hshoulder := evalf(rshoulder*tan((10*(1/360))*Pi));
> hprobe := .19*0.254e-1;
> `&xi;s` := rshoulder/L;
> `&xi;p` := rprobe/L;
> `&eta;s` := rshoulder/W;
> `&eta;p` := rprobe/W;
> `&zeta;s` := hshoulder/S;
> `&zeta;p` := hprobe/S;
> h := 10;
> U := 330;
> Bi := h*L/k;
> mu := U/h;
> fs := .85;
> fp := .15;
> fo := .5;
> Qin := 2827;
> TC := convert(ExcelTools[Import]("Furse Digestible Data.xls", "Sheet1",
"E2:E6171"), Vector[column], datatype = float[8]);
> TClocs := convert(ExcelTools[Import]("Furse Digestible Data.xls", "Sheet2",
"B2:D51"), Matrix, datatype = float[8]);
> Timer := ExcelTools[Import]("F2procdata.xls", "Sheet1", "A2:A6171"); Time
:= Vector(6170, 1, proc (i) options operator, arrow; Timer[i, 1] end proc,
datatype = float[8]);
> TC;
                Vector[column](%id = 444041632)
lambdafinder := (varlambda^2-Bi^2)*tan(varlambda)-2.0*varlambda*Bi:
lambda:=Vector(80,datatype=float[8]):
n := 1:
for m to 80 do
```

```
   a := fsolve(lambdafinder = 0, varlambda = (m-.9999999)*2.5 .. 2.5*m);
   if type(a, float) then lambda[n] := a; n := n+1 end if;
end do:
P := n-1;
betafinder := varbeta*tan(A*varbeta)-Bi:
beta:=Vector(60,datatype=float[8]):
n := 1:
for m to 60 do
   b := fsolve(betafinder = 0, varbeta = (m-1)*10 .. 10*m);
   if type(b, float) then beta[n] := b; n := n+1 end if;
end do:
Q := n-1;
```

64
32

```
assign(eval([xi=x/L,eta=y/W,zetta=z/S],[x=TClocs[4,1],y=TClocs[4,2],z=TClocs[
4,3]]));
NX:=Vector(P,(i)->(Bi^2+lambda[i]^2+2*Bi)/(2*Bi^2),datatype=float[8]):
X:=Vector(P,(i)-
>sin(lambda[i]*xi)+lambda[i]*cos(lambda[i]*xi)/Bi,datatype=float[8]):
NY:=Vector(Q,(i)-
>(A*Bi^2+A*beta[i]^2+Bi)/(2*A*(beta[i]^2+Bi^2)),datatype=float[8]):
Y:=Vector(Q,(i)->cos(A*beta[i]*eta),datatype=float[8]):
>
> EIGEXP3 := proc (fractionp::float, fs::float, fp::float, fo::float,
U::float) mu := U/h; gammafinder := (varg^2-Bi^2*mu)*tan(B*varg)-
Bi*varg*(mu+1.0); g := Vector(60, datatype = float[8]); n := 1; for m to 30
do c := fsolve(gammafinder = 0, varg = 200*m+200*(-.99999) .. 200*m); if
type(c, float) then g[n] := c; n := n+1 end if end do; R := n-1; NZ :=
Vector(R, proc (i) options operator, arrow;
1/2+(1/2)*g[i]^2/Bi^2+((1/2)*g[i]/(B*Bi^2)-
(1/2)/(B*g[i]))*sin(B*g[i])*cos(B*g[i])+sin(B*g[i])^2/(B*Bi) end proc,
datatype = float[8]); Z := Vector(R, proc (i) options operator, arrow;
sin(B*g[i]*zetta)+g[i]*cos(B*g[i]*zetta)/Bi end proc, datatype = float[8]);
THETA :=
add(add(add(((Bi*(lambda[p]^2+beta[q]^2+g[r]^2)+lambda[p]^2*v*L/alpha)*sin(la
mbda[p]*`&xi;not`)+(lambda[p]*(lambda[p]^2+beta[q]^2+g[r]^2)-
Bi*lambda[p]*v*L/alpha)*cos(lambda[p]*`&xi;not`))*(-
1/2)*(Bi*fo*sin(A*beta[q]*`&eta;s`)*sin(B*g[r])*sin(lambda[p]*`&xi;s`)*`&zeta
;s`*B*g[r]*`&zeta;p`*`&xi;p`^2*`&eta;p`^2+Bi*fp*sin(A*beta[q]*`&eta;p`)*cos(`
&zeta;p`*B*g[r])*sin(lambda[p]*`&xi;p`)*`&zeta;s`*`&xi;s`*`&eta;s`*`&xi;p`*`&
eta;p`-
Bi*fo*sin(A*beta[q]*`&eta;s`)*sin(B*g[r])*sin(lambda[p]*`&xi;s`)*`&zeta;s`*B*
g[r]*`&zeta;p`*`&xi;p`*`&eta;p`*`&xi;s`*`&eta;s`-
Bi*fp*sin(A*beta[q]*`&eta;p`)*sin(lambda[p]*`&xi;p`)*`&zeta;s`*`&xi;s`*`&eta;
s`*`&xi;p`*`&eta;p`-
Bi*fp*sin(A*beta[q]*`&eta;p`)*cos(`&zeta;p`*B*g[r])*sin(lambda[p]*`&xi;p`)*`&
zeta;s`*`&xi;s`^2*`&eta;s`^2+Bi*fs*sin(A*beta[q]*`&eta;p`)*cos(B*g[r]*`&zeta;
s`)*sin(lambda[p]*`&xi;p`)*`&zeta;p`*`&xi;p`*`&eta;p`*`&xi;s`*`&eta;s`+Bi*fs*
sin(A*beta[q]*`&eta;s`)*sin(lambda[p]*`&xi;s`)*`&zeta;p`*`&xi;p`*`&eta;p`*`&x
i;s`*`&eta;s`-
Bi*fs*sin(A*beta[q]*`&eta;s`)*cos(B*g[r]*`&zeta;s`)*sin(lambda[p]*`&xi;s`)*`&
zeta;p`*`&xi;p`*`&eta;p`*`&xi;s`*`&eta;s`+Bi*fp*sin(A*beta[q]*`&eta;p`)*sin(l
ambda[p]*`&xi;p`)*`&zeta;s`*`&xi;s`^2*`&eta;s`^2-
Bi*fs*sin(A*beta[q]*`&eta;p`)*sin(lambda[p]*`&xi;p`)*`&zeta;p`*`&xi;p`*`&eta;
p`*`&xi;s`*`&eta;s`+fp*sin(A*beta[q]*`&eta;p`)*sin(`&zeta;p`*B*g[r])*sin(lamb
da[p]*`&xi;p`)*`&zeta;s`*g[r]*`&xi;s`^2*`&eta;s`^2+fo*sin(A*beta[q]*`&eta;s`)
```

```
*g[r]^2*cos(B*g[r])*sin(lambda[p]*`&xi;s`)*`&zeta;s`*B*`&zeta;p`*`&xi;p`^2*`&
eta;p`^2+fs*sin(A*beta[q]*`&eta;s`)*sin(B*g[r]*`&zeta;s`)*sin(lambda[p]*`&xi;
s`)*g[r]*`&zeta;p`*`&xi;p`*`&eta;p`*`&xi;s`*`&eta;s`-
fp*sin(A*beta[q]*`&eta;p`)*sin(`&zeta;p`*B*g[r])*sin(lambda[p]*`&xi;p`)*`&zet
a;s`*g[r]*`&xi;s`*`&eta;s`*`&xi;p`*`&eta;p`-
fo*sin(A*beta[q]*`&eta;s`)*g[r]^2*cos(B*g[r])*sin(lambda[p]*`&xi;s`)*`&zeta;s
`*B*`&zeta;p`*`&xi;p`*`&eta;p`*`&xi;s`*`&eta;s`-
fs*sin(A*beta[q]*`&eta;p`)*sin(B*g[r]*`&zeta;s`)*sin(lambda[p]*`&xi;p`)*g[r]*
`&zeta;p`*`&xi;p`*`&eta;p`*`&xi;s`*`&eta;s`)*X[p]*Y[q]*Z[r]/(NX[p]*NY[q]*NZ[r
]*Bi*((lambda[p]^2+beta[q]^2+g[r]^2)^2+lambda[p]^2*v^2*L^2/alpha^2)*`&zeta;s`
*(-
`&xi;s`*`&eta;s`+`&xi;p`*`&eta;p`)*B*g[r]*A*beta[q]*lambda[p]*Bi^2*`&zeta;p`*
`&xi;p`*`&eta;p`*`&xi;s`*`&eta;s`), q = 1 .. Q), p = 1 .. P), r = 1 .. R);
Tfinal := THETA*fractionp*Qin*L/(W*S*k)+Tinf; unTfinal := unapply(Tfinal, t);
ret := evalf(unTfinal(Time[4500])-TC[4500])^2+evalf(unTfinal(Time[4317])-
TC[4317])^2+evalf(unTfinal(Time[5001])-
TC[5001])^2+evalf(unTfinal(Time[4310])-
TC[4310])^2+evalf(unTfinal(Time[6000])-TC[6000])^2; if type(bestfound,
extended_numeric) and ret < bestfound then bestfound := ret; userinfo(1,
EIGEXP3, `new best objective value found:`, ret) end if; ret end proc;
objf3 := proc(V::Vector)
  EIGEXP3(V[1],V[2],V[3],V[4],V[5]);
end proc:
objf3gradient := proc(X::Vector,G::Vector)
  G[1] := fdiff( EIGEXP3, [1], [X[1],X[2],X[3],X[4],X[5]] );
  G[2] := fdiff( EIGEXP3, [2], [X[1],X[2],X[3],X[4],X[5]] );
  G[3] := fdiff( EIGEXP3, [3], [X[1],X[2],X[3],X[4],X[5]] );
  G[4] := fdiff( EIGEXP3, [4], [X[1],X[2],X[3],X[4],X[5]] );
  G[5] := fdiff( EIGEXP3, [5], [X[1],X[2],X[3],X[4],X[5]] );
  NULL;
end proc:
> Aeq := Matrix([[0, 1, 1, 0, 0]], datatype = float);
> beq := Vector([1], datatype = float);
> lc := [NoUserValue, NoUserValue, Aeq, beq];
>
infolevel[Optimization]:=6:
bestfound:=infinity:
infolevel[EIGEXP3]:=1:
Optimization:-NLPSolve( 5, objf3,lc,
        [<0.1,0.01,0.01,0.01,50.0>, <1.0,1.0,1.0,1.0,1000.0>],
        'objectivegradient'=objf3gradient,
        'initialpoint'=Vector([0.5796,0.8767,0.1233,0.6365,160.4]),
'method'='sqp',iterationlimit=200);
NLPSolve: calling NLP solver
NLPSolve: using method=sqp
NLPSolve: number of problem variables 5
NLPSolve: number of nonlinear inequality constraints 0
NLPSolve: number of nonlinear equality constraints 0
NLPSolve: number of general linear constraints 1
NLPSolve: feasibility tolerance set to 0.1053671213e-7
NLPSolve: optimality tolerance set to 0.3256082241e-11
NLPSolve: iteration limit set to 200
NLPSolve: infinite bound set to 0.10e21
NLPSolve: trying evalf mode
attemptsolution: number of major iterations taken 75
     [706.049475164990440,Vector[column](%id = 446225208)]>
```